The Effects of Light-Absorbing Aerosols, Blocking, and Clouds on Greenland's Surface

by

Jamie L. Ward

A dissertation submitted in partial fulfillment
of the requirements for the degree of
Doctor of Philosophy
(Atmospheric, Oceanic, and Space Sciences)
in the University of Michigan
2020

Doctoral Committee:

Associate Professor Mark G. Flanner, Chair
Associate Professor Christiane Jablonowski
Assistant Professor Kerri Pratt
Professor Allison Steiner

Jamie L. Ward

jamiewa@umich.edu

ORCID ID: 0000-0002- 8751-8894

Dedication

I dedicate this dissertation to my parents and sister.
Your support and love have sustained me from start to finish.

Acknowledgements

When I started college in September 2005 at the University of Michigan-Flint, I had planned to complete college in 4 years and enter the workforce as an architect. Happily, I have pursued a different career path and consequently developed in to the person I am today. I'd like to thank those who have influenced my evolution as a scientist and person throughout this journey.

I could not ask for a better doctoral advisor than Mark Flanner. He is kind and is always available to help while not being overbearing or pushy. From what I've heard, this is a difficult balance for advisors to achieve, and Mark has done so with flying colors. Mark, thank you for always encouraging me and finding ways to help me surmount self-doubt. I'd also like to thank my dissertation committee members, Allison Steiner, Christiane Jablonowski, and Kerri Pratt, for their advice as I wrapped up my doctoral research.

I firmly believe that successfully completing graduate school without good friends is impossible. I'd like to thank my officemates for providing an abundance of advice and entertainment throughout the years. Anthony, Matt, Rosa, "the Zachs", Chloe, Adam, Deepak, and Dan have all collectively provided stellar life and research advice while also making me laugh so hard I cried (I apologize to those who heard our antics from afar). Abby, Annareli, Alan, Natasha, Sam, Juan, Stacey, Greg, David, Emily, Daniel, Justin, Chaoyi, and the other graduate students were all so supportive and friendly. You all made this journey possible for me.

I'd also like to thank those friends I made before starting my doctoral program for their continued friendship and support. I've remained close with Tom, Melissa, Doc, and Mary from my Earth Science days at UM-Flint for over ten years now. Ashley ("Wee One") has been a steadfast friend for over 10 years and has always encouraged me as I pursued my dreams. As a master's student at Indiana State, Brooke was my lifeline when I lived away from home and is still one of my best friends. While at UM, I've lived with my sister, Robin, and her friend from school, Jordan. They both work in the UM hospital system have been under unusual strain over the past few months because of COVID-19; I would like to thank them for their patience and support as I dealt with a different variety of stress. We've had some good laughs (if you ever want to make Jordan laugh until she cries, just drive into a carwash with your window down).

Most importantly, none of this would have been possible without my family. My parents (Allan and Barbara) and sister always encouraged me and were the first to celebrate my successes. Mom and Dad worked full-time to provide for Robin and myself while always being there for events and games. They taught us about the importance of good work ethic, education, and being kind to others. I am forever grateful for their love and support and I hope to continue to make them proud.

I hope to use what I have learned in graduate school and from those who have shaped me as a person to better the world through kindness and scholarship. It is important for researchers to understand how we can impact the world through the communication of our work, and I aim to do my best to further our understanding of the climate system for all of humankind.

"Words are, in my not so humble opinion, our most inexhaustible source of magic..." −Albus Dumbledore, *Harry Potter and the Deathly Hallows* by J.K. Rowling

Table of Contents

List of Tables

List of Figures

Abstract

The Greenland Ice Sheet covers over 80% of Greenland's land area and is the largest reservoir of frozen water in the Northern Hemisphere. Over the past few decades, the Greenland Ice Sheet has experienced significant summertime ice and surface snow loss. Much of this mass loss can be attributed to short-term processes that initiate surface energy changes. In this dissertation, we examine the effects of 1) light-absorbing aerosols on the Greenland Ice Sheet and in the overlying atmosphere, 2) the impacts of atmospheric block location over the Greenland Ice Sheet on cloud formation and atmosphere-surface energy exchanges, and 3) how these block-induced surface energy responses will change in the future.

Aerosols are microscopic solid or liquid particles that can be transported long distances through the atmosphere. Light-absorbing aerosols like black carbon and certain types of dust are unique in that they absorb sunlight and warm the local environment. In the Arctic, black carbon reduces surface reflectivity and increases surface energy to induce or enhance melt. Light-absorbing aerosols suspended in the atmosphere warm the local air and change vertical circulation patterns. We use an idealized version of the Community Earth System Model (CESM) to understand how Greenland-specific local atmospheric and in-snow light-absorbing aerosols can affect Greenland Ice Sheet surface energy input and snowmelt processes. Overall, we find that the largest snowmelt and net surface energy responses occur in simulations containing only in-snow light-absorbing aerosols while atmospheric absorbing aerosols decrease

incident sunlight on the surface and produce insignificant melt and energy changes. Atmospheric and in-snow aerosols have offsetting effects on the surface energy budget.

Atmospheric blocks are mostly stationary high pressure systems that last for days to weeks at a time. Blocking over Greenland has been shown to enhance net surface energy by reducing cloud cover and transporting warm, moist air over the surface. The variability of the Greenland Ice Sheet topography impacts regional block-induced surface changes based on block location. We use a variety of observational datasets to understand the impacts of block location on cloud formation and surface energy fluxes over the Greenland Ice Sheet. Blocking over northern Greenland produces larger cloud reductions that enhance sunlight and decrease net longwave energy at the surface than southern Greenland blocking activity. Net surface energy increases for all block locations, but more so for blocks over eastern Greenland because of greater warm air transport in combination with enhanced sunlight absorption by the Greenland Ice Sheet.

Five different global climate simulations from the Coupled Model Intercomparison Project, phase 6 (CMIP6) are examined to understand how summer Greenland blocking activity will affect net surface energy fluxes in the middle (2040-2059) and at the end (2080-2099) of the 21st century for the largest warming scenario. Net surface energy input increases with blocking over all simulations. However, atmospheric warming over the Greenland Ice Sheet produced by block circulation plays a larger role in total energy enhancement than solar energy input changes. Future net surface energy fluxes may be larger because historical (1986-2005) CMIP6 simulations underestimate component and total energy fluxes found in Modern Era Retrospective Analysis, version 2 (MERRA-2) observational data. These results indicate that Greenland blocking will continue to contribute to increased total surface energy in the future.

Chapter 1. Introduction

1.1 Greenland Geography and Surface

Greenland is located in the Northern Hemisphere high latitudes between the Atlantic and Arctic Oceans and is the largest island in the world. Over 80% of Greenland's land surface is covered by the Greenland Ice Sheet (GrIS). The GrIS covers roughly 1.7 million km^2 of land area and is the second largest ice sheet in the world (the largest being the Antarctic Ice Sheet). Its frozen water volume is equivalent to over 7m of global sea level rise (Gregory et al., 2004; Church et al., 2013), which would inundate coastal populations around the world. Like the Antarctic Ice Sheet, the GrIS is characterized by steeper margins and a relatively flat interior (Fig. 1.1). At its most elevated point, Summit, the GrIS is 3.25km thick (Shupe et al., 2013). The surface of the GrIS is snow-covered, with partially compacted snow (i.e., firn) beneath new snow and ice composing the remaining mass.

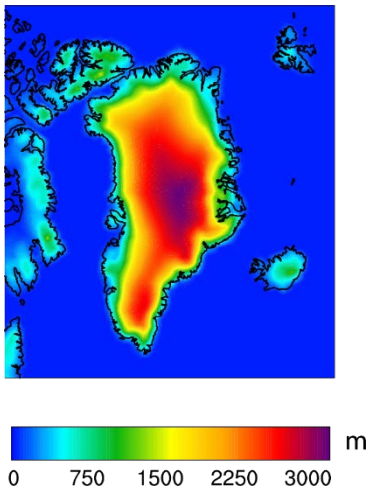

Fig. 1.1: Greenland elevation map produced using Modern-Era Retrospective Analysis for Research and Applications, version 2 (MERRA-2) surface geopotential data.

1.2 Greenland Ice Sheet Mass Changes

GrIS mass changes via surface processes constitute the surface mass balance (SMB), a metric used to compare total mass loss to total mass gain. Precipitation (snowfall or rainfall) positively impacts GrIS SMB, while sublimation, evaporation, and melt all lead to mass loss. Net accumulation and loss occur over the accumulation and ablation zones of the GrIS, respectively. The accumulation zone is defined by fresh, highly reflective snow in elevated GrIS interior and is characterized by net surface mass gain. The GrIS margins constitute the ablation zone and are where summer snowmelt and net surface mass loss occur most regularly. These snow zones naturally occur because the higher GrIS elevations are colder and less prone to melt and refreezing processes. The ablation zone locations are defined as areas that have annual net surface mass loss (i.e., Lenaerts et al., 2019). Fig. 1.2 illustrates the geographical coverage of the summer 2012 GrIS accumulation (blue) and ablation (red) zones with 0℃ as the boundary (Bennartz et al., 2013).

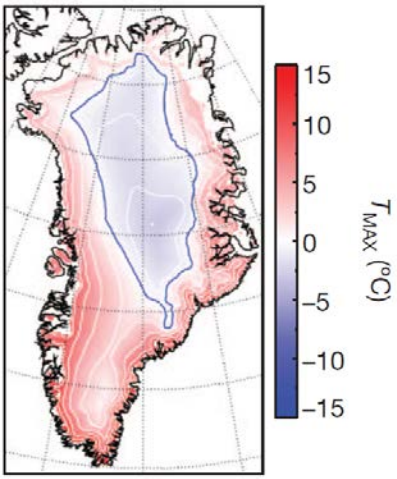

Fig. 1.2: Summer 2012 representation of the accumulation and ablation zones, based on surface temperature (courtesy of Bennartz et al., 2013).

1.3 Net Surface Energy (E_{Total})

Snowmelt is triggered when the surface receives enough energy to warm above the freezing point of water. Atmosphere-surface energy exchange is produced through "radiative" and "non-radiative" processes. Radiative energy broadly refers to electromagnetic radiation, or energy that consists of electric and magnetic fields and can travel through any medium. All electromagnetic radiation is classified by wavelength (λ), or distance between consecutive crests (units of meters). All possible radiative energy wavelengths constitute the electromagnetic spectrum. In order to broadly classify different types of radiative energy, the spectrum is divided into 7 different energy varieties (Fig. 1.3):

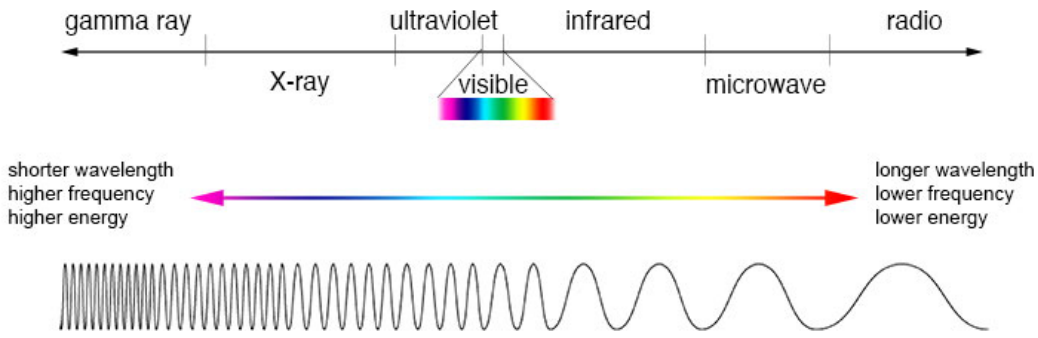

Fig. 1.3: Schematic of the electromagnetic spectrum and its divisions based on wavelength (courtesy of Humboldt State University, 2019).

The largest source of energy input for the Earth system is solar energy produced by the sun. The sun, which maintains an average temperature between 5500 and $6000K$, produces peak emissions in the visible light portion of the electromagnetic spectrum (Fig. 1.3). Most of the incoming solar radiation (i.e., "insolation") at the top of the atmosphere is characterized by wavelengths ranging from $0.1\mu m$ to $4\mu m$ (ultraviolet, visible light, and near-infrared, collectively referred to as "shortwave" energy), and of this incoming energy, a large portion of the ultraviolet energy does not reach the Earth's surface.

Incident shortwave energy can either be scattered (i.e., deflected), absorbed, or transmitted by the atmosphere and surface. In the case of surface-insolation interactions, the amount of shortwave energy that is scattered depends on the surface reflectivity, or albedo. Albedo is a unitless quantity defined as the ratio of upwelling shortwave energy ($SW^{\uparrow}$) that is scattered back into the atmosphere to the total amount of downwelling insolation that reaches the surface ("downwelling shortwave", $SW^{\downarrow}$):

$$\alpha = \frac{SW^{\uparrow}}{SW^{\downarrow}} \quad (1.1).$$

Earth's average surface albedo is ~0.15; 15% of all energy that reaches the Earth's surface is reflected back towards space. However, deserts, ice, and snow-covered surfaces like the GrIS maintain higher-than-average albedos (e.g., summertime GrIS-wide albedos range from 0.65 to 0.75 (Box et al., 2012)). Net shortwave energy (SW_{net}), or the amount of insolation absorbed by the surface, depends on the surface albedo and is defined as follows:

$$SW_{net} = SW^{\downarrow} - SW^{\uparrow} = SW^{\downarrow} - \left(\alpha * SW^{\downarrow}\right) = SW^{\downarrow}(1 - \alpha) \quad (1.2).$$

GrIS SW_{net} varies seasonally and is lower over the pristine accumulation zone snow than the lower albedo ablation zone surface.

Although SW_{net} is generally low over the GrIS, small, negative perturbations in surface albedo produced by snow metamorphism (i.e., snow grain shape change from crystals to spheres over time) or external factors (discussed in section 1.5) can trigger continuing melt via increasing SW_{net} through the ice-albedo feedback mechanism. Within this positive ice-albedo feedback process, decreasing albedo enhances melt, which further reduces surface albedo and increases SW_{net} and melt. The ice-albedo feedback process can only be halted by 1) melting all existing frozen water, 2) by overlaying old snow with fresh snow precipitation, which increases surface albedo, or 3) surface temperature falling below 0°C. Because Greenland and the broader Arctic

climate system are snow- and ice-covered, they are more susceptible to Arctic Amplification, or the ice-albedo feedback cycle that has produced larger regional warming and enhanced melting (Screen et al., 2012; Jiao and Flanner, 2016).

Like the sun, the Earth and its overlying atmosphere also emit electromagnetic radiation. However, because the Earth's average emitting temperature is much lower (approximately $288K$), the emitted energy wavelength range is $4 - 200\ \mu m$. These less energetic wavelengths are almost completely separate from shortwave radiation and are referred to as "longwave" or "terrestrial" energy (Fig. 1.4).

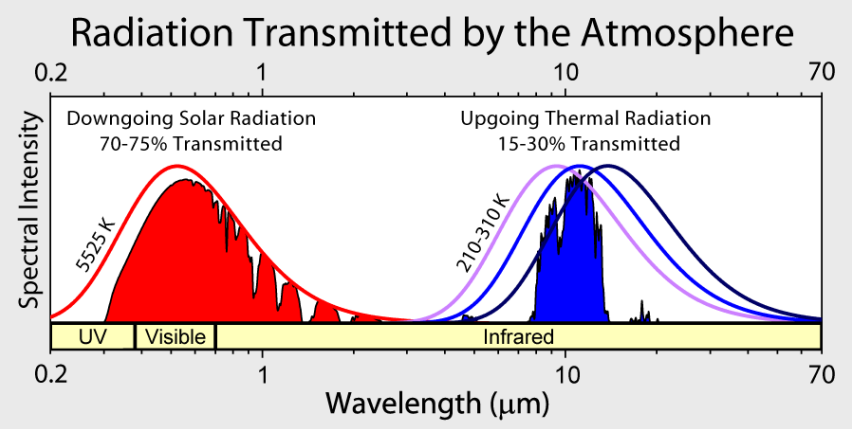

Fig. 1.4: Shortwave (red) versus longwave (blue) emission wavelength ranges.

Earth's surface, atmospheric gases, and clouds are all longwave energy emitters. The total power radiated by any body or object per unit area is calculated using the Stefan-Boltzmann law:

$$E = \varepsilon \sigma T^4 \qquad (1.3),$$

where ε is the scaling factor that accounts for non-blackbody (i.e., less than 100% radiating efficiency) radiation, $\sigma = 5.67 \times 10^{-8}\ W\ m^{-2}\ K^{-4}$ is the Stefan-Boltzmann constant, and T is the temperature (in K) of the emitting body. Like surface net shortwave energy, absorbed longwave energy is defined by upwelling (out of the surface (s), $LW^{\uparrow}$) and downwelling (from

$$LW_{net} = LW^{\downarrow} - LW^{\uparrow} = \varepsilon_s LW^{\downarrow} - \varepsilon_s \sigma {T_s}^4 \quad (1.4).$$

Sensible (SH) and latent heat (LH) fluxes are so-called "turbulent fluxes" that are directly proportional to wind speed, surface roughness, and air density magnitudes. Sensible (latent) heat flux direction is directed from locations of higher temperature (specific humidity) to lower temperature (specific humidity). Sensible heating adds more to total surface energy than latent heating over most of the GrIS. All seasonal average sensible heat fluxes are directed from the atmosphere into the surface (Fig. A.1). Turbulent heating could become increasingly important as the overlying atmosphere warms in the future (van den Broeke et al., 2011).

Net surface energy flux ($E_{Total}; W/m^2$) is thus the sum of radiative (SW_{net}, LW_{net}) and non-radiative energy fluxes (SH and LH; positive when directed downward):

$$E_{Total} = SW_{net} + LW_{net} + SH + LH \quad (1.5).$$

When $E_{Total} > 0$, energy is added to the surface; if enough total energy is added to the GrIS surface, surface mass balance decreases. Dominant surface energy flux contributions to net surface energy vary over the GrIS and depend on climatological winds, elevation, surface albedo, and moisture presence, among other factors. Fig. 1.5 illustrates GrIS surface features, energy fluxes, and mass balance changes over the ablation and accumulation zones. These can vary with different melt triggering events, which we discuss in next section 1.5.

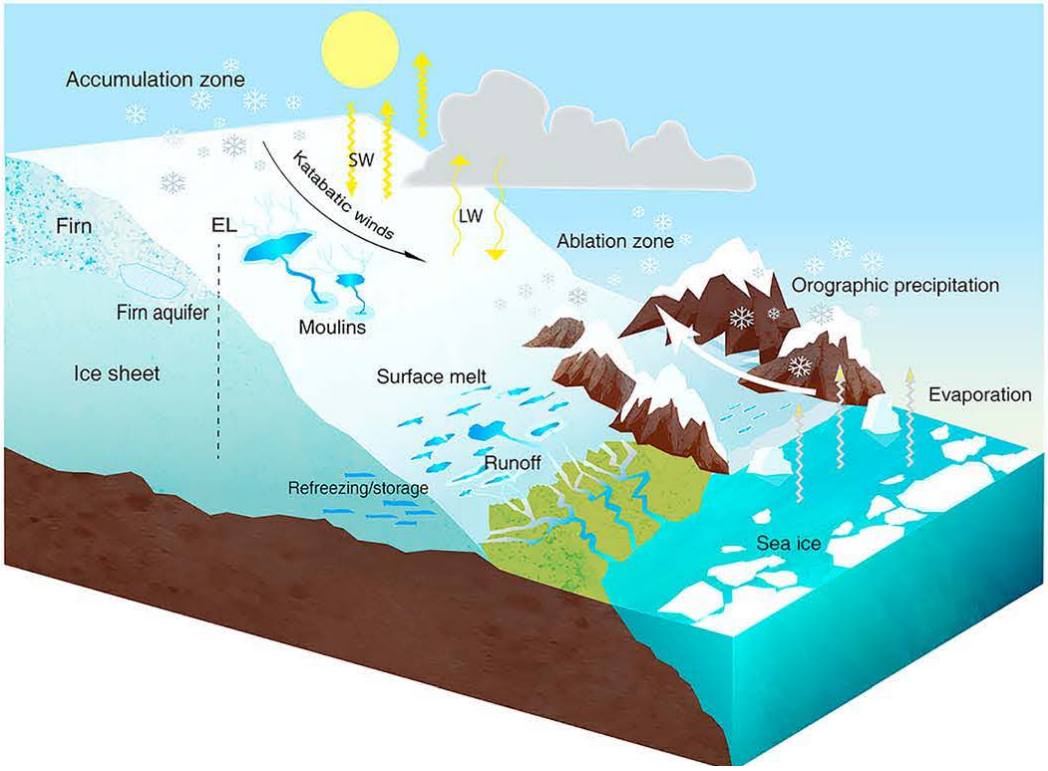

Fig. 1.5: Sample accumulation and ablation zone illustration of the GrIS. Katabatic winds result when cold, dense air from the GrIS interior flows downslope over the accumulation zone (Lenaerts et al., 2019).

1.4 Greenland Ice Sheet Melt

Since 1980, GrIS total mass loss has exceeded mass gain through ice discharge processes (Mouginot et al., 2019). Mass loss has further accelerated into the 21st century. Between 2002 and 2011, the GrIS lost $214 \pm 58\ Gt/yr$, which was approximately 6 times as large as the 1992-2001 mass loss average (Tedesco et al., 2016a). Fig. 1.6 depicts the non-linear nature of GrIS-average mass loss between April 2002 and July 2014 (Khan et al., 2015).

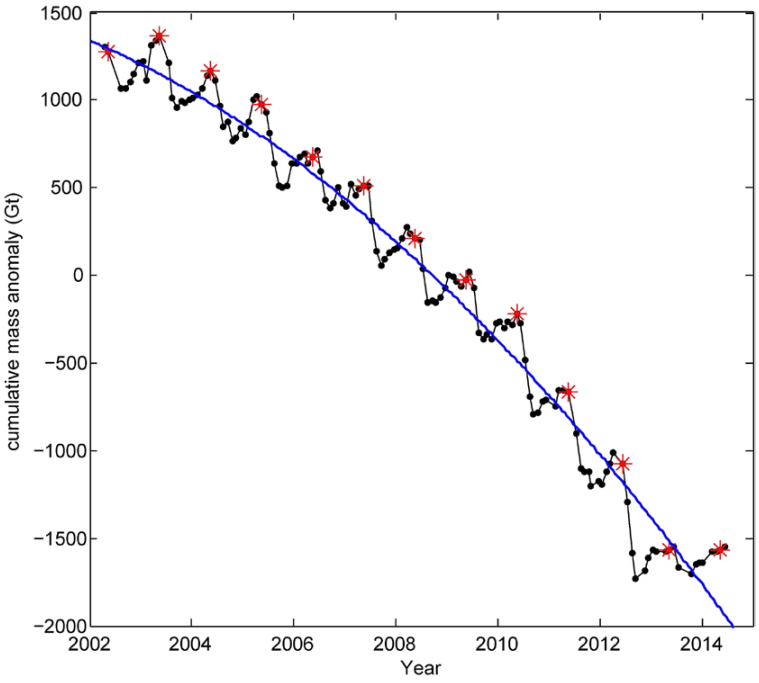

Fig. 1.6: GrIS-wide total mass change (gain-loss) derived from GRACE between April 2002 and July 2014 (Khan et al., 2015).

Surface mass loss through runoff (originating from melt) increased from 1990 onward and constituted roughly 60% of all ice sheet mass change (Rignot et al., 2008; Fettweis et al., 2013; Fettweis et al., 2017). Especially since the mid-2000s, snowmelt loss has been unprecedented. The summers of 2007, 2010, 2012, 2015, and 2019 have all produced record-high surface melt volume over greater area (Tedesco et al., 2008; Tedesco et al., 2011; Nghiem et al., 2012; Hanna et al., 2014; Tedesco et al., 2016b; Tedesco and Fettweis, 2020) dating back through 1889 in ice core records (i.e., Neff et al., 2014).

GrIS snowmelt can occur over varying temporal and spatial scales. The duration and spatial coverage of melt events is largely determined by the melt triggering mechanism. For example, higher average summer temperatures will slowly enhance average seasonal snowmelt

rates. Persistent atmospheric warming preconditions the surface to future melt by reducing snow albedo through snow metamorphism and refreezing processes (i.e., ice-albedo feedback mechanism). Some of GrIS snowmelt can be explained by Arctic Amplification, or increased warming in the Arctic relative to the rest of the northern hemisphere. Arctic Amplification results from sea ice melt and open water, surface ice-albedo feedback, oceanic warming, and atmospheric circulation and warming, among others (Serreze and Barry, 2011). These mechanisms all occur on different time scales and have ultimately led to decades-long Arctic Amplification that is predicted to continue well into the future (Serreze and Barry, 2011).

Episodic GrIS snowmelt is spatially heterogeneous and can occur as a result of short-lived melt triggers in the atmosphere and on the surface (Velicogna et al., 2014; Cullather and Nowicki, 2018). An example of extreme GrIS surface snowmelt occurred on 11-12 July, 2012 when melt was recorded over >98% of the GrIS and included Summit, Greenland (i.e., the highest elevation of the GrIS) (Nghiem et al., 2012). Because the most recent instance of snowmelt at Summit preceding this event occurred in 1889 (Neff et al., 2014), the July 2012 event has been widely studied to better understand how it was triggered. Coincident with extensive melt, the following conditions were observed on the GrIS and in the overlying atmosphere: black carbon aerosols (BC) in Summit firn cores (Keegan et al., 2014); persistent atmospheric ridging producing anticyclonic circulation (e.g., Nghiem et al., 2012; Tedesco et al., 2013; Hanna et al., 2014); thin, liquid clouds were detected at higher elevations (e.g., Bennartz et al., 2013; Miller et al., 2015); and strong moisture transport through an atmospheric river (e.g., Mattingly et al., 2018). The 2012 melt season also began two weeks earlier in the year than usual (Tedesco et al., 2013) and was accompanied by persistent anticyclonic circulation between May and July (Hanna et al., 2014). All of these mechanisms likely played a role in the GrIS-wide melt

that transpired in mid-July. However, it is very unusual for all of these conditions to be present simultaneously. The triggers on summer GrIS surface processes examined in this dissertation include 1) black carbon and other light-absorbing impurities, 2) clouds, and 3) atmospheric blocking. These will be discussed in further detail in the following section.

1.5 Greenland Ice Sheet Melt Triggers

1.5.1 Black Carbon

Black carbon (BC) is an inorganic, irregularly-shaped microscopic (diameter $\leq 2.5\mu m$) aerosol (i.e., liquid or solid particle) that is produced naturally (e.g., biomass burning) and anthropogenically (e.g., fossil fuel, coal, and wood fire combustion) (Bond et al., 2007, 2013). Since the onset of the Industrial Revolution, global cumulative BC emissions produced through biofuel and fossil fuel combustion have increased linearly from 1.0 to 4.5 Tg/year (Bond et al., 2007). Relative contributions of fuel types to these emissions have changed with evolving technologies and fuel preferences. As of 2000, average total BC emissions produced via fuel combustion is 4.8 Tg/yr (Bond et al., 2013). Biomass burning and other natural processes produced average global BC emissions of 1.86 Tg/yr between 1997 and 2016 (van der Werf et al., 2017), which is less than half of the anthropogenic emissions. Because BC particles are so small, they can remain suspended in the atmosphere for days to weeks at a time (Bond et al., 2013). Averaged over the entire globe, modeled atmospheric BC burdens at the start of 21st century were 0.088-0.24 Tg (Liu et al., 2012).

Unlike other common aerosol species (e.g., sulfates, sea salt, and certain dust species), BC is an efficient absorber of shortwave energy and can thus induce localized warming. Atmospheric warming occurs when suspended BC particles absorb incoming sunlight and heat

the surrounding air. If suspended BC concentrations are large enough, sunlight absorption in the aerosol layer will lead to shortwave cooling on the underlying surface through “dimming”. Warming produced by BC direct aerosol forcing can also impact local atmospheric stability. BC at high altitudes decreases the environmental lapse rate to induce vertical stability, while BC close to the surface increases the environmental lapse rate and decreases stability (Ban-Weiss et al., 2011; Flanner, 2013).

Cloud formation processes are also impacted by atmospheric BC. Although freshly-emitted BC is generally insoluble and independent of other aerosol species (i.e., externally mixed) (Chýlek et al., 1984; Koch et al., 2009; Liu et al., 2012; Bond et al., 2013), often quickly becomes coated with water-soluble compounds like sulfates or organics (Wang, 2004; Koch et al., 2009; Liu et al., 2012; Bond et al., 2013; Allen and Landuyt, 2014). Coated BC can serve as cloud condensation nuclei, thus indirectly impacting shortwave fluxes through cloud scattering processes and by extending cloud life span. Localized warming produced by suspended BC can also decrease local relative humidity and lead to cloud burn-off, which can increase the amount of insolation that reaches the surface.

Deposited BC leads to surface warming, especially over the high-albedo snow- and ice-covered surfaces in the polar regions. BC in snow and ice decreases surface albedo and increases net shortwave energy flux to warm the surface and enhance melt (Warren and Wiscombe, 1980; Flanner et al., 2007). This is especially important in the summer months when solar insolation is highest (McConnell et al., 2007). Estimated BC radiative forcing over snow, ice, and other highly reflective surfaces is roughly $+2.8 \pm 0.4\, W/m^2$ (Ban-Weiss et al., 2012), which is over three times larger than the global average BC radiative forcing of $+0.88(+0.17, +1.48)\, W/m^2$ (Bond et al., 2013). Overall, snow and ice warming due to BC forcing is roughly 2-4 times

greater than that produced by equal carbon dioxide-caused forcing (Hansen and Nazarenko, 2004; Flanner et al., 2007).

Most BC over Greenland or on the GrIS surface originates from forest fires in Canada and Russia (e.g., Thomas et al., 2017). Although average BC mass mixing ratios over the GrIS are smaller than over other Arctic regions (Doherty et al., 2010; Polashenski et al., 2015), melt and warming are easily triggered because of the high GrIS albedo. The compared effects of atmospheric and in-snow BC on GrIS melt and energy fluxes need to be explored. Furthermore, since future atmospheric and in-snow burdens over Greenland could change in response to enhanced circumpolar forest burning in the Northern Hemisphere (i.e., Soja et al., 2007), it is important to understand how large BC burdens could impact GrIS surface melt and energy processes.

1.5.2 Clouds

Clouds affect net surface energy fluxes by decreasing net shortwave energy via scattering and emitting longwave energy down to the surface (Fig. 1.7). The negative (positive) impacts of clouds on shortwave (longwave) energy fluxes relative to cloud-free conditions are referred to as cloud radiative forcing. Over the GrIS, cloud coverage is largest between May and September (i.e., Cawkwell and Bamber, 2002; Shupe et al., 2013; Miller et al., 2015; Lacour et al., 2017; McIlhattan et al., 2017). The impacts of summertime clouds are especially important because they can trigger and enhance GrIS melt (e.g., Bennartz et al., 2013).

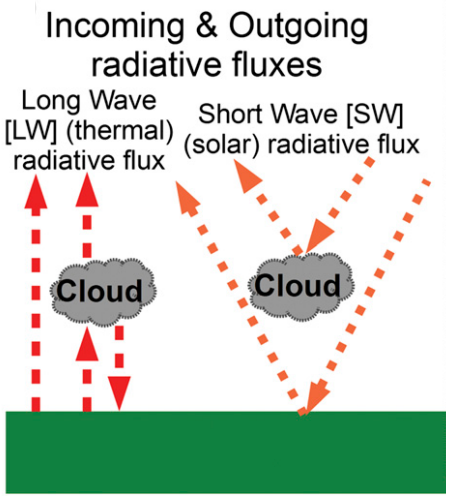

Fig. 1.7: (Left to right) Longwave and shortwave cloud radiative forcing processes (Forsythe et al., 2015).

Especially over elevated GrIS areas, the impact of net shortwave loss produced by clouds is reduced because snow has a high surface albedo. Shortwave cloud radiative impacts are also affected by the solar cycle and cloud transmission (i.e., Cawkwell and Bamber, 2002; Shupe and Intrieri, 2004). Higher solar zenith angle (lower sun angle) reduces insolation and minimizes the shortwave impacts of clouds. Cloud transmitting abilities, on the other hand, largely depend on cloud composition. Compared to ice clouds, liquid-based clouds have higher albedos and thus increase the magnitude of shortwave cloud radiative forcing (Shupe and Intrieri, 2004; Morrison et al., 2012). Small solar zenith angles and increasingly prevalent mixed-phase clouds over the GrIS (Morrison et al., 2012; Shupe et al., 2013; Miller et al., 2015; Lacour et al., 2017) produce more negative shortwave cloud radiative forcing in the summer. This contrasts with winter clouds, which produce negligible shortwave cloud radiative forcing.

Longwave cloud radiative forcing positively contributes to GrIS net surface energy in all seasons (Curry et al., 1996; Shupe and Intrieri, 2004; Miller et al., 2015). Unlike shortwave

cloud radiative forcing, the magnitude of longwave cloud radiative forcing depends on cloud base height and cloud temperature properties, which influence cloud phase and emissivity (Shupe and Intrieri, 2004). Higher cloud bases have lower temperatures because of adiabatic cooling at higher altitudes, which produce greater ice crystal concentrations. Ice crystals emit less longwave energy than liquid cloud droplets (Curry et al., 1996; Shupe and Intrieri, 2004; Miller et al., 2015), which reduces surface longwave cloud radiative forcing. Winter clouds warm the surface through longwave processes (Curry et al., 1996; Shupe and Intrieri, 2004; Miller et al., 2015), while longwave cloud radiative forcing is at least partially offset by negative shortwave cloud radiative forcing in the summer. Over the GrIS, longwave cloud radiative forcing decreases from the margins to the GrIS center because of temperature and moisture changes (Lenaerts et al., 2017).

Optically thin liquid-containing clouds are especially important for GrIS snowmelt enhancement. Low-level liquid clouds with liquid water paths of $10 - 40\ g/m^2$ over high elevation locations like Summit insulate the surface via longwave cloud radiative forcing while also transmitting shortwave energy to the surface and minimizing shortwave cloud radiative forcing (i.e., Bennartz et al., 2013; Solomon et al., 2017). In the future, warming and increased atmospheric moisture (e.g., Serreze and Barry, 2011; Kusunoki et al., 2015) could induce low-level liquid cloud frequency changes over the GrIS accumulation zone and impact regional melt frequency.

These cloud-surface interactions over Greenland are further complicated by underlying surface albedo variability. Wang et al. (2018) use data from the Greenland Climate Network (GC-Net) automatic weather stations to examine the impact of surface albedo and latitude on shortwave, longwave, and net cloud radiative forcing. Southern GrIS albedo decreases

throughout the summer season, so shortwave cloud radiative forcing magnitudes increase between May and September while longwave cloud radiative forcing remains roughly constant (Wang et al., 2018). Because northern Greenland accumulation and ablation zone surface albedo response to warming is lower than southern Greenland, the shortwave cloud radiative effect is lessened and the net cloud radiative effect is more positive (Wang et al., 2018). This spatial variability in surface responses to cloud presence can impact regional GrIS meltwater refreezing (i.e., Van Tricht et al., 2016) and surface mass balance responses. Along with atmospheric moisture and temperature characteristics, cloud formation spatial variability is affected by GrIS surface-airflow interactions. Greenland blocking is a large-scale system that can affect cloud formation and associated cloud radiative forcing spatial variability over the GrIS.

1.5.3 Blocking

Atmospheric blocks are synoptic-size extratropical anticyclones that last for days to weeks at a time and remain mostly stationary throughout their lifespans (Rex, 1950; Lupo and Smith, 1994). Although blocking is most robust and frequent in the winter, the North Atlantic, North Pacific, and eastern European/Russian regions maintain high blocking frequencies in all seasons (Lupo and Smith, 1994; Barriopedro et al., 2006; Croci-Maspoli et al., 2007; Masato et al., 2013). Future global climate simulations generally produce reduced blocking frequencies (Dunn-Sigouin and Son, 2013; Kennedy et al., 2016; Matsueda and Endo, 2017), but these findings are still highly uncertain because global climate models are unable to produce historical synoptic and planetary-scale circulation trends (e.g., Cassano et al., 2006; Franco et al., 2013; Pithan et al., 2016; Hanna et al., 2018b).

Greenland blocking, which is a variety of North Atlantic blocking, has shown increased summertime frequencies since the start of the 21st century (Fettweis et al., 2011; Box et al., 2012; Rajewicz and Marshall, 2014; Hanna et al., 2015). Multiple atmospheric and surface processes have been cited as possible causes for the observed Greenland blocking frequency changes. The first is the North Atlantic Oscillation (NAO) teleconnection pattern that is modulated by atmospheric pressure change between the Azores High and Icelandic Low semi-permanent pressure systems. Negative NAO indices characterize lower pressure changes with latitude and more meridional-like airflow in the North Atlantic region. Like Greenland blocking activity, negative NAO indices have become more frequent over the past 20 years (i.e., Davini et al., 2012; Hanna et al., 2013, 2014, 2015, 2016; Hassanzadeh and Kuang, 2015). Whether Greenland blocking activity induces negative NAO through dynamic-based Rossby Wave Breaking activity in the upper troposphere (Woollings et al., 2008) or NAO pressure changes trigger Greenland blocking activity (Overland et al., 2012; Hanna et al., 2015) remains unclear. Another process that is hypothesized to increase Greenland blocking activity is the reduction of summertime sea ice surrounding Greenland. Reduced sea ice exposes underlying ocean water and warms the overlying atmosphere to enhance local geopotential height patterns over and around Greenland (Liu et al., 2016). Since summertime Arctic-average sea ice is virtually non-existent at the end of the 21st century across numerous models (i.e., Mioduszewski et al., 2019), the importance of regional sea ice changes for Greenland blocking activity could be reduced. However, the role of NAO in future Greenland blocking frequencies is uncertain because of model deficiencies.

Greenland blocking frequency changes over the past 20 years have had important impacts on GrIS net surface energy and snowmelt processes. During blocking activity, subsidence reduces cloud presence and leads to increased downwelling shortwave energy at the surface (Fig.

1.8; Rajewicz and Marshall, 2014; Lim et al., 2016; Mioduszewski et al., 2016; Hofer et al., 2017).

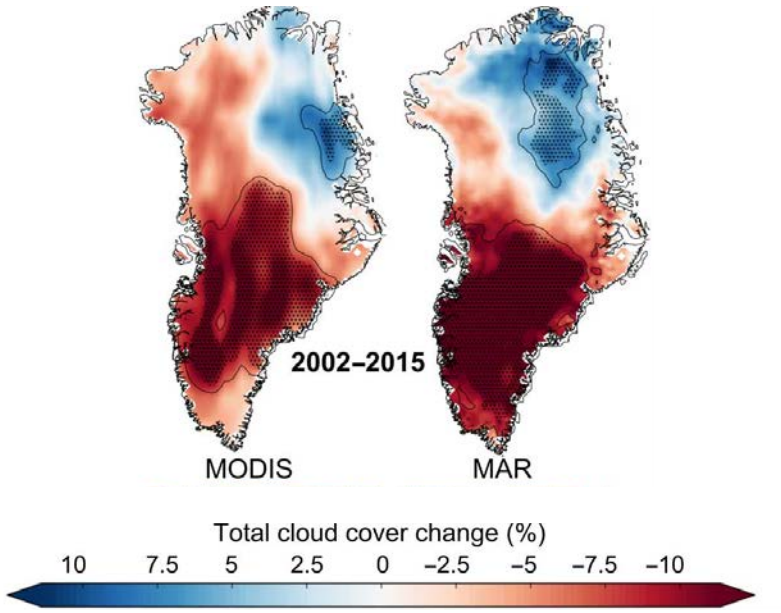

Fig. 1.8: Observational (MODIS) and modeled (MAR) evidence of average cloud coverage change between 2002-2015 (relative to average 1970-1995 modeled cloud coverage) resulting from increased Greenland blocking activity (courtesy of Hofer et al., 2017).

The locations of greatest cloud reduction (Fig. 1.8) correspond to the GrIS ablation zone that enhances net shortwave flux and perpetuates the ice-albedo feedback process. In order for net shortwave fluxes to enhance melt and albedo changes over the more reflective GrIS regions, melt must be triggered by other surface energy flux components.

The main melt trigger associated with Greenland blocking that enhances net surface energy flux is the advection of warm air onto the ice sheet (e.g., Fettweis et al., 2011, 2013). In addition to melt onset via the ice-albedo feedback process, this warm air produces downwelling sensible heat flux into the surface. These processes are spatially-variable over the GrIS. Snow aging and albedo reduction is the largest contributor to melt as a result of increased net shortwave energy over the accumulation zone (e.g., Franco et al., 2013) and northern Greenland

(e.g., Tedesco et al., 2016b), while sensible heating during blocking most frequently occurs over western Greenland (Franco et al., 2013; Fausto et al., 2016). Because the western GrIS ablation zone has low albedo, net shortwave energy and sensible heating inputs resulting from blocking contribute to large net surface energy gain, especially over the lower ablation zone (Franco et al., 2013; Fausto et al., 2016). Despite larger downwelling longwave energy fluxes produced by warm air advection (Hofer et al., 2017), negative longwave cloud radiative forcing and enhanced longwave emission from the warmer surface produce overall negative net longwave energy anomalies.

Although Greenland block subsidence reduces cloud coverage, horizontal airflow over the elevated GrIS can produce clouds through adiabatic cooling. Regional moisture transport induced by block circulation impacts GrIS surface processes outside of the high pressure center by promoting cloud growth (i.e., Johansson et al., 2017) and increasing latent heat flux into the surface. Moisture transport activity is highly correlated with Greenland blocking (i.e., Välisuo et al., 2018) and has increased in frequency over the last 20 years (Mattingly et al., 2016). Precipitation resulting from block-induced moisture transport can directly impact GrIS surface mass balance and energy exchange processes through snow accumulation, rainfall-induced runoff, and the associated surface albedo changes (Mattingly et al., 2018; Doyle et al., 2015).

The relative contributions of Greenland blocking energy flux changes, cloud formation, warm air transport, and moisture transport to GrIS melt processes is regionally variable because of GrIS topography. The studies that examine Greenland blocking-induced atmosphere-surface interactions do so by exploring seasonally-averaged blocking conditions (e.g., Lim et al., 2016; Mioduszewski et al., 2016; Hofer et al., 2017). Given the quasi-stationary nature of Greenland blocking (Chen et al., 2017), these GrIS surface processes likely vary with block location. The

importance of GrIS surface processes on global climate processes mandates that the impacts of different Greenland block locations should be better understood. Furthermore, the effects of future Greenland blocking on surface energy fluxes could change as GrIS albedo and mass decrease and regional atmospheric temperatures and moisture increase.

1.6 Specific Aims: Thesis Outline

Understanding how the GrIS responds to the short-term melt triggers discussed in section 1.5 is important for predicting GrIS mass balance and global sea level rise changes in a warmer climate. The general science question explored in this dissertation is: "How do light-absorbing aerosols, clouds, and Greenland blocking affect GrIS surface energy fluxes?". Chapter 2 (Ward et al., 2018) examines the impacts of light-absorbing aerosols like BC and dust on GrIS snowmelt and surface energy fluxes. The different responses of GrIS surface processes to atmospheric and in-snow aerosols are tested in a suite of model runs with varying prescribed aerosol content. These atmospheric and in-snow aerosol quantities are then combined in another suite of global climate model runs to understand their combined effects. Chapter 3 (Ward et al., 2020, submitted) focuses on how different Greenland block locations affect regional cloud coverage using observational cloud data. The combined impacts of these cloud changes and Greenland block-induced airflow are then examined to better understand how block location affects net surface energy fluxes. Finally, Chapter 4 (in preparation) examines how Greenland blocking surface energy fluxes could change in the future, as produced by global climate modeling.

Chapter 2. Modeled Response of Greenland Snowmelt to the Presence of Biomass Burning-Based Absorbing Aerosols in the Atmosphere and Snow

(Ward et al., 2018)

2.1 Introduction

One of the most important influences on Earth's climate system is the production, transport, and deposition of aerosols. These tiny solid or liquid particles can influence incoming solar radiation (insolation) directly through scattering and absorption, or indirectly by serving as cloud condensation nuclei (CCN) and generating clouds that reduce insolation at the surface. Although most aerosol species predominantly scatter insolation and cool the surface, some species strongly absorb insolation. Of these light-absorbing aerosols (LAA), black carbon (BC) has the highest absorptivity. BC is produced by the incomplete combustion of biomass, biofuels, or fossil fuels and tends to be emitted along with less absorptive species (Bond et al., 2013; Chung & Seinfeld, 2002; Hansen & Nazarenko, 2004; Koch et al., 2009; Ocko et al., 2012). The radiative and meteorological effects of BC are difficult to assess because the processes of emission, transport, and deposition distribute it heterogeneously across the globe (Liu et al., 2012; Ramanathan & Carmichael, 2008). As BC emissions continue to evolve in the future, regional atmospheric temperature and precipitation patterns could change in response (Menon et al., 2002).

BC is especially important for the climate system and local energy budget because it efficiently absorbs radiation in the visible wavelengths (0.4–0.7 μm), which make up the largest portion of energy emitted by the Sun (Bond et al., 2013; Koch et al., 2009). Through the direct aerosol effect, BC presence can lead to localized warming in the atmosphere or on the surface, affecting atmospheric stability, cloud formation, and sensible and latent heat fluxes at the surface (Ban-Weiss et al., 2011; Flanner, 2013; Ramanathan & Carmichael, 2008). Indirect effects of LAA that result from cloud formation can also significantly impact these processes. Unlike greenhouse gases, which warm the surface regardless of height in the atmosphere, the altitude of BC is important when considering its net energy impact at the surface. Regardless of its position, BC in the atmosphere leads to positive top-of-atmosphere forcing on a global scale due to its high absorptivity. Direct surface radiative forcing from BC in the atmosphere is negative because it reduces surface insolation. In an idealized modeling framework focusing on the Arctic, Flanner (2013) determined that the altitude of BC is an important factor for surface temperature response. Flanner's (2013) results indicate that BC suspended in the lowest portion of the atmosphere leads to surface warming. This surface warming decreases as BC is suspended at higher altitudes, eventually transitioning to surface cooling with BC suspended above roughly 450 hPa (Flanner, 2013). Haywood and Ramaswamy (1998), Ramanathan and Carmichael (2008), and Ban-Weiss et al. (2011) also note the importance of vertical aerosol distribution on surface processes.

Several processes and feedbacks impact the net effect of atmospheric aerosols. Localized atmospheric warming resulting from suspended BC can lead to cloud burn-off (i.e., cloud droplet dissipation). In this process, local air becomes unsaturated as a result of increasing air temperatures and cloud droplets evaporate (Ban-Weiss et al., 2011; Flanner, 2013; Ramanathan & Carmichael, 2008; Sand et al., 2013; Wang, 2004). BC-based warming can also lead to

changes in the vertical lapse rate of the atmosphere and local stability, depending on BC altitude. Within the aerosol layer, diabatic warming associated with the aerosols leads to local destabilization of the atmosphere and can result in cloud formation (Ban-Weiss et al., 2011; Wang, 2004). High-altitude BC often leads to atmospheric stabilization and inhibits convective low cloud formation as a result of warming the air aloft and cooling the surface (Ban-Weiss et al., 2011; Flanner, 2013). Decreased atmospheric stability results from the presence of deposited BC. Deposited BC leads to surface warming, resulting in steepening of the lower tropospheric adiabatic lapse rate and atmospheric destabilization (Ban-Weiss et al., 2011; Flanner, 2013).

LAA are especially influential on the climate of snow- and ice-covered polar regions. Flanner et al. (2007) determined that absorptive biomass burning and fossil fuel emissions led to Arctic air warming by $0.5 - 1.61℃$. This is large relative to the global emission-based warming of $0.10 - 0.15℃$ (Flanner et al., 2007). In-snow impurities like BC and dust also increase surface energy fluxes into the surface through snow-albedo feedback mechanisms. BC and dust darken the snow and enhance solar energy absorption at the surface. As a result of this extra energy, snowmelt and snow aging are enhanced (Hansen & Nazarenko, 2004). In the perennial snow that covers the GrIS, meltwater can cause impurities to percolate downward into the snowpack, though buried impurities can also become reexposed when overlying snow is removed, further reducing surface albedo (Painter et al., 2012). The outsize impact of LAA on high-albedo areas suggests that these aerosols could have a significant impact on the Greenland Ice Sheet (GrIS), a high albedo, perennially snow and ice covered surface, with implications for sea level rise. If the entire GrIS were to melt, projected sea level rise is estimated to be $7.4\ m$, which could lead to the destruction of populous coastal cities across the globe (Gregory et al., 2004; Hanna et al., 2008). One of the climatic factors that could enhance future GrIS melt is

altered presence of LAA in the Greenland region. BC and other LAA are transported to the GrIS through global circulation mechanisms and cyclonic storms. Measurements and simulations indicate that LAA transport to the Greenland region normally begins to increase in March, with concentrations peaking in the summer months before tapering off in autumn (Jiao et al., 2014; Polashenski et al., 2015). However, Greenland currently receives lower concentrations of BC than other Arctic locations (Jiao et al., 2014). As a land mass of perennial snow and ice cover, though, the GrIS is more susceptible to the effects of snow darkening than most other areas of the Arctic.

Biomass burning-based BC emissions contribute roughly 40% of all global BC emissions, which suggests that biomass burning is an important influence on global climate (Ramanathan & Carmichael, 2008). The frequency of sustained, extreme biomass burning depends on regional temperature and precipitation. Higher temperature and lower precipitation conditions are more conducive to larger-scale, uncontrollable fire activity. Boreal climates are warmer and drier now than they have been for much of the past 10,000 years (Kelly et al., 2013). Under future climate scenarios, it is predicted that fire frequency, burned area, severity, and fire season length will increase (Flannigan et al., 2009, 2013; Stocks et al., 1998). There is already evidence of fire-induced change across the circumboreal (Jolly et al., 2015; Soja et al., 2007). In addition to boreal forests, it has been predicted that biomass burning activity in other regions will also increase where fire suppression is not practiced (Marlon et al., 2013). For example, Spracklen et al. (2009) used global climate model-based meteorological output and stepwise regression techniques to test this hypothesis for the western United States. They found that the total land area affected by biomass burning will increase by 54% by the middle of the 21st century as a result of changing regional climate patterns (Spracklen et al., 2009). With increased

biomass burning activity, more BC could be emitted and transported to sensitive environments like the GrIS. The resulting BC could lead to greater GrIS snowmelt as a result of surface albedo reduction. We have observed that BC produced from biomass burning can be transported to the GrIS. Recent measurements of elevated GrIS BC have been shown to be coupled with high NH_4^+ mixing ratios, suggesting that these BC samples were produced from remote biomass burning events (Keegan et al., 2014; Polashenski et al., 2015). Thomas et al. (2017) confirmed that BC deposited on the GrIS in early August of 2013 originated from biomass burning activity in Quebec and western Canada using a combination of transport modeling, satellite data analysis, and snow pit measurements. Although the quantity of BC deposited from the fire activity cited by Thomas et al. (2017) could have led to significant GrIS albedo reduction, Polashenski et al. (2015) determined that this was not the case because the BC was buried by fresh snow days after its deposition. Given that sunlight intensity decreases in August, this magnitude of BC on the GrIS would have been more effective at reducing surface albedo if it had taken place in late spring or early summer (Polashenski et al., 2015). However, biomass burning is a key and uncertain source of Arctic LAA in the summer.

Although many studies have investigated the direct radiative forcing of BC and other LAA on a global scale (e.g., Ban-Weiss et al., 2011; Bond et al., 1998; Clark et al., 2015; Flanner et al., 2007; Jacobson, 2001, 2004; Wang, 2004) and in the Arctic (e.g., Flanner, 2013; Jiao et al., 2014; Sand et al., 2013; Wang et al., 2011) using various modeling techniques, the relative impacts of biomass burning-based atmospheric and deposited LAA on GrIS snowmelt have yet to be investigated. In this study, we use idealized global climate modeling techniques to examine the relative impacts of atmospheric and deposited LAA on GrIS snowmelt and surface energy fluxes from June through August. First, we describe the methods we use for setting up the

model simulations and analyzing the results in section 2.2. We then demonstrate how different aerosol concentrations and positional combinations lead to varying GrIS snowmelt and surface energy patterns in section 2.3. Finally, we summarize the results and implications of this research in the conclusion.

2.2 Methods

To explore the extent to which atmospheric and deposited LAA can affect GrIS snowmelt and other climatic conditions in the summer, we conduct four sets of experiments. The "AOD-ONLY" experiment varies atmospheric aerosol burden without any BC or dust in the GrIS snow. Similarly, we explore the effects of changing atmospheric aerosol single-scatter albedo (SSA) in runs with constant atmospheric aerosol burden ("Variable SSA" or "VSSA"). We analyze different SSA values because the ratio of BC to organic carbon (OC) in smoke depends largely on the biomass type being burned (Bond et al., 2013). OC is less absorptive than BC, so more OC in a smoke plume indicates higher SSA (Bond et al., 2013). We examine the climate effects of BC and dust deposited on the GrIS by changing in-snow aerosol mixing ratios and zeroing out all atmospheric aerosols in the "IN-SNOW" runs. Finally, to evaluate the effects of aerosols present simultaneously in the atmosphere and on the GrIS surface, we conduct the "BOTH" runs. Although BOTH more accurately depicts LAA conditions (i.e., high atmospheric LAA are required for high deposited LAA content), we conduct AOD-ONLY, VSSA, and IN-SNOW to isolate the climate impacts of LAA location. For all of these simulations, we use the Community Earth System Model (CESM), version 1.0.3. We apply CESM with a spatial resolution of 1.9° × 2.5° and a time step of 30 min. Although the spatial resolution may seem somewhat coarse, the land surface of Greenland is present in 121 grid cells that we use for our analysis. We

run each simulation for 11 model years and analyze monthly model output. To accommodate the time required for atmospheric equilibration, we discard the first year of each model simulation for spin-up purposes. Regardless of the experiment, the aerosol burdens and optical properties we specify at the start of each model run remain constant for the entire simulation. We specifically investigate the climate response during the summer (June, July, and August) because this is when Greenland receives the greatest amount of insolation. During these months, the direct radiative forcing that results from suspended LAA is responsible for air temperature enhancement throughout the troposphere (Screen et al., 2012). Although aged, hydrophilic BC can indirectly affect the propagation of radiation by serving as CCN, we do not address these effects on Greenland's climate in this study.

For each simulation, we couple Community Atmosphere Model 4.0 (CAM4) and Community Land Model 4.0 (CLM4) while prescribing annually repeating present-day climatological sea surface temperatures and sea ice. While the use of fixed sea surface temperatures does not capture the full climate response to aerosols, we use this setup because less model noise is produced, the model output contains less interannual variability, and less spin-up time is needed, all of which facilitate a more straightforward interpretation of the effects of aerosol loading above and on the GrIS. The SNow, ICe, and Aerosol Radiation model (SNICAR) is a standard component of CLM that we adapt for our experiments to simulate the radiative effects of aerosols in snow on the GrIS. SNICAR is a two-stream, multilayer, multiple-scattering radiative model (e.g., Flanner & Zender, 2005). SNICAR calculates surface albedo and vertical heating in the snowpack using solar zenith angle, ice effective grain size, and BC, OC, and dust mass concentrations (Oleson et al., 2010). Snow grains and impurities are represented as spheres for Mie calculations that are used in the two-stream setup (Oleson et al.,

2010). Although SNICAR normally diagnoses impurity mass changes in each snow layer associated with new snowfall and meltwater percolation, we choose to maintain constant mass mixing ratios in each layer for experiments conducted here, ensuring consistency with our imposition of constant aerosol burdens in the atmosphere.

Because the purpose of this study is to isolate the climate effects of LAA above and on the GrIS, we prescribe identical three-dimensional climatological aerosol fields (Lamarque et al., 2010) outside of Greenland in all experiments. We define the Greenland area to span land within latitude and longitude ranges of $60 - 85°N$ and $20 - 60°W$ respectively. Within this region, we manually vary atmospheric and terrestrial aerosol burdens, as well as aerosol SSA. For the atmospheric aerosol simulations, we impose a specific aerosol burden in the lowest five vertical layers of CAM, or approximately the lowest 2 km of the atmosphere overlying the GrIS. All aerosols are zeroed out above the lowest five atmospheric layers in CAM. Although we could perform additional simulations with LAA placed at different altitudes above Greenland, we do not explore the vertical dimension in this study. Flanner (2013) finds that air temperature and net radiation at the surface decrease as the altitude of BC increases. Given the similar setup to their study, we hypothesize that this would also be the case for our AOD-ONLY simulations. It is important to emphasize that the aerosols within this Greenland region are not advected by the model. Instead, aerosol quantities and properties that we define remain constant over all of the Greenland region throughout the entire simulation.

To determine how varying atmospheric LAA burdens affect GrIS snowmelt, we specify aerosol optical depth (AOD), or the opacity associated with the suspended particles, over the entire Greenland region. Functionally, we achieve this by setting the burdens of hydrophobic BC and OC, each of which have unique values of mass extinction cross section and SSA, to the exact

quantities that achieve the desired AOD and SSA. We distribute their total burdens evenly among the five lowest atmospheric layers of CAM. Suspended BC and OC burdens are also distributed uniformly across the Greenland region. All other aerosol species are absent from Greenland's atmosphere. We choose AOD as a proxy for aerosol concentration because much of the available atmospheric aerosol data over Greenland are measured in terms of AOD. We examine the climate response to atmospheric aerosols by changing AOD while maintaining constant aerosol SSA in the AOD-ONLY simulations. We note again that the imposed aerosols do not directly affect cloud microphysics. These LAA only affect the propagation of radiation through the atmosphere, which subsequently impacts diabatic heating and bulk thermodynamic processes. The choice of values for the AOD-ONLY cases is based on AOD measurements taken by Strellis et al. (2013) over Summit, Greenland, in the summer of 2011. These measurements were taken using handheld Sun photometers; AOD = 0.09 ± 0.03 (used in case AOD = 0.09) was the average value over the entire summer, and AOD = 0.21 (used in case AOD = 0.21) was the maximum measurement (Strellis et al., 2013). Based on in situ scattering measurements that Strellis et al. (2013) also took over Summit, the average SSA of the suspended aerosols was 0.93 ± 0.03. We incorporate these measurements in our AOD-ONLY runs by imposing constant SSA = 0.93 in every case. We also consult other Arctic-based AOD measurements to establish extreme scenarios of aerosol loading associated with high-impact biomass burning events. Using measurements taken over select Arctic locations during the summer of 2004, Stohl et al. (2006) determined that the average AOD of LAA produced by extensive remote biomass burning activity was 0.50, which we use for our third AOD-ONLY case. For the final two AOD-ONLY cases, we set extremely high AOD values of AOD = 0.75 and AOD = 1.0, which are 50% and 100% larger than the AOD = 0.50 case, respectively. Thomas et al. (2017) showed that for

intense fires 550 nm AOD values (Moderate Resolution Imaging Spectroradiometer [MODIS] Aqua) were close to 1 over the source fires in Canada and over Hudson Bay in summer 2013. However, detection of AOD over the Greenland ice sheet during fire event was limited by cloud cover. Although aerosol extinction associated with AOD > 0.50 has not been measured in the generally pristine Greenland atmosphere, we simulate the unrealistic AOD = 0.75 and AOD = 1.0 cases to achieve high signal-to-noise ratios and more wholly characterize the sensitivity of Greenland's climate to atmospheric LAA. The values of aerosol properties that we use for all of our simulations are shown in Table 2.1. Given the measured range of SSA values by Strellis et al. (2013), we conduct two additional runs with AOD = 0.50 and varying SSA values (i.e., SSA = 0.90 and SSA = 0.96) in the VSSA experiment to examine how changing SSA affects Greenland's climate (Table 2.1).

Because aerosols also darken snow surfaces after being deposited, we run a suite of five IN-SNOW simulations to assess the effects of LAA deposited on the GrIS. In these simulations, we vary BC and dust mixing ratios in snowpack based on measured and theoretical values. We include dust in our simulations because dust also contributes to the absorption of sunlight in snow (Painter et al., 2007). Unlike with the AOD-ONLY and VSSA experiments, we represent deposited LAA quantities as mixing ratios because these are the quantities for which we have measurements. Although we specify BC and dust mixing ratios throughout the entire snow column, we note here that it is the presence of LAA only in the top several centimeters of snow that causes most of the sunlight absorption. We simulate BC with a number mean radius of 50 nm using one size bin. We distribute specified dust mixing ratios among the four size bins applied by SNICAR, with lognormal size functions partitioned into each of the bins. The minimum particle sizes of these four bins are 0.01, 1.0, 2.5, and 5.0 μm, and the corresponding

volume fractions for the assumed size distribution are 44.53%, 43.66%, 10.37%, and 1.45%, respectively.

To concisely represent the total amount of LAA in snow, we refer to the combined mixing ratios of BC and dust in this discussion using a black carbon equivalent (BCE) metric with units of ng/g:

$$\mathrm{BCE} = [\mathrm{BC}] + \sum_{i=1}^{4} \left([\mathrm{Dust}]_i * \frac{\mathrm{MAC}_{\mathrm{Dust,i}}}{\mathrm{MAC}_{\mathrm{BC}}} \right) \quad (2.1).$$

In this equation, [BC] is the mixing ratio of BC, $[\mathrm{Dust}]_i$ is the mixing ratio of dust in size bin *i*, and the mass absorption cross sections (MACs) for dust in bin *i* and BC are $\mathrm{MAC}_{\mathrm{Dust,i}}$ and $\mathrm{MAC}_{\mathrm{BC}}$, respectively. This metric represents the equivalent BC mixing ratio when we take into account the MAC of BC and dust for each aerosol bin that are based on calculations performed by SNICAR. The BC and dust mixing ratios for each case are listed with the corresponding BCE values in Table 2.1.

Table 2.1: LAA Model Input for each Experiment[a]

Experiment	**BOTH**				**VSSA****
	AOD-ONLY*	**IN-SNOW**			
Rank	*AOD*	*BC (ng/g)*	*Dust (ng/g)*	*BCE (ng/g)*	*SSA*
1	0.09	2.6	54.8	2.7	0.90
2	0.21	15	328	15.7	0.93
3	0.50	58.8	1360	61.8	0.96
4	0.75	88.2	2040	92.8	--
5	1.00	117.6	2720	123.7	--

* $SSA = 0.93$ for each case.
** $AOD = 0.50$ for each case.
[a]AOD, BC and Dust mixing ratios (and the associated BCE for each case), and SSA values used in CESM for AOD-ONLY, IN-SNOW, BOTH, and VSSA simulations.

We first consult measurements taken by Polashenski et al. (2015) from snow pits dug in northwestern Greenland during early summer 2013 and August 2014 to constrain mixing ratios. Although Polashenski et al. (2015) directly measured BC mixing ratios within each snow pit,

they were only able to measure mixing ratios of individual ions and element components of dust. Based on previous research and their findings, Polashenski et al. (2015) determined that the ratio of Ca^{2+} to dust concentration ranges from 0.21 to 0.29. Therefore, we multiply their Ca^{2+} mixing ratio measurements by a factor of 4 to infer the dust mixing ratios we impose on the GrIS. Per Polashenski et al. (2015), the lowest BC and dust mixing ratios we use for the IN-SNOW scenario (i.e., BCE = 2.7 ng/g) are representative of average snow pit LAA mixing ratio measurements. The elevated snow pit BCE value based on BC and dust measurements reported by Polashenski et al. (2015) is 15.7 ng/g, which we use as our second IN-SNOW case. Based on maximum values of additional measurements taken on the GrIS in the early 2000s, we set our third IN-SNOW case BCE as 61.8 ng/g (Bory et al., 2003; McConnell et al., 2007). To achieve a stronger signal and again explore the linearity of climate response to very large mixing ratios of LAA in Greenland snow, we increase the BC and dust mixing ratios from the BCE = 61.8 ng/g run by 50% (BCE = 92.8 ng/g) and 100% (BCE = 123.7 ng/g) for the final IN-SNOW simulations.

Finally, we combine the AOD values from AOD-ONLY scenario with BC and dust mixing ratios from the IN-SNOW cases in the BOTH experiment. Because the AOD-ONLY and IN-SNOW experiments each contain five cases, we match up the associated burdens in each experiment from lowest to highest. The purpose for conducting this suite of runs is to explore the net effects and potential nonlinear responses of atmospheric and in-snow LAA acting in combination, which may differ from the sums of individual impacts identified from AOD-ONLY and IN-SNOW cases. Like in the AOD-ONLY scenario, we maintain SSA = 0.93 for suspended aerosols in all BOTH model runs.

We calculate changes in Greenland's climate attributable to aerosol presence by comparing all of the aforementioned runs to a control simulation. We define this control simulation, termed CONTROL, to have AOD = 0 and an in-snow BCE of 0 ng/g within the Greenland region. The model boundary conditions and specified aerosol concentrations outside of Greenland for CONTROL are the same as the variable runs. For each simulation, we find differences in temperature, snowmelt, and energy fluxes by calculating $\Delta Var = Var_{CASE} - Var_{CONTROL}$, where Var is the variable of interest and CASE is one of the non-CONTROL simulations. Furthermore, we test for statistically significant differences between each case and CONTROL by using two-sample t test calculations. This test is done for each grid cell over the Greenland region, as well as on spatially averaged data. All of our statistical calculations involve n = 10 summer seasons that are analyzed. For this analysis, we require a confidence interval of 95% for a run to be significantly different from CONTROL ($p \leq 0.05$). To maintain consistency when determining area-weighted spatial averages of the climate state for each case, we filter out sea-based grid cells by using the CESM landfrac field, which provides the fraction of land present in each grid cell. We use a threshold landfrac ≥ 0.83 to define the land mass of Greenland in order to exclude data from nearby Iceland. In the case of the grid-by-grid statistical analysis, though, we do not take land fraction into account.

2.3 Results and Discussion

In this section, we examine how temperature, snowmelt, and surface energy fluxes change with increasing atmospheric and deposited aerosol loads. First, we compare how air temperature changes vertically with respect to CONTROL for different AOD, SSA, and in-snow LAA mixing ratios. Next, we discuss snowmelt rate changes for the different LAA experiments

using two-dimensional difference maps and spatially averaged statistics. We then show how changes in the surface energy balance relative to CONTROL explain simulated differences in snowmelt. Finally, to explain the GrIS-averaged sign of change in surface energy flux, we examine each component of the surface energy balance.

2.3.1 Vertical Temperature Profile Deviations

To gain a better understanding of the different physical mechanisms that lead to changes in melt for all aerosol experiments, we first examine changes in vertical profile air temperature in the lower troposphere. For this portion of the analysis, we average three-dimensional temperature data horizontally over Greenland. The vertical temperature difference (ΔT) plots for all atmospheric and deposited aerosol cases are shown in Fig. 2.1, where the vertical coordinate represents the mean height above the GrIS surface of each hybrid sigma-pressure layer within CAM.

From these plots, we see that increasing atmospheric LAA presence causes localized warming within the aerosol layer as a result of the direct absorption of sunlight. We observe this warming in the AOD-ONLY and VSSA experiments. When we maintain constant SSA in the AOD-ONLY experiment, we find that ΔT increases monotonically with higher atmospheric aerosol content through the lowest 1.5 km of the troposphere. We determine that decreasing SSA (i.e., increasing aerosol absorptivity) for the VSSA runs also leads to a monotonic increase in ΔT in the same altitude range. However, temperature change at the surface (ΔT_s) is lower than ΔT within the aerosol layer because of surface dimming for all AOD-ONLY and VSSA cases. Above the aerosol layer, ΔT is lower and remains positive through 7 km for all AOD-ONLY cases and the VSSA cases with SSA ≤ 0.93. The SSA = 0.96 case depicts non-significant

negative ΔT just above 2 km because there is less sunlight absorption inside the aerosol layer so less heat energy is transferred to higher altitudes.

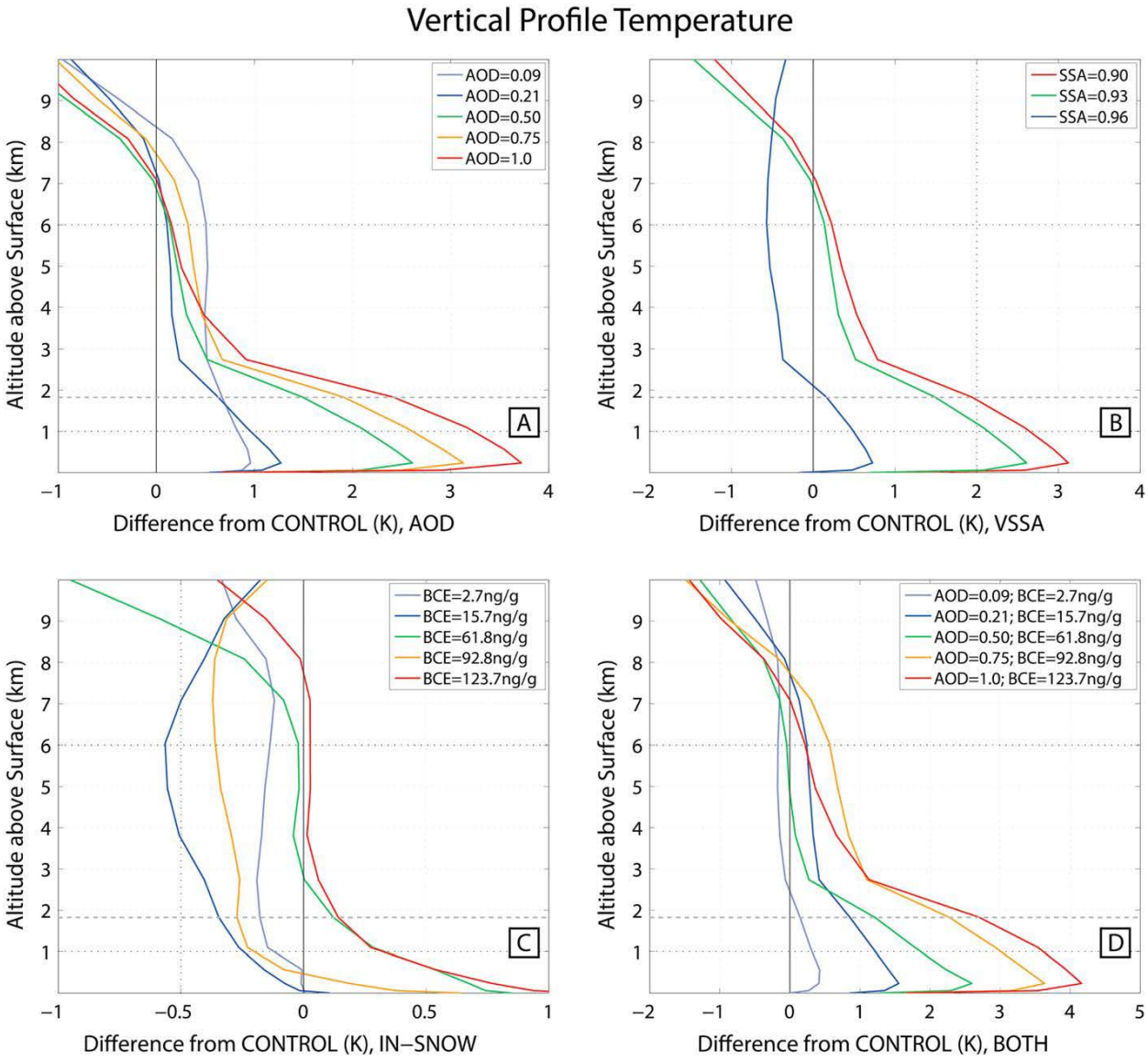

Fig. 2.1: Spatially-averaged vertical profile difference plots for tropospheric air temperature, relative to CONTROL, for (A) AOD-ONLY, (B) VSSA, (C) IN-SNOW, and (D) BOTH simulations. The horizontal dashed line at ~2km represents the upper-most LAA altitude for the atmospheric aerosol runs.

In contrast to the AOD-ONLY and VSSA experiments, ΔT is positive at the surface and decreases with height for all but the smallest of the IN-SNOW runs. With the exception of the BCE = 92.8 ng/g case, we determine that ΔT_s increases monotonically as we increase BC and dust mixing ratios. Insolation is more readily absorbed at the surface as albedo decreases because of the "in-snow" direct aerosol effect, resulting in surface and lower atmospheric warming. Although we do not observe any surface temperature change for BCE = 2.7 ng/g (i.e., $\Delta T_s \approx 0$), we suspect that this is simply because there is not enough BC and dust in the snow to trigger substantial "in-snow" direct aerosol effect. Despite ΔT_s being lower for the BCE = 92.8 ng/g case than BCE = 61.8 ng/g, the difference is not statistically significant, so we attribute this non-monotonic behavior to model noise. For all IN-SNOW runs, we find that only the unreasonably large BCE = 123.7 ng/g case results in significant ΔT_s. Without the effects of atmospheric aerosols in IN-SNOW, ΔT steadily decreases with altitude because anomalous heating originates at the Earth's surface. We note here that we find negative, decreasing ΔT with height through most of the atmosphere for BCE = 15.7 ng/g. We attribute this to model noise and variability since no ΔT are statistically significant.

Like in the AOD-ONLY and VSSA experiments, ΔT in the BOTH experiment increases monotonically with LAA amount in the aerosol layer and on the surface. All but the AOD = 0.09; BCE = 2.7 ng/g BOTH runs maintain low positive ΔT from the top of the aerosol layer through 7 km, as we see in AOD-ONLY and VSSA. We calculate larger ΔT for the BOTH AOD = 1.0; BCE = 123.7 ng/g case than the AOD = 1.0 AOD-ONLY case because of the combined warming effects of atmospheric and deposited LAA.

2.3.2 GrIS Snowmelt (QMELT) Deviations

The ΔT trends we discuss in the previous section illustrate how suspended and deposited aerosols affect air temperature at the surface and in the lower atmosphere. These ΔT patterns, along with surface energy flux changes described later, influence snowmelt difference (ΔQMELT) patterns across the GrIS. To explore the ΔQMELT patterns that result when we impose different aerosol loads, we analyze the statistical results and plots of two-dimensional and spatially averaged ΔQMELT (Figs 2.2 and 2.3, respectively). We note that there is positive melt on the central GrIS for CONTROL with surface air temperature below 265K (8K below freezing). These QMELT results (not shown) are unusual because the central GrIS rarely experiences melt during the summer months (e.g., Nghiem et al., 2012). We hypothesize that the snowmelt at temperatures below freezing over central Greenland in the model could lead to overestimations of QMELT.

The effect of atmospheric aerosols on ΔQMELT varies based on both aerosol prevalence and SSA. In the AOD-ONLY and VSSA cases, we find that none of the melt patterns are statistically different from CONTROL (Figures 2 and 3). However, despite the small snowmelt changes, certain patterns do emerge with changing AOD and SSA. First, we observe slightly positive ΔQMELT around the periphery of the GrIS for lower AOD values (AOD $\leq$ 0.50). The enhanced marginal melt rates of the AOD-ONLY runs are caused by a combination of the warming lower troposphere and the absence of substantial surface dimming. We also observe this trend for the SSA = 0.90 and SSA = 0.93 VSSA cases. In contrast to the GrIS margins, however, we observe ΔQMELT $\leq$ 0 over the central portion of the ice sheet in these AOD-ONLY and VSSA simulations.

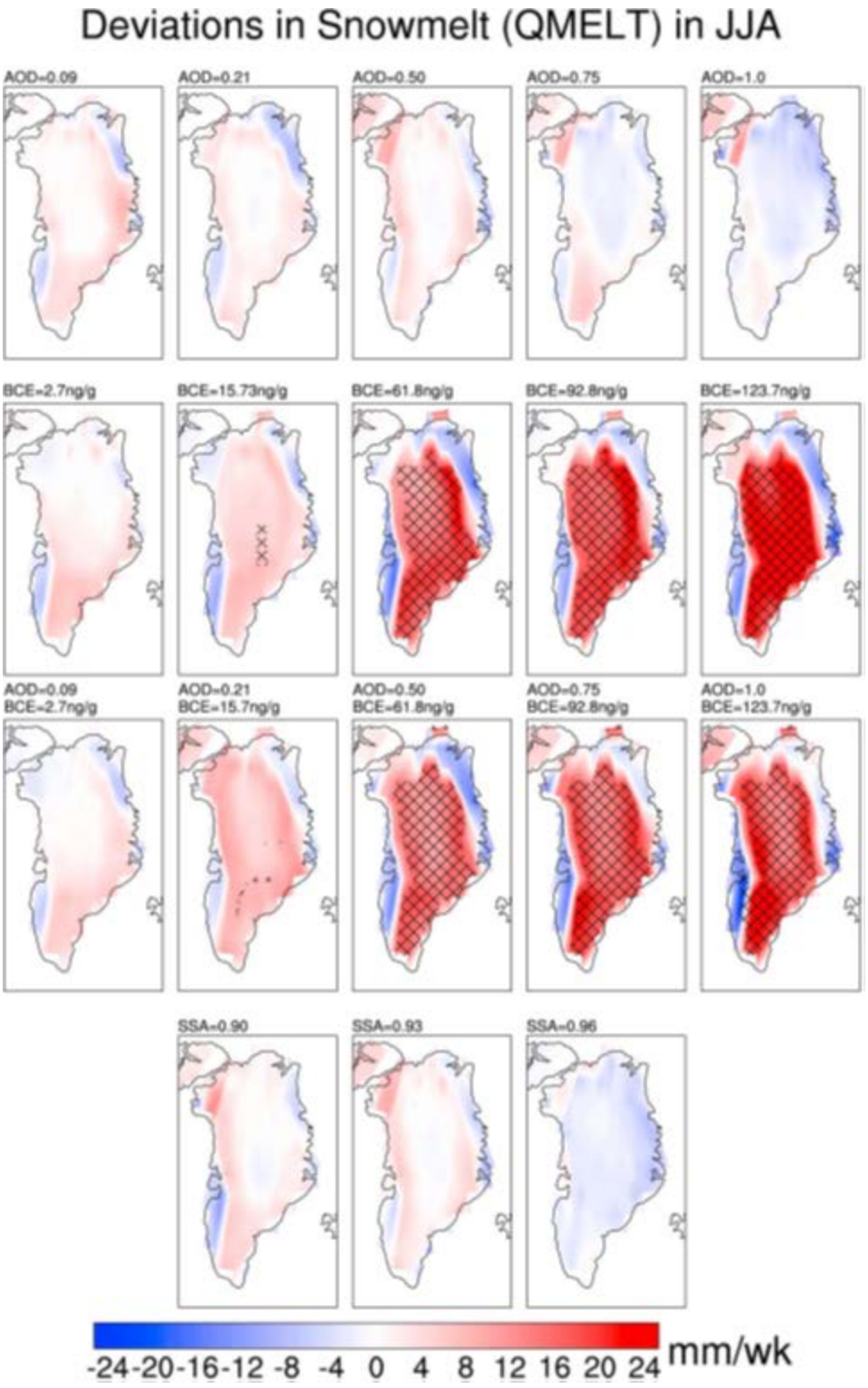

Fig. 2.2: ΔQMELT for the (first row) AOD-ONLY, (second row) IN-SNOW, (third row) BOTH, and (fourth row) VSSA experiments.

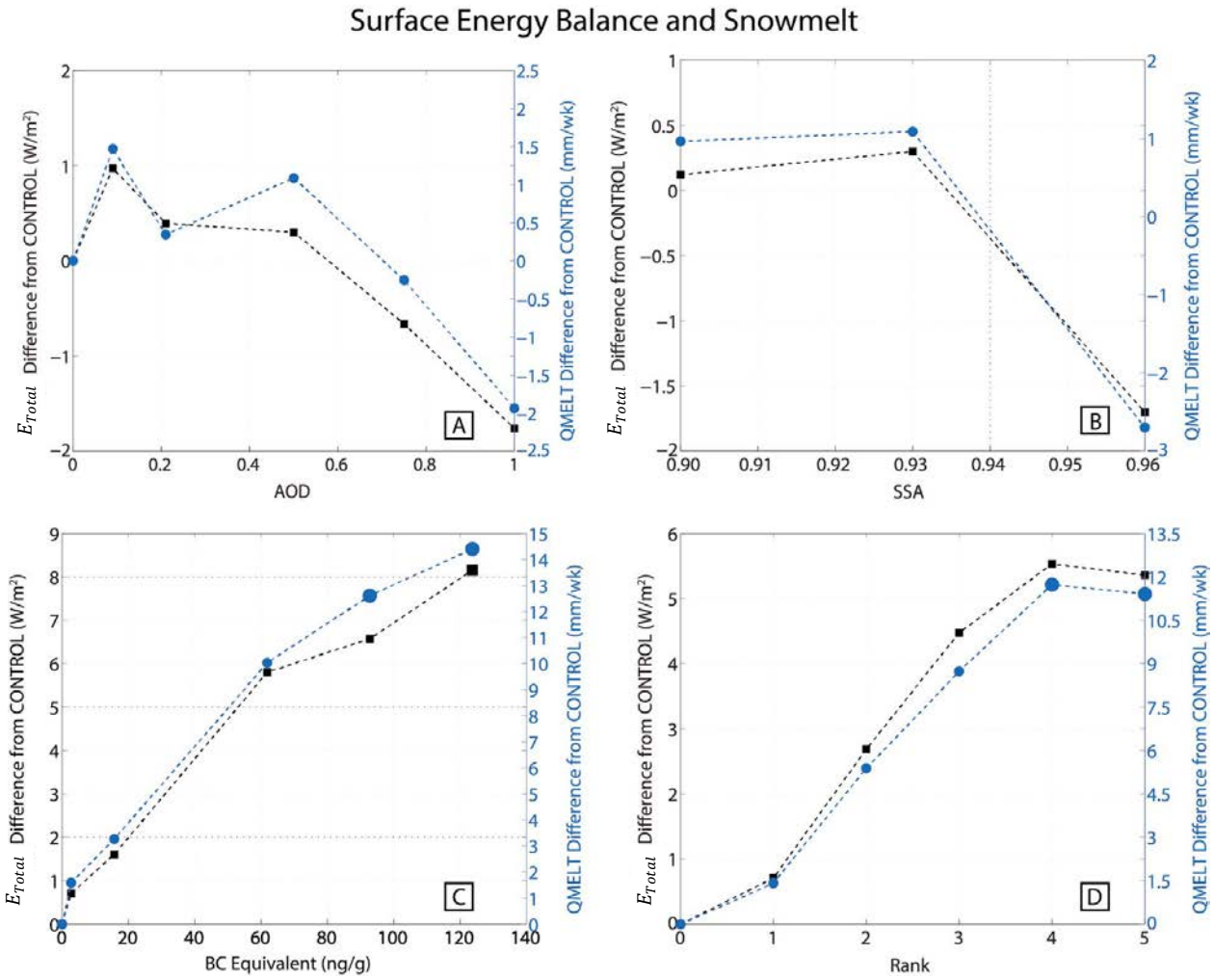

Fig. 2.3: Spatially averaged snowmelt (QMELT) and net surface energy (E_{Total} changes relative to CONTROL for the (a) AOD-ONLY, (b) VSSA, (c) IN-SNOW, and (d) BOTH experiments.

Even with the direct aerosol effect enhancing air temperature within the aerosol layer, the amount of energy that is transferred to the surface is not large enough to induce positive snowmelt changes. The unrealistically large AOD (i.e., AOD ≥ 0.75) and SSA = 0.96 cases produce mostly negative snowmelt change (i.e., less melting) over the GrIS. For the AOD = 0.75 and AOD = 1.0 runs, the effects of excessive surface dimming and limitations on sensible heat transfer from the warmed atmosphere lead to less total energy reaching the surface (Flanner, 2013). The negative ΔQMELT we observe over the entire GrIS in the SSA = 0.96 case results

from increased solar irradiance being scattered by the aerosols away from the surface, combined with minimal atmospheric heating.

By increasing in-snow BC and dust mixing ratios, we see that ΔQMELT for the IN-SNOW experiment increases across the GrIS. Furthermore, in all but the lowest IN-SNOW case, significant positive ΔQMELT occurs at some location on the GrIS, with the cases defined by BCE ≥ 61.8 ng/g having significant snowmelt changes almost everywhere. Because deposited LAA lowers the GrIS snow albedo, enhanced melt is expected (e.g., Warren & Wiscombe, 1980). However, based on historical in-snow BC and dust measurements, we emphasize that the high LAA presence associated with cases depicting significant melt on any large scale are very rare. The largest BC mixing ratio measured in a central Greenland ice core dating back to 1788 was 58.8 ng/g and only occurred once during this time span (McConnell et al., 2007). In our simulations, this corresponds to the BCE = 61.8 ng/g case. We emphasize that the BCE = 92.8 ng/g and BCE = 123.7 ng/g mixing ratios have never been observed in Greenland snow or ice (i.e., Doherty et al., 2010; McConnell et al., 2007; Polashenski et al., 2015). Warming snow and increasing snowmelt also trigger an acceleration of snow aging, where snow grain sizes increase as a result of vapor redistribution, melting and refreezing of water. Enlarged snow grains enable greater albedo perturbation from LAA in snow (Flanner et al., 2007). For all of the IN-SNOW simulations, we find that the northeastern and southwestern margins of the GrIS experience negative ΔQMELT. We determine that this is caused by an average decrease of snow depth (as measured by liquid water depth equivalent; see Figure 2.4) in the equilibrium state of the simulations. With less snow available for melting, the rate at which melt occurs after reaching equilibrium decreases.

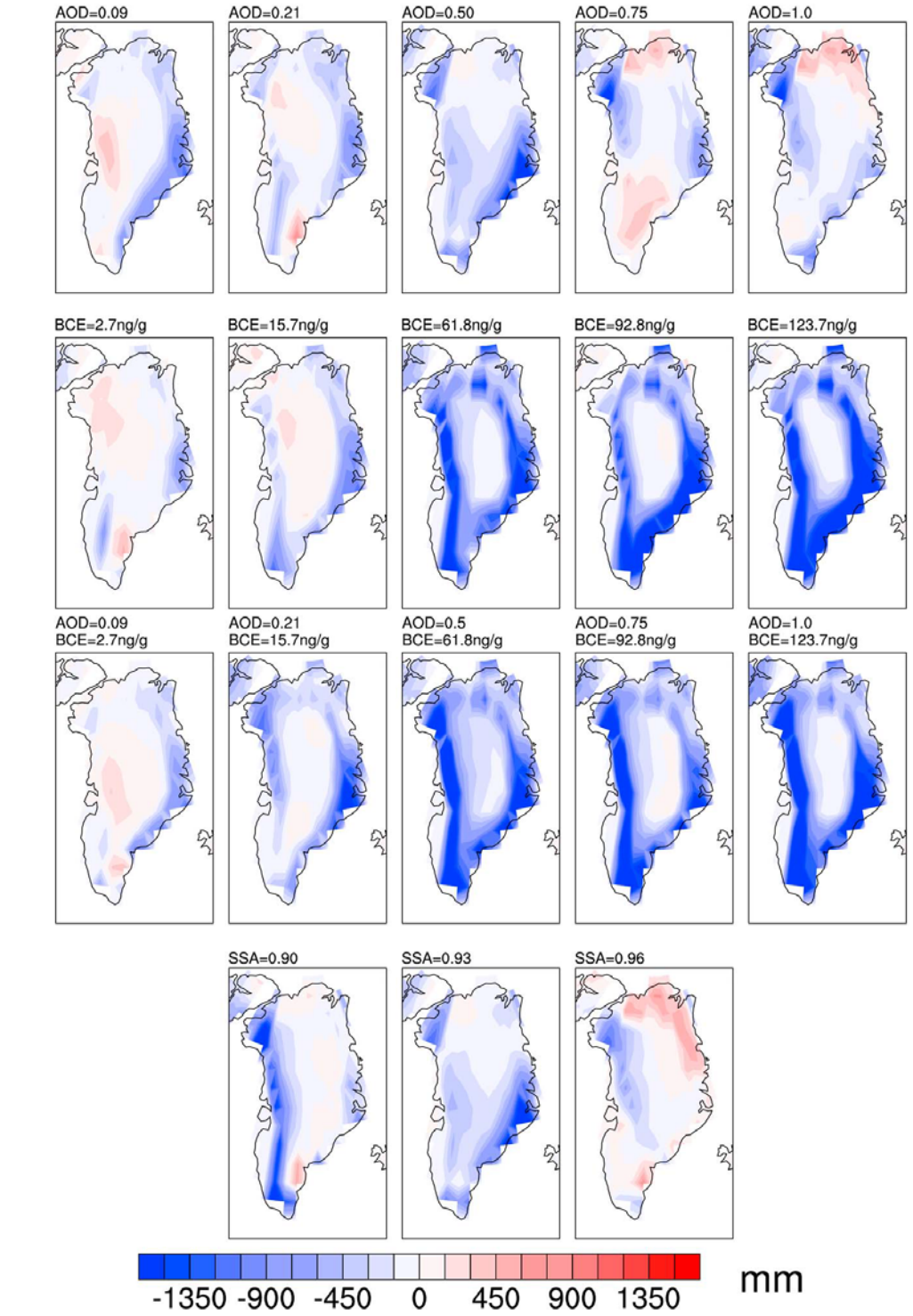

Fig. 2.4: Change in GrIS snow water equivalent with respect to CONTROL for the AOD-ONLY, IN-SNOW, BOTH, and VSSA cases.

The ΔQMELT spatial patterns and statistical results we find for the BOTH cases are very similar to those of the IN-SNOW experiment. However, despite the strong feedback associated with deposited aerosols, the effects of atmospheric aerosols do reduce the rate at which ΔQMELT increases for the BOTH runs. When we compare ΔQMELT between the IN-SNOW and BOTH simulation suites, $\Delta QMELT_{BOTH} < \Delta QMELT_{IN\_SNOW}$ (compare the lower panels of Figure 3). In the BOTH scenario, some of the surface heating from deposited LAA is counteracted by the dimming effects of atmospheric aerosols. We can see that the magnitude of ΔQMELT across most of the GrIS is slightly lower for the BOTH experiment than the IN-SNOW experiment (Fig. 2.2).

Based on the ΔQMELT trends we see with increasing atmospheric aerosol burden and in-snow aerosol mixing ratios, we can conclude from these modeling experiments that snowmelt of the GrIS is more sensitive to the presence of deposited aerosols than atmospheric aerosols when both are varied similarly in relation to their mean and extreme observed values. We can see from the surface energy balance values shown in Figure 2.3 that deposited aerosols are more effective at enhancing melt because surface energy flux increases ubiquitously as in-snow LAA mixing ratios are increased. The sign of impact that atmospheric aerosols have on the surface energy balance is less clear because of the competing effects of surface dimming, tropospheric warming, and potential indirect cloud feedbacks.

2.3.3 Surface Energy Budget Changes

Although snowmelt rates respond to changing surface air temperature (compare Figs 2.1 and 2.3), the extent to which snow surfaces with temperatures close to melting can warm is limited. However, because large surface energy fluxes can lead to large changes in snowmelt

with little change in surface temperature, we expect a more direct relationship between ΔQMELT and net surface energy flux changes (ΔE_{Total}). To determine ΔE_{Total} for each model simulation, we sum the following vector energy quantities at the surface: net solar flux ($\Delta SW_{net} = \Delta\left(SW^{\downarrow} - SW^{\uparrow}\right)$, where $SW^{\downarrow}$ and $SW^{\uparrow}$ are incoming and outgoing solar energy, respectively), net longwave energy flux ($\Delta LW_{net} = \Delta\left(LW^{\downarrow} - LW^{\uparrow}\right)$ for longwave energy flux, LW), net sensible heat flux (ΔSH), and net latent heat flux (ΔLH). For each of the energy flux components, we assume that positive energy fluxes are directed at the surface and negative energy fluxes flow upward from the surface (e.g., $SW^{\uparrow}$ and $LW^{\uparrow}$ are negative in each calculation). We compute the grid-by-grid ΔE_{Total} as follows:

$$\Delta E_{Total} = \Delta SW_{net} + \Delta LW_{net} + \Delta SH + \Delta LH \quad (2.2).$$

As we can see from the Greenland maps, spatially averaged plots, and the statistical results (Figures 2.5 and 2.2 and Table 2.2, respectively), ΔE_{Total} and ΔQMELT are very similar for each experiment. For the AOD-ONLY simulations, ΔQMELT and ΔE_{Total} initially increase with lower atmospheric aerosol burdens before becoming negative due to strong surface dimming. In the VSSA experiment, average snowmelt and net surface energy decrease with highly scattering atmospheric aerosols but remain slightly positive when SSA ≤ 0.93. In contrast to the purely atmospheric aerosol cases, increasing in-snow BC and dust mixing ratios leads to increasing ΔQMELT and ΔE_{Total} as a result of decreasing surface albedo. Based on these results, we can state with a good degree of certainty that changes in surface energy dictate melt pattern changes. However, the changes in each energy component with additional aerosol cannot be determined from this information alone. We can use the relative magnitudes of solar and turbulent energy fluxes in ΔE_{Total} to determine how each of these fluxes are influenced by changes in LAA abundance, location, and optical properties (Fig. 2.6).

Deviations in Net Surface Energy Flux (E_{Total}) in JJA

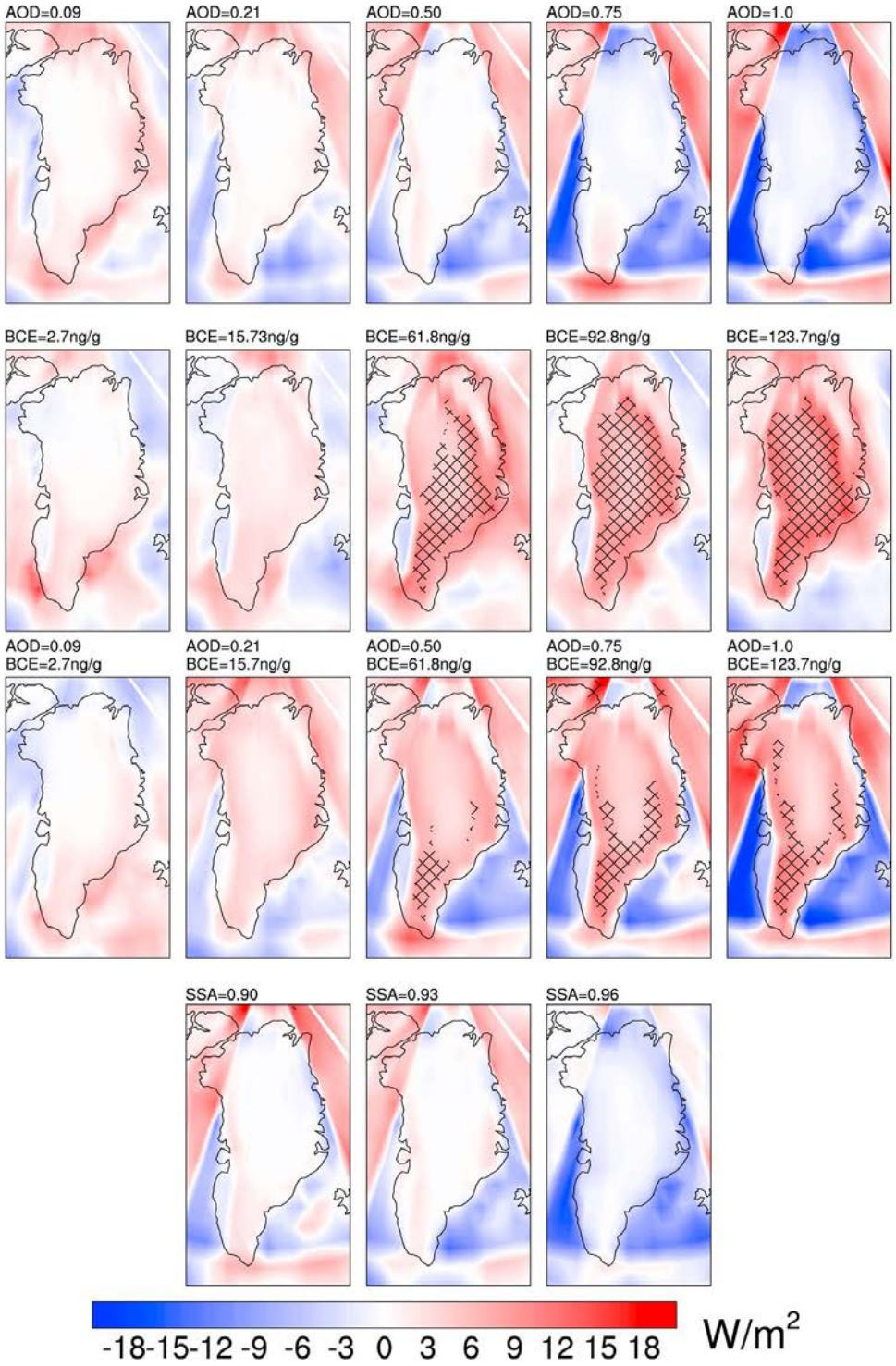

Fig. 2.5: ΔE_{Total} for the AOD-ONLY, IN-SNOW, BOTH, and VSSA experiments.

Table 2.2: Net Surface Energy Component Differences[b]

Experiment		ΔSW_{net}		ΔLW_{net}		ΔSH	ΔLH
Aerosol Scenario	*Case*	$\Delta SW^{\uparrow}$	$\Delta SW^{\downarrow}$	$\Delta LW^{\uparrow}$	$\Delta LW^{\downarrow}$	--	--
AOD-ONLY (*AOD*=) *(for SSA=0.93)*	0.09	0.93		-1.53		1.20	0.36
		6.98	-6.04	-2.64	1.11	--	--
	0.21	0.24		-2.82		2.02	0.95
		12.95	-12.71	-2.36	-0.46	--	--
	0.50	-0.25		-6.59		4.61	2.53
		24.50	-24.75	-3.05	-3.54	--	--
	0.75	-4.13		-5.52		5.53	3.67
		34.11	-38.24	-2.96	-2.56	--	--
	1.0	-5.49		-6.55		6.43	4.21
		42.42	-48.27	-2.87	-3.69	--	--
VSSA (*SSA*=) *(for AOD=0.50)*	0.90	-2.19		-5.24		4.60	2.95
		32.09	-34.28	-4.50	-0.74	--	--
	0.96	-4.90		-1.22		2.47	1.95
		19.62	-24.52	0.65	-1.87	--	--
IN-SNOW (*BCE* (*ng/g*)=)	2.7	3.21		-1.86		-0.43	-0.21
		0.31	2.91	-0.08	-1.77	--	--
	15.7	3.81		-0.23		-1.39	-0.59
		7.46	-3.65	-0.49	0.27	--	--
	61.8	11.65		-2.38		-1.61	-1.86
		18.87	-7.22	-3.78	1.39	--	--
	92.8	11.52		-0.62		-2.39	-1.95
		23.69	-12.16	-2.81	2.19	--	--
	123.7	14.50		-1.37		-2.60	-2.37
		28.37	-13.87	-5.16	3.79	--	--
BOTH (*AOD*, *BCE* (ng/g)=)	0.09; 2.7	1.99		-2.60		0.89	0.43
		5.92	-3.93	-0.06	-2.53	--	--
	0.21; 15.7	3.13		-2.68		1.42	0.82
		19.11	-15.98	-3.78	1.09	--	--
	0.50; 61.8	7.29		-6.13		2.15	1.16
		39.36	-32.07	-5.62	-0.51	--	--
	0.75; 92.8	5.36		-5.82		3.62	2.38
		51.97	-46.61	-7.18	1.36	--	--
	1.0; 123.7	6.20		-8.07		4.39	2.84
		60.45	-54.24	-7.23	-0.84	--	--

[b]Differences (in units of W/m^2) are with respect to CONTROL. Positive ΔSW_{net}, ΔLW_{net}, ΔSH, and ΔLH depict energy flow into the surface. Gray boxes highlight statistical significance. $\Delta SW^{\uparrow} < 0$ and $\Delta LW^{\uparrow} < 0$ indicate increased upwelling in the variable case, while $\Delta SW^{\downarrow} < 0$ and $\Delta LW^{\downarrow} < 0$ indicate less downwelling energy.

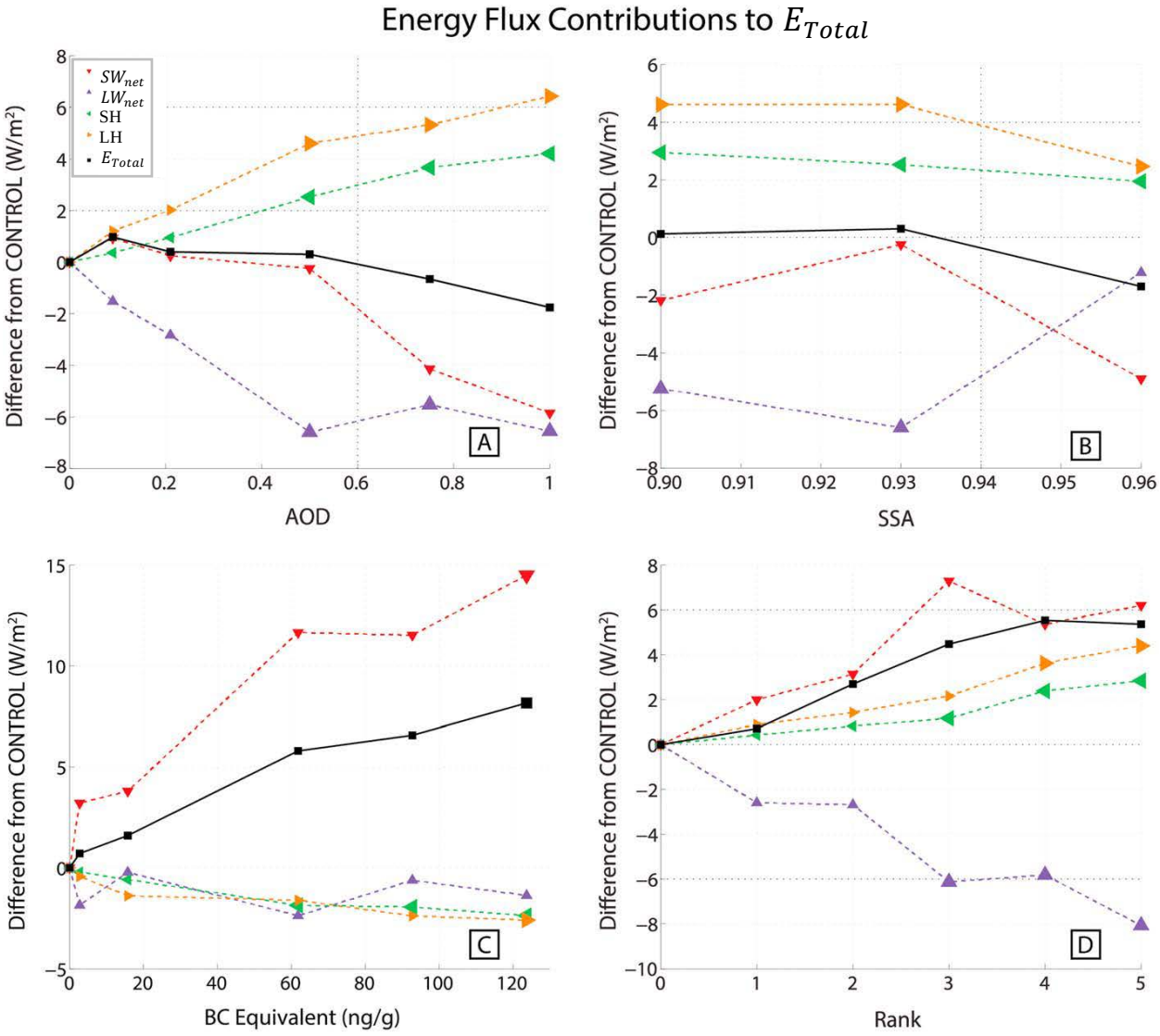

Fig. 2.6: Spatially averaged surface energy flux component changes for (a) AOD-ONLY, (b) VSSA, (c) IN-SNOW, and (d) BOTH scenarios. In each plot, SW_{net} is the net solar energy, LW_{net} is the net longwave energy, SH is sensible heat flux, and LH is latent heat flux.

Increasing the mass of LAA in the atmosphere generally leads to negative ΔSW_{net} through the process of surface dimming (Fig. 2.6A). As expected, spatially averaged ΔSW_{net} (red line) values are negative when AOD ≥ 0.5 in the AOD-ONLY simulations. Unexpectedly, in spite of the increasing LAA burden in the atmosphere, the AOD = 0.09 and AOD = 0.21 cases (Fig. 2.6) exhibit positive ΔSW_{net}. This occurs in the model because these aerosols lead to so-

called cloud burn-off while simultaneously allowing most of the insolation to transmit through the sparsely concentrated aerosol layer (Ban-Weiss et al., 2011; Ramanathan and Carmichael, 2008). We can verify cloud burn-off by calculating the change in cloud radiative forcing (ΔCRE) between each AOD-ONLY case and CONTROL:

$$\Delta CRE = \Delta SW_{net,clear-sky} - \Delta SW_{net} \quad (2.3),$$

where $\Delta SW_{net,clear-sky}$ is clear-sky solar flux. Negative ΔCRE indicates higher cloud radiative effect in CONTROL. High latitude clouds are difficult to model because cloud phase, optical thickness, and altitude result from the combination of large-scale circulation, boundary layer, and microphysical processes, among others (Curry et al., 1996; Kay & Gettelman, 2009). de Boer et al. (2012) and Kay et al. (2012) determined that cloud fraction is underestimated in the Arctic at all altitudes in CAM4. de Boer et al. (2012) also determined that liquid water path was overestimated and ice water path was underestimated by CAM4 in the high latitudes. We hypothesize that these cloud biases could impact our assessment of cloud changes and surface energy balance over Greenland. Based on de Boer et al. (2012) cloud composition findings in CAM4, we can assume that liquid clouds are over-represented in our simulations. Liquid clouds are more reflective than ice clouds, so CONTROL clouds might have a high-albedo bias. We speculate that burn-off of these liquid clouds could lead to overestimated ΔSW_{net} and net surface energy changes. Bearing these potential cloud biases in mind, we see low-level cloud burn-off for the AOD = 0.09 and AOD = 0.21 runs relative to CONTROL in Fig. 2.7 and in ΔCRE calculations (i.e., $\Delta CRE_{AOD=0.09} = -1.6\ W/m^2$ and $\Delta CRE_{AOD=0.21} = -3.6\ W/m^2$). This is further supported by the ΔLW_{net} results we discuss later in this section. We also observe lower surface albedo and upwelling solar energy in these cases (not shown), suggesting that decreasing GrIS snow albedo leads to enhanced absorption of sunlight at the surface.

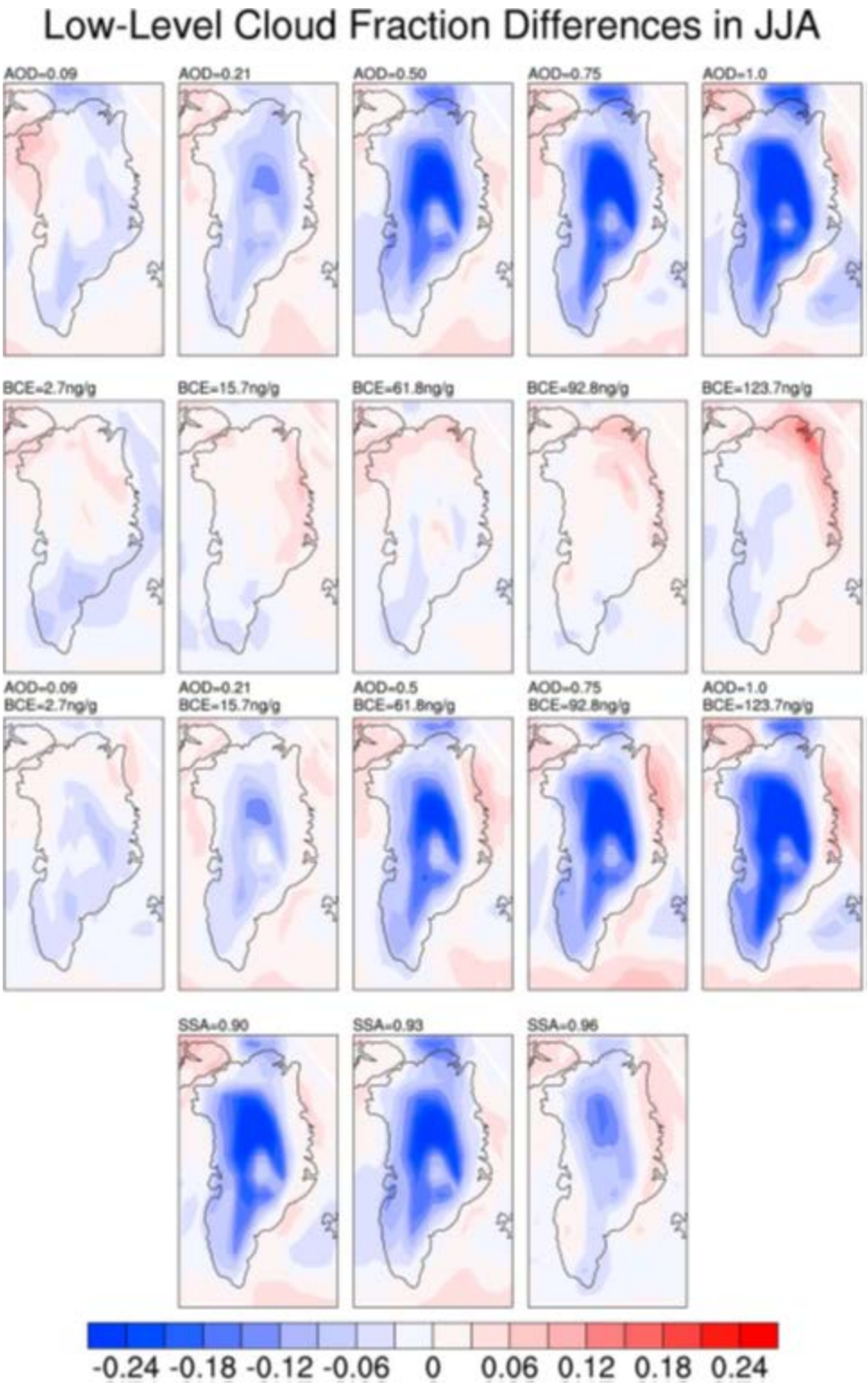

Fig. 2.7: Low cloud fraction changes for all cases relative to CONTROL.

We speculate that these changes result from snow aging processes induced by elevated $SW^{\downarrow}$, whereby snow grains become larger and result in lower near-infrared surface albedo (e.g., Flanner and Zender, 2006).

Like the AOD-ONLY cases with AOD ≥ 0.50, we determine that ΔSW_{net} is negative for all of the VSSA cases (Fig. 2.6B). Given that AOD = 0.50 for all of the VSSA runs, we know that surface dimming causes the reduction of sunlight at the surface. However, the mechanism diverting energy away from the GrIS depends on aerosol SSA. We find that $\Delta SW^{\uparrow}$ (Table 2.2) is more positive (i.e., there is less upwelling energy in the variable case) and $\Delta SW^{\downarrow}$ is more negative (i.e., there is less downwelling energy) for the SSA = 0.90 case due to enhanced LAA absorption. The values of $\Delta SW^{\uparrow}$ and $\Delta SW^{\downarrow}$ are roughly the same magnitude for SSA = 0.90, so its resulting ΔSW_{net} is less negative than ΔSW_{net} for SSA = 0.96.

In contrast to the atmospheric aerosol cases, the effects of deposited LAA on ΔSW_{net} are more straightforward (Fig. 2.6C). As we see from the IN-SNOW ΔQMELT and ΔT results, ΔSW_{net} becomes more positive with enhanced BC and dust mixing ratios due to the "in-snow" direct aerosol effect. Similarly, despite simultaneous atmospheric LAA presence, ΔSW_{net}also increases with enhanced aerosol burdens in the BOTH experiment. This further demonstrates that the presence of deposited BC and dust is generally more influential on the amount of solar energy absorbed at the surface than the presence of suspended LAA.

However, when we compare ΔSW_{net} between the IN-SNOW and BOTH experiments, we see that the largest ΔSW_{net} value in the BOTH runs (Fig. 6D) is not statistically significant and is roughly half the magnitude of the largest ΔSW_{net} for IN-SNOW. This results from the competing effects of surface dimming and surface darkening present in the BOTH experiment. We determine that IN-SNOW ΔSW_{net} is highest with the largest BC and dust mixing ratios, but

because of dimming, the BOTH case with the highest ΔSW_{net} is AOD = 0.50; BCE = 61.8 ng/g. These results suggest that the net impact of LAA is lower when both atmospheric and deposited aerosols are acting. The effects of deposited (atmospheric) LAA at high latitudes are often modeled independently; we assert that neglecting atmospheric (deposited) LAA in model simulations may lead to non-negligible biases in net surface energy flux.

For all of the experiments, we determine that average ΔLW_{net} (purple line) negatively contributes to ΔE_{Total}. The upwelling longwave term, $LW^{\uparrow}$, responds to surface temperature changes via the Stefan-Boltzmann relationship. However, the downwelling longwave energy flux change patterns ($LW^{\downarrow}$) depend on aerosol location. In all but the AOD = 0.09 case, we find negative $\Delta LW^{\downarrow}$. Although the LAA lead to localized warming in the atmosphere that could cause positive $\Delta LW^{\downarrow}$, the low-level (Figure 7) and midlevel cloud burn-off that result from the LAA reduce cloud-based $LW^{\downarrow}$. The negative $\Delta LW^{\downarrow}$ values that we calculate in the AOD-ONLY and VSSA experiments suggest that the effect of cloud removal slightly outweighs that of tropospheric warming.

When we examine the deposited aerosol cases (i.e., IN-SNOW and BOTH), we find that the magnitude of ΔLW_{net} largely depends on the presence of atmospheric LAA. As we observe in the IN-SNOW cases, ΔLW_{net} is negative and remains mostly constant. Similar to the AOD-ONLY and VSSA experiments, BOTH ΔLW_{net} becomes more negative as the atmospheric aerosol burden increases. The highest BC and dust mixing ratio cases in IN-SNOW and BOTH show the BOTH case having a ΔLW_{net} magnitude that is at least three times larger than the IN-SNOW equivalent. When we compare cloud burn-off between all experiments, we find the smallest low-level cloud fraction change in the IN-SNOW cases. Therefore, cloud-based $LW^{\downarrow}$ in the IN-SNOW runs does not decrease to the extent that we observe in the other cases (Fig. 2.7).

Furthermore, unlike the atmospheric aerosol experiments, IN-SNOW ΔLW_{net} only depends on BC and dust mixing ratios; the GrIS surface does not receive any statistically significant change in $LW^{\downarrow}$ from the atmosphere relative to CONTROL.

Unlike the shortwave and longwave energy fluxes, increasing AOD and decreasing SSA lead to positive ΔSH (orange line) and ΔLH (green line; i.e., more downward directed flux or less upward directed flux). Both of these changes occur as a result of the direct aerosol effect. With increasing atmospheric LAA burdens or decreasing SSA, more insolation is absorbed in the aerosol layer. As we have seen with the ΔT analysis, this leads to increasing ΔT within the aerosol layer. By the Clausius-Clapeyron relationship, local saturation specific humidity also increases. These air temperature and saturation specific humidity enhancements lead to positive sensible and latent heat flux changes. Research by Wang (2004) also supports this positive change in heat energy flux as a result of LAA presence. Wang (2004) used a suite of global climate models to determine how BC affects radiative energy in the climate system. In response to negative radiative forcing at the surface caused by BC in the atmosphere, Wang (2004) suggested that the positive sensible and latent heat fluxes served as a compensating mechanism to offset the negative energy balance at the surface. This result is apparent in our AOD-ONLY and VSSA model simulations. In the AOD-ONLY and VSSA scenarios, ΔSH and ΔLH are the only positive energy components of ΔE_{Total}. However, as we can observe from Figs. 2.6A and 2.6B, the negative ΔSW_{net} and ΔLW_{net} are collectively comparable to ΔSH and ΔLH. This is why we do not calculate significant ΔQMELT or ΔE_{Total} in any of these cases.

Deposited aerosols in IN-SNOW lead to changes in the magnitude and sign of ΔSH and ΔLH relative to the BOTH runs. To compensate for energy being added to the surface via positive ΔSW_{net}, the IN-SNOW simulations exhibit negative ΔSHand ΔLH. Air temperature and

specific humidity increase at the surface (e.g., Fig. 1) relative to CONTROL and create changes in temperature and specific humidity gradients that lead to negative heat flux changes. As we can see from Fig. 2.6, the values of ΔSH and ΔLH for IN-SNOW decrease slightly with increasing deposited LAA mixing ratios and are comparable to the magnitude of ΔLW_{net}. Overall, the only positive energy contribution to ΔE_{Total} for IN-SNOW is ΔSW_{net}. However, ΔSW_{net} for each BC and dust mixing ratio case is much larger than the sum of ΔLW_{net}, ΔSH, and ΔLH, which is why ΔE_{Total} and ΔQMELT are positive for all IN-SNOW cases.

In contrast to the IN-SNOW experiment, the BOTH simulations all depict positive ΔSH and ΔLH. This indicates that for surface sensible and latent heat flux changes, atmospheric aerosols are more influential on the direction of energy flow than their in-snow counterparts. We also note that of all of the experiments involving atmospheric aerosols, ΔSH and ΔLH magnitudes are the smallest in the BOTH scenario because of the offsetting impacts of in-snow aerosols. However, despite positive ΔSH and ΔLH for all BOTH cases, we can see from Fig. 2.6 that solar energy changes still contribute more to ΔE_{Total}. Unlike all of the other simulations, the only surface energy component that leads to energy depletion in ΔE_{Total} in BOTH is ΔLW_{net}. However, the combination of ΔSW_{net}, ΔSH, and ΔLH all contribute more energy to the surface than longwave energy emission removes, so ΔQMELT and ΔE_{Total} both increase.

2.4 Conclusion

In this study, we use CESM to better understand the relative impact of atmospheric and deposited LAA on the climate of Greenland. To achieve this goal, we compare idealized simulations with varying LAA mixing ratios to a local-to-Greenland no-aerosol control run (i.e., CONTROL) by using a series of independent two-sample t-tests. By comparing variable aerosol

simulations to CONTROL, we are able to determine the effects of LAA on the climate of Greenland, and we are also able to determine how increasing aerosol burdens can impact these results.

We determine that air temperature changes (ΔT) throughout the lower portion of the atmosphere and at the surface are caused by local LAA. In the AOD-ONLY runs, air temperature within the aerosol layer and at the surface increases monotonically with respect to CONTROL. However, ΔTs is smaller than ΔT within the aerosol layer for all AOD-ONLY cases because of surface dimming caused by the suspended LAA. We observe the same ΔT patterns seen in the AOD-ONLY cases at both the surface and in the lower troposphere for the VSSA runs. We further determine that decreasing SSA leads to a monotonic increase in ΔT as a result of the increasing absorbing capabilities of the LAA. Deposited aerosols also affect the ΔT trends we observe, but the patterns differ from those we see with atmospheric aerosols. With the exception of the BCE = 92.8 ng/g case in the IN-SNOW experiment, ΔT_s increases monotonically because of the "in-snow" direct aerosol effect. We attribute the non-monotonic ΔT_s increase for the BCE=92.8 ng/g run to model noise and variability. We also demonstrate that ΔT decreases in magnitude with altitude for all IN-SNOW runs. When we simulate the presence of both atmospheric and deposited LAA, the resulting air temperature change trends are similar to those in AOD-ONLY, but the ΔT values are positively skewed in the lower troposphere and at the surface for higher LAA cases.

Along with the changes in tropospheric air temperature, we determine that snowmelt and surface energy flux changes associated with LAA largely depend on aerosol location. Increasing atmospheric LAA burden leads to surface dimming and enhanced air temperatures just above the surface. These offsetting effects of atmospheric LAA lead to non-statistically significant changes

in melt and net surface energy flux across the entire GrIS for the AOD-ONLY and VSSA experiments. For the AOD-ONLY cases, we show that both snowmelt and net surface energy flux initially increase with enhanced LAA burden before decreasing as a result of surface dimming. We find further evidence of surface dimming by the negative ΔSW_{net} component of ΔE_{Total} when AOD $\geq$ 0.50. In contrast, we calculate positive ΔFSNS in the AOD $\leq$ 0.21 cases because of cloud burn-off. Although the sign of ΔSW_{net} for the AOD-ONLY experiment depends on the AOD value, we observe that both ΔSW_{net} and snowmelt changes (ΔQMELT) transform from positive to negative at the same AOD value. This indicates that ΔSW_{net} is very influential for subsequent snowmelt changes. The change in net longwave energy flux negatively impacts the surface energy balance for all atmospheric aerosol cases. In contrast, ΔSH and ΔLH positively contribute to ΔE_{Total} as a result of localized warming in the air above the GrIS. We observe this pattern in all experiments involving the presence of atmospheric aerosols, regardless of whether in-snow impurities are also present. In the VSSA experiment, ΔSW_{net} is negative for all cases because of absorption or scattering by the moderately high aerosol load imposed in the lower troposphere. As a result of decreased surface albedo from in-snow LAA overwhelming dimming caused by atmospheric LAA, though, the BOTH simulations all maintain positive ΔSW_{net}.

When we impose BC and dust in GrIS snow, we find that snowmelt and net surface energy increase with increasing LAA mixing ratios because of reduced surface albedo. In the IN-SNOW and BOTH experiments, snowmelt increases with higher aerosol burdens. Unlike the BOTH scenario, the IN-SNOW positive energy balance of the GrIS is due to the dominating positive ΔSW_{net} relative to negative ΔLW_{net}, ΔSH, and ΔLH. The relative magnitudes of ΔQMELT for the IN-SNOW runs are comparable to the corresponding SW_{net} deviations, while

changes in snowmelt for the BOTH experiment depend on ΔSW_{net}, and to a lesser extent, ΔSH and ΔLH. Overall, we find that in-snow aerosols affect snowmelt more than their atmospheric counterparts. However, the snowmelt and net surface energy changes we calculate for these experiments show that LAA in the atmosphere reduce the impact of aerosols on the ground by a factor of 2. This finding highlights the offsetting effects of atmospheric aerosols and emphasizes the importance of including atmospheric LAA when simulating the climate effects of deposited LAA, especially on ice- and snow-covered terrain.

Although this research demonstrates the relative effects of atmospheric and deposited LAA on air temperature, snowmelt, and surface energy fluxes for the GrIS, there are several aspects of Greenland's climate and the effects of biomass burning that we do not address. Most importantly, we investigate the effects of LAA in a highly idealized modeling environment. We maintain constant and spatially uniform aerosol burdens in the snow and lower atmosphere for the duration of each simulation rather than explicitly representing aerosol advection from remote locations into the Greenland region (e.g., Thomas et al., 2017). Atmospheric circulation mechanisms lead to spatially heterogeneous aerosol distributions on the surface and in the atmosphere. For example, atmospheric LAA from biomass burning generally decrease from west to east over the GrIS because of plume dilution and LAA depositional processes. Although BC and OC can serve as CCN after transport and aging processes (i.e., Bond et al., 2013), the bulk aerosol setup we use neglects this process. BC and OC CCN affect cloud lifespan, cloud albedo, and incident radiation at the surface. Wang et al. (2018) confirm that aerosol microphysical effects make up a large portion of the total aerosol forcing in the Arctic. Inclusion of these effects in our experimental setup would have impacted our findings. Along with simulating spatially homogeneous aerosol burdens, the larger atmospheric and in-snow aerosol mixing

ratios we impose (i.e., rank 4 and rank 5 on Table 1) are extreme burdens that have not been observed over Greenland (McConnell et al., 2007; Polashenski et al., 2015). LAA mixing ratios similar to the BCE = 61.8 ng/g case have only been measured in GrIS snow once during the last 215 years, and monthly concentrations of BC in GrIS snow that exceed 5 ng/g have occurred only two or three times in each decade since 1950 (McConnell et al., 2007). Because biomass burning and its transport are spatially and temporally episodic, simulating the constant presence of biomass burning aerosols over and on the surface of Greenland leads to more radiative forcing than would be realistic for the region (Clark et al., 2015). However, regardless of emission source, multiple studies have found that BC and other aerosols are most prevalent over the GrIS during the summer months (Jiao et al., 2014; Sand et al., 2013). Biomass burning and anthropogenic aerosols transported to the GrIS from other areas of the northern hemisphere are suspended at various levels in the atmosphere (e.g., Jiao & Flanner, 2016), which we also do not take into account for our atmospheric aerosol experiments.

Although the purpose of this study is to explore Greenland's climate response to idealized, clearly defined distributions of LAA, it would be noteworthy to take these factors into account to depict a more realistic representation of the response of Greenland's climate. Furthermore, in the case of our experimental setup, it would also be useful to examine the effects of LAA SSA by expanding SSA deviations to AOD values apart from AOD = 0.50. Overall, the results from these idealized and well-defined experiments indicate that BC and dust can affect snowmelt and the climate of Greenland when suspended in the atmosphere or, especially, deposited on the surface.

Chapter 3. Impacts of Greenland Block Location on Clouds and Surface Energy Fluxes over the Greenland Ice Sheet

(Ward et al., 2020; submitted)

3.1 Introduction

Many atmospheric processes affect Greenland Ice Sheet (GrIS) surface energy fluxes and subsequent surface mass balance changes. Clouds impact the GrIS surface by reflecting insolation away from the surface (i.e., cooling) while also trapping and reemitting longwave energy (i.e., warming). Over snow-covered surfaces like the GrIS, the magnitude of this cloud radiative forcing is affected by cloud properties like ice-to-liquid cloud content ratios, cloud height, and cloud water path (i.e., Shupe and Intrieri, 2004). Liquid-bearing clouds, which are most common over Greenland during the summer months (Shupe et al., 2013; Miller et al., 2015; Van Tricht et al., 2016; Lenaerts et al., 2017), enhance net radiative surface energy flux by largely increasing longwave energy fluxes and only marginally dimming surface insolation (Shupe and Intrieri, 2004; McIllhatan et al., 2017). Optically-thin, low-lying liquid-bearing clouds are optimal for increasing surface radiative energy flux (Bennartz et al., 2013; Van Tricht et al., 2016). In recent years and in future climate projections, liquid-bearing clouds contribute to melt over much of the GrIS (Bennartz et al., 2013; Van Tricht et al., 2016; Hofer et al., 2019).

One factor that increases Greenland cloud fraction is enhanced atmospheric water vapor from local- and remotely sourced moisture transport (Johansson et al., 2017). Although summertime moisture amounts and source regions vary regionally over Greenland (e.g., Nusbaumer et al., 2019), a large portion of atmospheric water vapor originates over the North Atlantic. This warmer, moister air moves over the GrIS surface and can influence not only clouds but also skin surface temperatures and snowmelt rate (Pfahl et al., 2015; Mattingly et al., 2018). Over the last 20 years, available water vapor over Greenland has increased with warming air temperatures (Mattingly et al., 2016) and will likely affect Greenland's future climate through increased cloud cover.

Atmospheric dynamics affect GrIS surface processes by influencing cloud formation, moisture transport, and temperature advection. These processes are complicated by airflow changes that result because of the elevated GrIS surface. Greenland "blocks" (i.e., quasi-stationary anticyclones lasting for days-to-weeks) increase GrIS melt through warm air advection and cloud suppression (Box et al., 2012; Fettweis et al., 2013; Hanna et al., 2014; McLeod and Mote, 2016; Hofer et al., 2017; Mattingly et al., 2018). The resulting cloud reduction and warm air advection from blocking enhance insolation and sensible heat fluxes, respectively, which can enhance surface melt (Hanna et al., 2014; Rajewicz and Marshall, 2014; Lim et al., 2016; Mioduszewski et al., 2016; Hofer et al., 2017). In addition, Greenland blocking is likely related to regional atmospheric moisture transport processes (i.e., Mattingly et al., 2018; Nusbaumer et al., 2019), and thus also cloud patterns and phase. Over Summit, liquid-bearing clouds have larger water paths and are longer-lived during block-like (i.e., ridging) flow regimes (Edwards-Opperman et al., 2018). Summertime Greenland blocking activity has significantly increased over the past twenty years (i.e., Fettweis et al., 2013; Rajewicz and Marshall, 2014; Belleflamme

et al., 2015; Hanna et al., 2016; McLeod and Mote, 2016) and is another potential contributor to GrIS snowmelt enhancement (Rignot et al., 2008; Fettweis et al., 2011; Shepherd et al., 2012; Tedesco and Fettweis, 2019).

The surface mass balance and energy flux effects resulting from different wind patterns and cloud locations vary spatially over the GrIS. Compared to eastern Greenland, westerly/southerly winds produce more cloud cover over western Greenland in the summer months that significantly reduces insolation while enhancing longwave fluxes and surface melt (Cawkwell and Bamber, 2002; Cullather and Nowicki, 2018). Moisture transport over western Greenland also has a larger impact on local GrIS snowmelt because the air is warmer and moister than over eastern Greenland (Mattingly et al., 2018). The effects of Greenland blocking on cloud cover (e.g., Lim et al., 2016; Hofer et al., 2017), temperature advection, and subsequent snowmelt and surface energy flux processes (e.g., Fettweis et al., 2013; Belleflamme et al., 2015; Tedesco et al., 2016b) also exhibit spatial variability and have been explored in previous studies. However, these studies investigate average blocking conditions that do not account for the quasi-stationary nature of Greenland blocks (e.g., Chen and Luo, 2017). Different block locations could produce variations in cloud, moisture transport, and surface energy flux patterns by changing air source regions and how block airflow interacts with the GrIS surface, which could directly impact GrIS surface mass balance processes.

In this study, we use a combination of reanalysis and satellite cloud data to document and differentiate the effects of summertime (i.e., June through August) Greenland block location on cloud formation, moisture transport, and surface energy flux processes over the GrIS. First, we describe the datasets, blocking detection algorithm, and statistical methods we use for this study. Next, we explore the impacts of block location on cloudiness in terms of moisture transport,

temperature, and airflow patterns. We then explore the implications of cloud changes on Greenland-wide cloud radiative forcing and total surface energy fluxes.

3.2 Methods

We use Modern-Era Retrospective Analysis for Research and Applications, version 2 (MERRA-2) reanalysis data to find blocks and analyze their associated meteorological and surface energy flux patterns over the GrIS (Gelaro et al., 2017). Although output variability exists between different reanalysis datasets because of varying observational sources and data assimilation schemes (e.g., Graham et al., 2019), MERRA-2 compares favorably to state-of-the-art ERA5 (CS3, 2017) output (Figs. A.1-A.2), which agrees well with observations over the Arctic (Delhasse et al., 2020). Because we are interested in blocking-induced cloud and surface energy flux anomalies that could materially impact summer surface melt, we analyze blocks in June, July, and August (JJA) from 2002 through 2018. We include days in late May and early September if they are part of early June and late August blocking events, respectively.

To detect blocks in the MERRA-2 dataset, we use a modified version of the Dunn-Sigouin et al. (2013) algorithm (hereafter referred to as D-S) (see Table 3.1). The multi-step approach of the D-S algorithm requires the satisfaction of multiple conditions to classify events as blocks (Dunn-Sigouin et al., 2013). In brief, the D-S method tracks contiguous groupings of 500mb geopotential height anomalies (Z'_{500}) meeting minimum pre-established amplitude threshold (A) and area requirements (S) over time. For each latitude/longitude grid, we calculate Z'_{500} between May 16 and September 15 with the following formula:

$$Z'_{500}(n) = Z_{500}(n) - Z_{clim}(n) \quad (3.1),$$

where $Z_{clim}(n)$ is the climatological average 500mb geopotential height. Z_{clim} is defined using a Gaussian-weighted, 31-day moving window centered on day *n* for all 17 years (2002-2018) of 500mb geopotential height data. Gaussian weighting places more emphasis on days close to *n*, incorporating seasonal variability in Z_{500}. In the D-S algorithm, a block is recorded if 1) the Z'_{500} areas between consecutive days overlap (O) by a certain percentage, and 2) these anomalies exist for a predefined number of days (D). Although the original D-S detection algorithm further tests for a Z_{500} gradient reversal equatorward of the block, we do not maintain this requirement because persistent high pressure ridging is a prominent variety of blocking in the Greenland region (Fettweis et al., 2013; Hanna et al., 2014; Tedesco et al., 2016b). The original and modified D-S thresholds are listed in Table 1. More details about the D-S algorithm can be found in Dunn-Sigouin et al. (2013).

Table 3.1: Dunn-Sigouin (D-S) algorithm original and modified parameters

Threshold	**Units**	**Original D-S**	**Modified D-S**
Duration (D)	Days	5	4
Amplitude (A)	Unitless	1.5	1.2
Spatial Scale (S)	km^2	2.5×10^6	1.0×10^6
Overlap (O)	Percentage	50	50

The block location for each block day detected in the modified D-S setup is determined using the equal-area block quadrants defined in Fig. 3.1A. For each block day, we first find the local maximum Z'_{500} latitude/longitude coordinate that is closest to Greenland; if there are multiple Z'_{500} local maxima, we choose the Z'_{500} data point with the largest magnitude. We then find its corresponding Z_{500} maximum latitude/longitude grid point and bin it in one of the four Greenland block quadrants (Fig. 3.1A). Because midlatitude ridging can result in Z_{500} center points south of our Greenland domain, we allow Z_{500} to lie marginally outside of the defined block quadrants.

Fig. 3.1: A) Equal-area Greenland block quadrants. The quadrants are Northwest (NW), Northeast (NE), Southwest (SW), and Southeast (SE). B) Present-day topography of the GrIS derived from MERRA-2 surface geopotential data.

We use Moderate Resolution Imaging Spectroradiometer (MODIS) Terra Collection 6, Level 2 cloud data (product code MOD06), which extends from 2002 to present (Platnick et al., 2017), to analyze cloud conditions during Greenland blocking. We choose MOD06 data because of its high spatial and temporal coverage, as well as its incorporation of processing algorithm improvements for high latitude opaque cloud detection and characterization over the reflective GrIS snow (Ackerman et al., 1998; Liu et al., 2010; Platnick et al., 2017). The cloud water path and cloud optical thickness fields we use are produced by the combination of 1.6μm and 2.1μm bands for better surface-cloud differentiation (Platnick et al., 2001). Although MOD06 data are accompanied by detection uncertainties, we do not include these here.

To better compare the MERRA-2 data to the corresponding daily cloud conditions, we spatially aggregate 1x1km and 5x5km along-swath gridded granule MOD06 data onto the 0.5° ×

0.625° MERRA-2 grid and average all resulting cloud data for each day. This regridded, daily-averaged MOD06 data covers $60 - 85°N$ latitude and $93.125°W - 13.125°E$ longitude to accommodate clouds corresponding to blocking in each block quadrant. We first aggregate 1x1km fields onto the 5x5km grid for each MODIS granule. Because cloud water path data is only collected during the day, we exclude "nighttime" pixels with solar zenith angle values exceeding 81.36° degrees for all other cloud variables (Platnick et al., 2017). We then aggregate 5x5km granule data onto the larger MERRA-2 grid by averaging the closest 5x5km data points onto each MERRA-2 grid point. Apart from cloud fraction and cloud phase, all MOD06 variables are averaged onto the MERRA-2 grid with cloud fraction weighting for each MODIS granule. Finally, we average (using cloud fraction weighting) each MERRA-2 gridded MOD06 data field over time to create daily average cloud fields.

Because cloud formation depends on the presence of atmospheric moisture, we evaluate moisture transport ($kg\ m^{-1}s^{-1}$) during blocking in each block quadrant, during all blocks combined, and during non-block days (i.e., JJA 2002-2018 days that do not exhibit blocking) to gain a first-order understanding of the effects of blocking on clouds and surface processes. Similar to Woods et al. (2013), we calculate daily gridded total column moisture transport as:

$$F = \frac{1}{g}\int_{400}^{p_s} Q(p) * W(p)dp \quad (3.2).$$

In (2), F is the resulting total column moisture flux, g is the acceleration of gravity ($9.8\,m/s^2$), $Q(p)$ is specific humidity at pressure level p, $W(p)$ is the wind velocity at p, and p ranges from pressure at the surface (p_s) to 400mb (Woods et al., 2013). Because of GrIS surface elevation variability and daily changes in atmospheric pressure, p_s is spatially and temporally variable in our Greenland domain.

GrIS surface energy balance is important to disentangle the effects of block location and subsequent cloud processes on snowmelt. We calculate total surface energy flux as the sum of net shortwave energy, net longwave energy, sensible heat flux, and latent heat flux at each point in the Greenland domain (e.g., van den Broeke et al., 2017; Lenaerts et al., 2019). We note that turbulent heat fluxes are positive when directed into the surface. We do not include conductive heat flux in our surface energy balance calculation because its magnitude is negligible in ice covered regions (Yang et al., 2011). In addition, to examine the impacts of clouds in each blocking case on net surface radiative fluxes, we calculate total cloud radiative forcing using all-sky (all) and clear-sky (clr) quantities:

$$CRF_{TOTAL} = CRF_{SW} + CRF_{LW} = \left(SW_{net,all} - SW_{net,clr}\right) + \left(LW_{net,all} - LW_{net,clr}\right) \quad (3.3).$$

Because high-latitude insolation varies strongly with time of year, our subsets of regional block and non-block days are subject to different mean insolation. To account for this, we use MERRA-2 downwelling top-of-atmosphere shortwave energy data to scale shortwave flux-related fields so they represent consistent "summer-mean" values. We calculate GrIS-wide top-of-atmosphere incoming solar radiation averages for summer (i.e., all days in JJA), "Control" (i.e., JJA non-block days), and block days in each blocking scenario. We divide this summer average by the corresponding "Control" and block day mean insolation to calculate shortwave scaling factors that are used to normalize our filtered surface and cloud shortwave fluxes. These scaling factors are listed in Table S2. Surface energy flux components are considered to be positive in the downward direction because they positively contribute to total surface energy.

We differentiate surface energy fluxes, meteorological conditions, and cloud properties between block days in each quadrant, "All Blocks", and non-block days ("Control") using two-sample t-testing for each coordinate and spatial averaging over the GrIS. In the case of spatial

averages, we define GrIS pixels as those having at least 50% land ice coverage, as defined with the MERRA-2 land ice surface fractions.

3.3 Results and Discussion

3.3.1 Blocking Statistics

Here, we briefly describe the frequency characteristics of block days for "All Blocks" and individual block quadrants. We find a total of 205 summer block days associated with 30 blocking events. Four of these blocking events extend outside of JJA (see Table A1 in Appendix 1 for block day list). There are ~12.1 block days per summer, on average, with a standard deviation of ~10.5 days. This year-to-year variability in block day count results from varying synoptic- to planetary-scale dynamics. We find above-average summer block day counts in 2003, 2006-2008, 2012, and 2015- 2016 (Fig. 3.2), which aligns well with previously reported Greenland blocking frequencies (e.g., Fettweis et al., 2011; Fettweis et al., 2013; Hanna et al., 2016; Tedesco et al., 2016b).

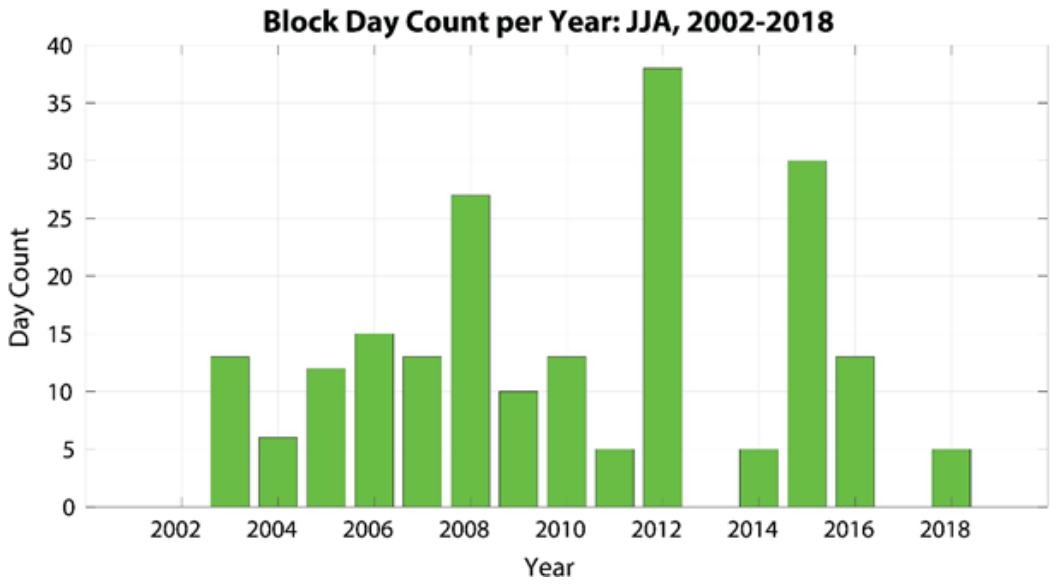

Fig. 3.2: Block day counts for each summer season (JJA) from 2002 to 2018.

Binning block days to our defined block quadrants (i.e., Fig. 3.1A) provides us with additional information about preferred blocking regions around Greenland. From Fig. 3.3A, and in agreement with previous studies (i.e., Häkkinen et al., 2014; McLeod and Mote, 2015; Cullather and Nowicki, 2018), the average "All Blocks" block center is located over south-central Greenland. We also see that average NW and NE blocks are smaller with higher geopotential heights than SW and SE blocks. Overall, we find that the southwest (SW) and southeast (SE) block quadrants contain more block days (69 and 80 days, respectively) than the northwest (NW) and northeast (NE) block quadrants (35 and 21 days, respectively). However, northern quadrant block days comprise 27% of Greenland blocking activity and are thus important to Greenland's climate.

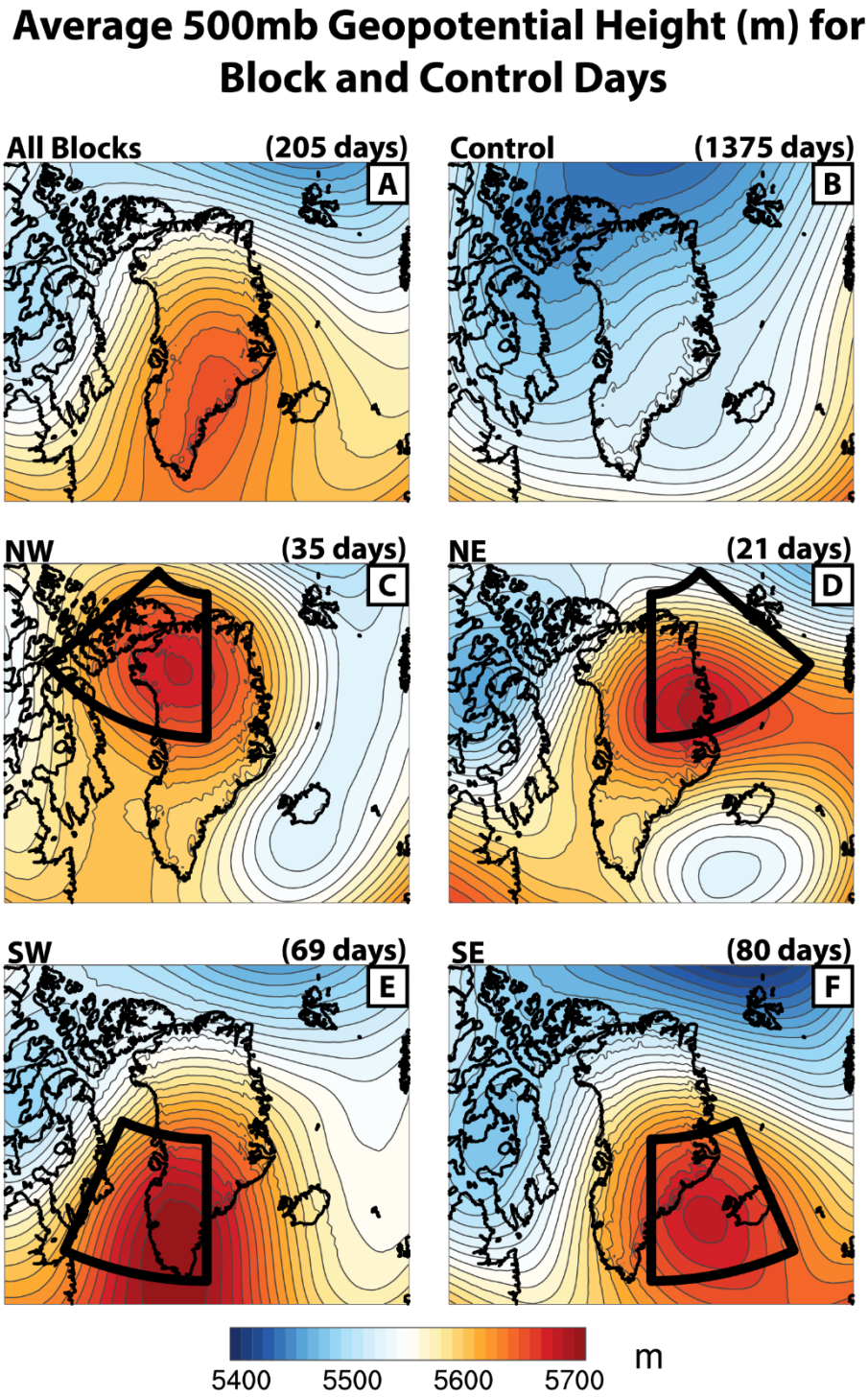

Fig. 3.3: Composite 500mb geopotential height plots for A) "All Blocks", B) "Control", C) NW, D) NE, E) SW, and F) SE block days. Day counts are listed above each panel. Black boxes in C-F represent the corresponding block quadrant boundaries.

3.3.2 Clouds and Block Location

In this section, we explore MOD06 cloud fraction (Fig. 3.4) and cloud water path (Fig. 3.6) changes over the Greenland Ice Sheet for “All Blocks” and individual block quadrants with respect to “Control”. We use moisture transport and wind fields (Fig. 3.5) to explain the resulting cloud anomaly patterns for each blocking case.

We can see in Fig. 3.4 that cloud fraction anomaly distributions are different between “All Blocks” and individual block quadrants. Regardless of block location, however, composite 500mb geopotential height block centers (Fig. 3.3) are collocated with negative cloud fraction anomalies because of high pressure subsidence (Box et al., 2012; Hanna et al., 2014; Rajewicz and Marshall, 2014; Lim et al., 2016; Mioduszewski et al., 2016; Hofer et al., 2017). In the case of “All Blocks”, cloud fraction anomalies are negative over most of the GrIS (Fig. 3.4C). The most negative of these cloud fraction changes is located over southern Greenland and coincides with the average “All Blocks” high pressure center (Fig. 3.3A). In agreement with previous studies (e.g., Hofer et al., 2017; Delhasse et al., 2018), limited positive cloud fraction anomalies in north-central Greenland result from onshore, westerly airflow (Fig. 3.5A) that cools adiabatically and condenses. Overall, Greenland-average cloud fraction decreases by 0.04 “All Blocks”.

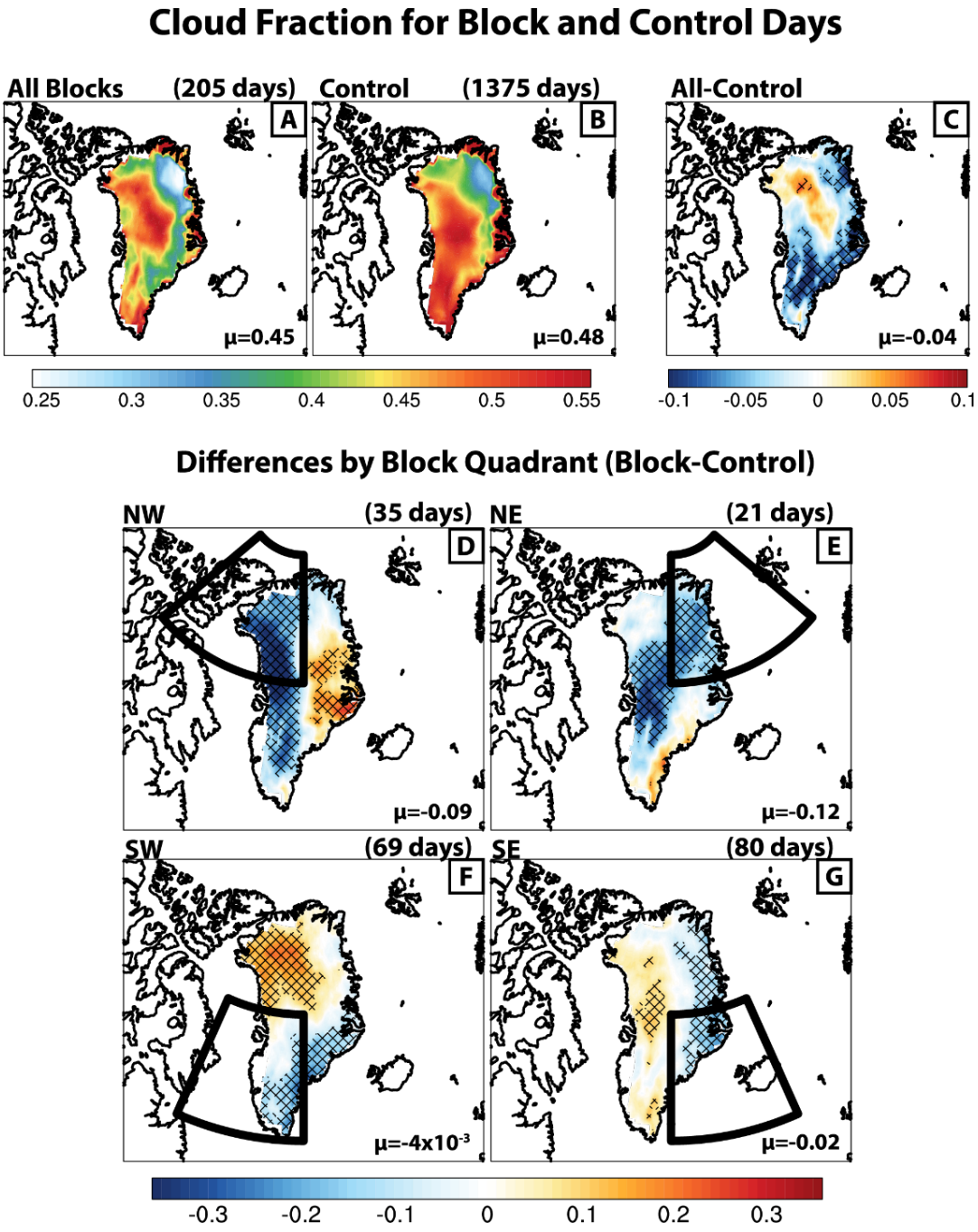

Fig. 3.4: MOD06 cloud fraction. Panels A and B show absolute cloud fraction for "All Blocks" and "Control", respectively, and their difference is in panel C. Quadrant-based cloud fraction changes with respect to "Control" are in panels D through G, with GrIS averages in the lower right-hand corner of each panel. The black boxes are the corresponding quadrant boundaries. Cross-hatching in panels C through G represents statistically significant differences (95% confidence level).

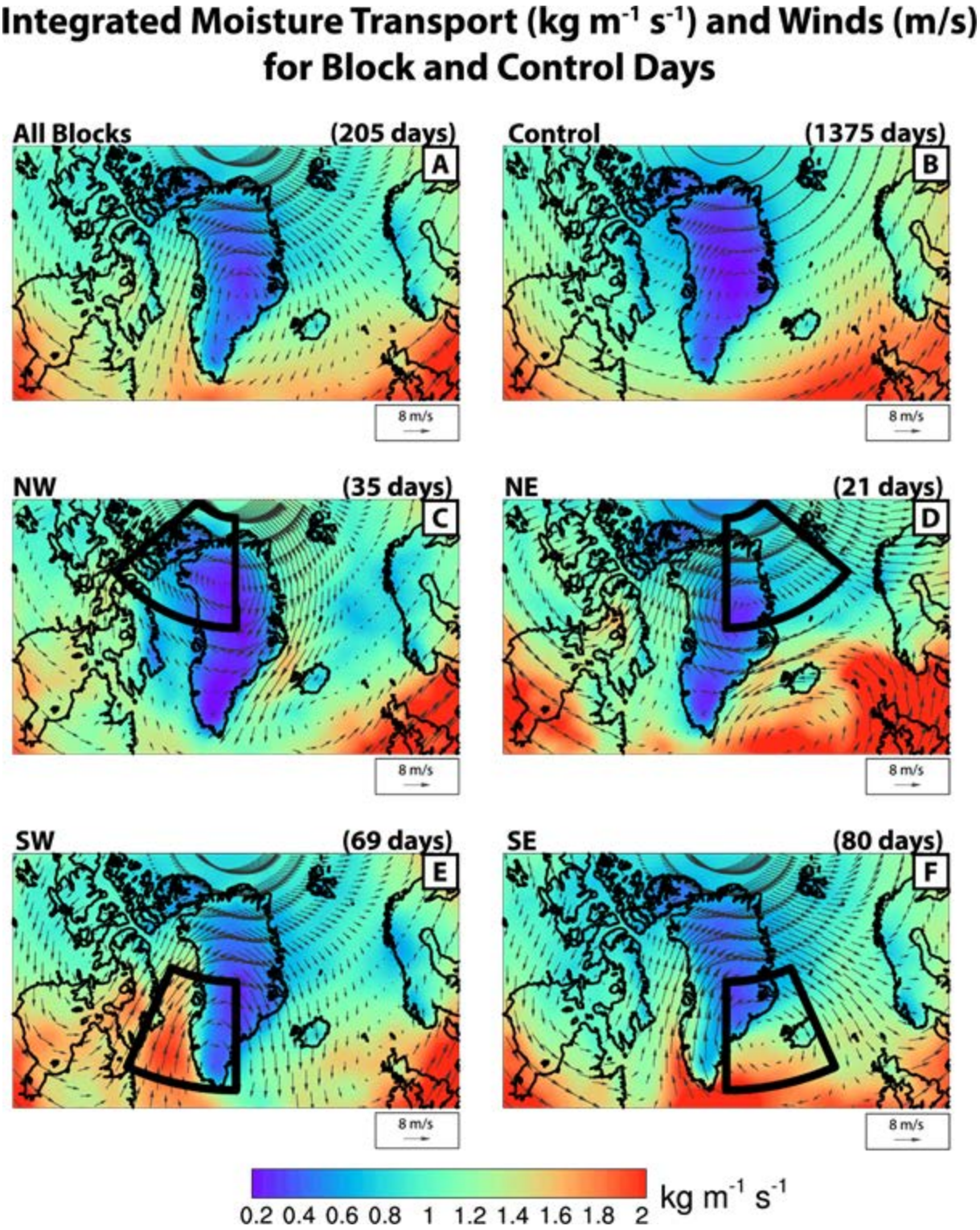

Fig. 3.5: Vertically integrated moisture transport (contours) and winds (arrows). The reference wind speed and arrow size are shown below each panel.

Outside of the block centers for each block location, we find that NW and NE block day cloud fraction change patterns are markedly different from those for SW and SE block days. In these cases, easterly winds flow (Fig. 3.5C-D) downslope from central Greenland and warm adiabatically to inhibit cloud formation. NW block days also produce significant cloud fraction enhancements over the eastern half of the GrIS (Fig. 3.4D) because of rising northerly airflow (Fig. 3.5C). Despite these small regions of increased cloudiness, Greenland-average cloud fraction is reduced by 0.09 and 0.12 during NW and NE block days, respectively (Fig. 3.4D-E). Cloud fraction anomaly spatial patterns reverse for SW and SE block days. Namely, SW and SE block days produce enhanced cloud fractions over portions of western Greenland and cloud fraction reductions over eastern Greenland. Cloud fraction changes for southern Greenland block days more closely represent "All Blocks" cloud fraction changes because they constitute a majority of all block days. Positive cloud fraction anomalies over northern Greenland are produced by westerly-based winds moving upslope over the GrIS margins (Fig. 3.5E-F) that adiabatically enhance cloud cover (i.e., Neff et al., 2014; McLeod and Mote, 2015; Mioduszewski et al., 2016; Mattingly et al., 2018). SE block days reduce cloud fractions along the eastern GrIS margins because westerly airflow adiabatically warms as it descends from the central GrIS towards the eastern shoreline. Similarly for SW block days, we calculate reduced cloud coverage over southeastern Greenland because of downslope airflow. Despite more prevalent cloud fraction enhancement over the GrIS during SW and SE block days, GrIS-average cloud fraction anomalies are still negative (-0.004 and -0.02, respectively).

Cloud water path changes are helpful for explaining cloud radiative forcing and surface energy flux anomalies produced by blocking. For "All Blocks", "Control", and individual block location cases, cloud water path spatial patterns (Fig. 3.6) are similar to their corresponding

cloud fraction patterns; areas of reduced cloud fraction align with areas of decreased cloud water path, and vice versa.

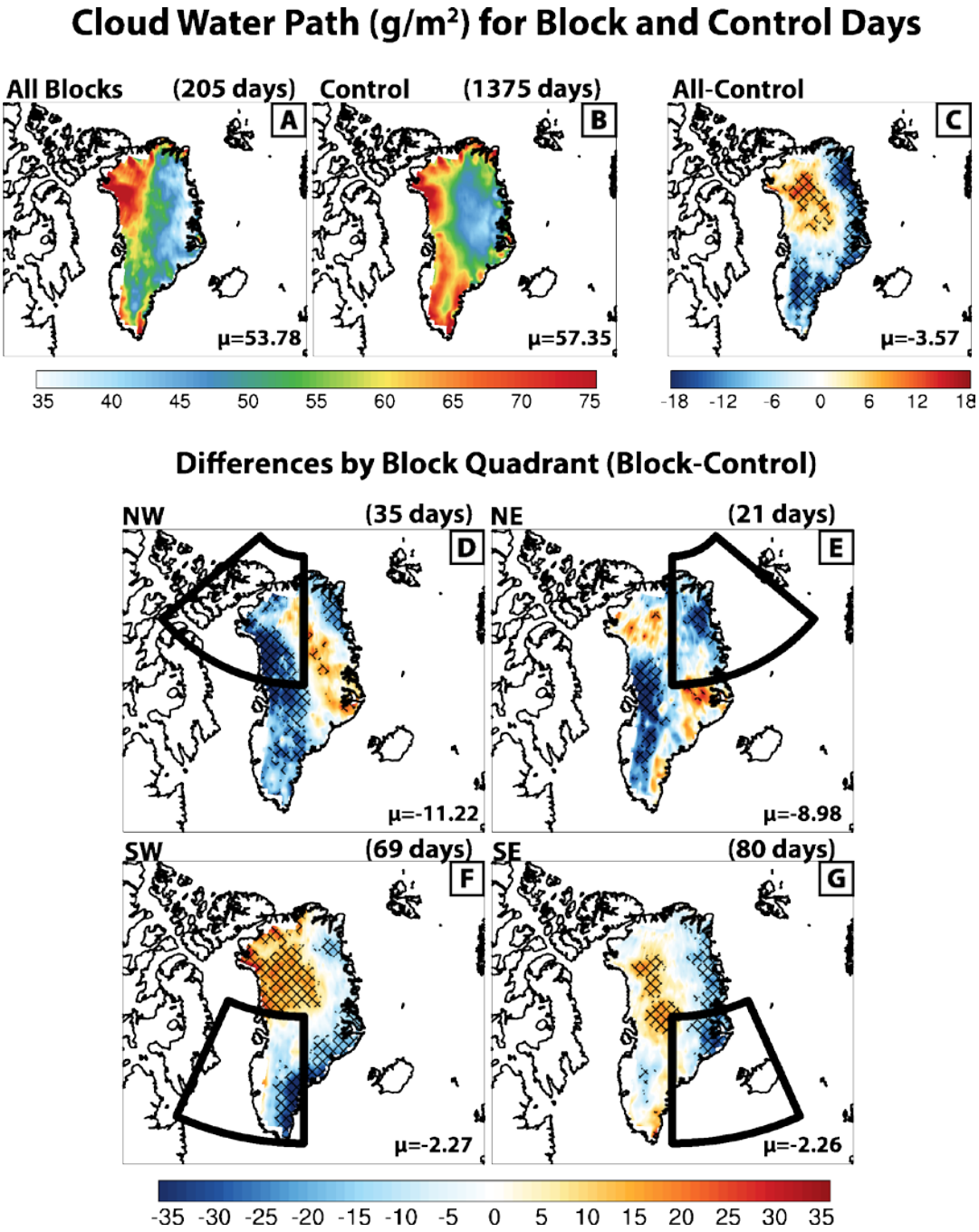

Fig. 3.6: Same as Fig. 3.4, but for cloud water path (g/m^2).

In addition to the interaction of anticyclonic airflow with Greenland's topography, available total column moisture is another contributing factor to cloud water path changes (Table 3.2).

Table 3.2: Total Column Water Vapor (Blocking values are anomalies)

Day Set	*Total Column Water Vapor (g/m^2)*
"Control"	55.30
"All Blocks"	8.80
NW	3.70
NE	7.10
SW	11.00
SE	9.50

Despite greater total column water vapor over the GrIS for each blocking case compared to "Control" that coincides with atmospheric warming, the corresponding cloud water path changes are negative because of increased stability. We also find that cloud water path changes are at least 4 times more negative for NW and NE block days than SW and SE block days because of lower Greenland-average total column water vapor (Table 3.2). NW and NE block days tend to transport colder, drier northerly air onto the GrIS (Fig. 3.6C-D). When this already dry air flows downslope to the GrIS margins, it dries further and results in larger cloud water path reductions. Regional moisture availability for different block days also varies by block location because of moisture source region. Column-integrated moisture transport indicates that SW and SE block days source moisture from the North Atlantic Ocean to the south (e.g., Neff et al., 2014; McLeod and Mote, 2015; Mioduszewski et al., 2016; Mattingly et al., 2018), while NW and NE block day moisture originates from the Arctic Ocean and Greenland Sea, respectively, which are colder bodies of water (Nusbaumer et al., 2019). Overall, absolute cloud water paths range from $20\ g/m^2$ to $80\ g/m^2$ over the GrIS during block days (Fig. A.3). Cloud water paths below $40\ g/m^2$ allow more radiative energy to transmit to the surface (Bennartz et al., 2013). As we

see from the composite block cloud water path anomalies, spatial distributions of optically-thin clouds over Greenland vary with block location.

From these results, we can see that cloud anomaly patterns differ by block location, especially between northern quadrant and southern quadrant block days. NW and NE block days produce greater cloud fraction and cloud water path reductions relative to “Control”, especially over western Greenland. In contrast, SW and SE block days enhance (reduce) cloud fraction and cloud water paths over portions of western (eastern) Greenland. These differences arise from 1) block airflow over Greenland’s elevated surface and 2) moisture prevalence and source region. However, cloud fraction and cloud water path changes are spatially similar for each blocking case. As we will see in the following section, cloud properties for different block locations can directly affect energy fluxes received at the surface.

3.3.3 Cloud Radiative Forcing and Block Location

In the previous section, we found that NW and NE quadrant blocking produces greater GrIS-wide cloud fraction and cloud water path reductions than SW and SE block days. We combine our cloud results with MERRA-2 shortwave and longwave cloud radiative forcing data to investigate the impacts of block location on surface radiative energy. To disentangle the effects of clouds on radiative fluxes, we use clear-sky and all-sky shortwave and longwave fluxes to calculate cloud radiative forcing (equation 3.3). Although cloud radiative forcing does not account for net surface energy changes, it is a useful metric for explaining radiative impacts of the actual clouds. All energy fluxes are defined as positive in the downward direction (i.e., into the surface).

Clouds in “All Blocks” and “Control” days produce negative absolute shortwave cloud radiative forcing because of scattering (Fig. 3.7A-B).

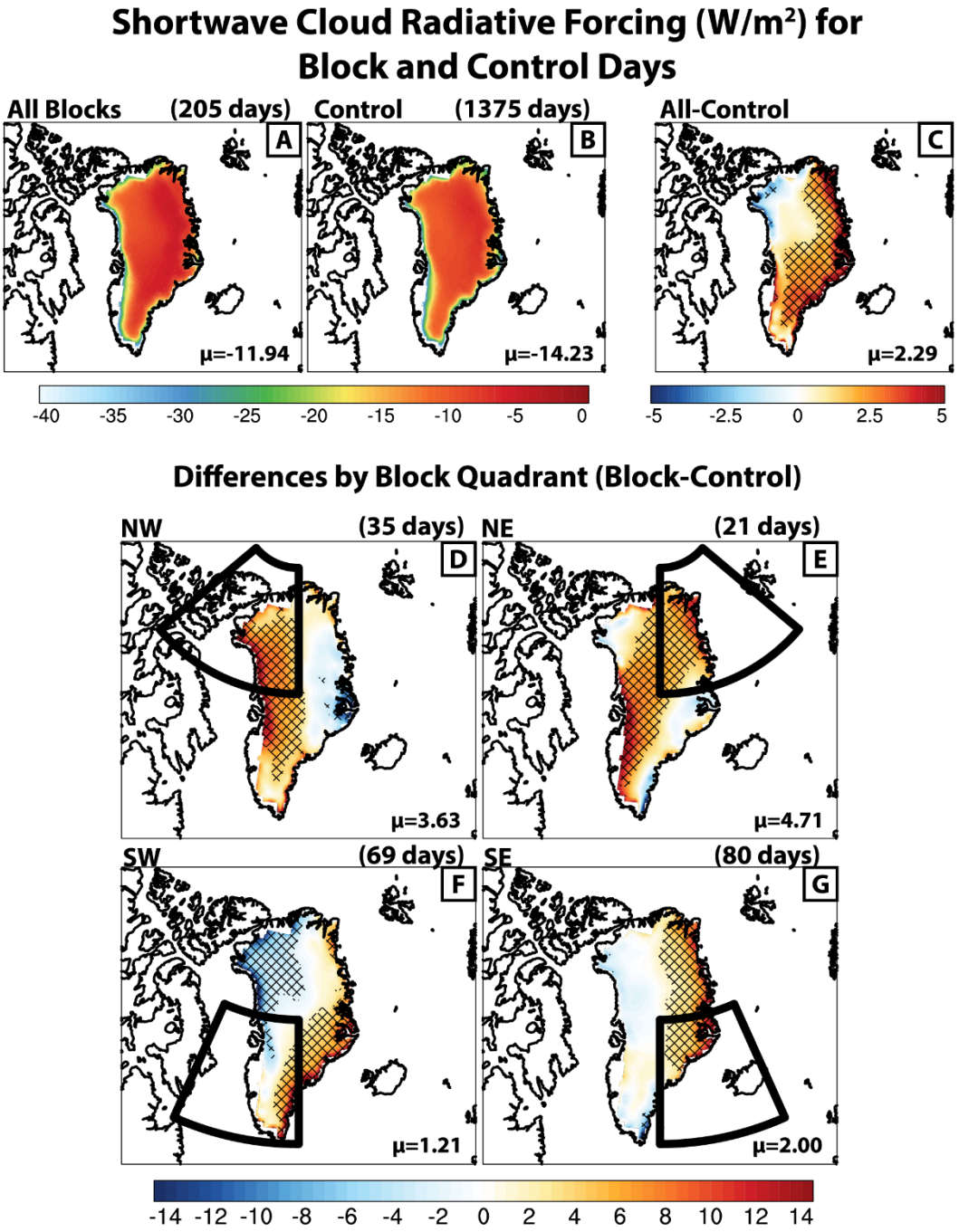

Fig. 3.7: Same as Fig. 3.4, but for MERRA-2 derived surface net shortwave cloud radiative forcing at the surface (W/m^2).

However, because cloud fraction and cloud water path reductions in “All Blocks” reduce scattering above the surface, positive shortwave cloud radiative flux anomalies result over most of the GrIS. Similarly, we find positive (negative) shortwave cloud radiative forcing anomalies for negative (positive) cloud fraction changes in each of the block quadrant cases (Fig. 3.7D-G); NW and NE block days produce significant shortwave cloud radiative forcing enhancements over western Greenland and within their respective block quadrant boundaries, while SW and SE block days exhibit positive shortwave cloud radiative forcing changes over portions of eastern Greenland. Overall, Greenland-average shortwave cloud radiative forcing anomalies are largest for NW and NE block days ($+3.63\ W/m^2$ and $+4.71\ W/m^2$ respectively; Fig. 3.7E, G).

We see the changes of the opposite sign in longwave cloud radiative forcing during blocking (Fig. 3.8). Greenland blocking produces significantly negative surface longwave cloud forcing (i.e., less absorbed longwave energy at the surface). “All Blocks” longwave cloud radiative forcing anomalies are significantly negative over most of the GrIS. Similarly, blocking in each block quadrant produces negative longwave cloud radiative forcing anomalies in regions of reduced cloudiness. Despite positive atmosphere temperature anomalies (i.e., Fig. 3.9), reduced cloud cover decreases downwelling longwave energy (i.e., Shupe and Intrieri, 2004; Miller et al., 2015) while surface-based upwelling longwave energy remain approximately constant (not shown), which produces negative changes in net longwave cloud radiative forcing (van As et al., 2012; Lenaerts et al., 2019).

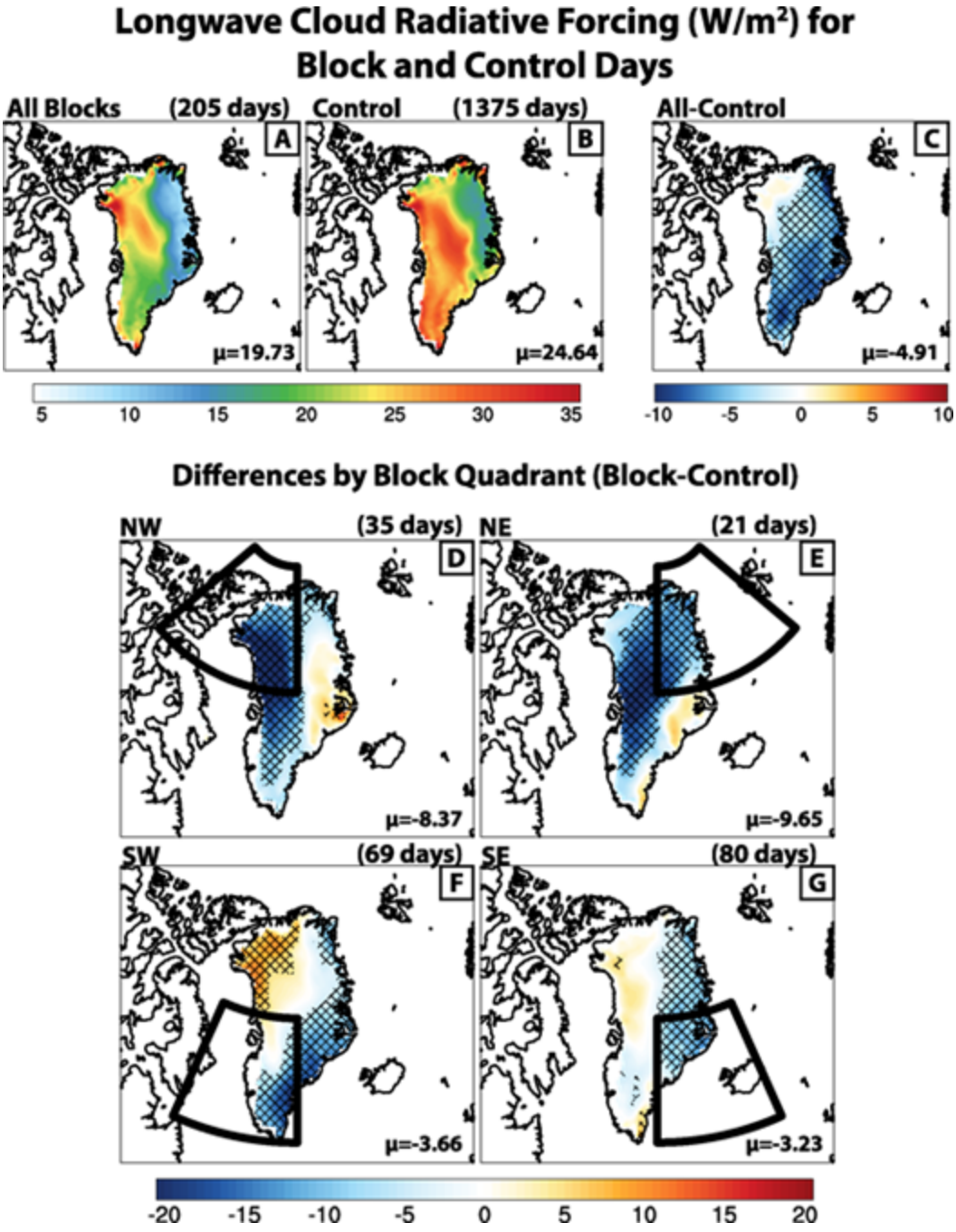

Fig. 3.8: Same as Fig. 3.4, but for MERRA-2 derived surface net longwave cloud radiative forcing at the surface (W/m^2).

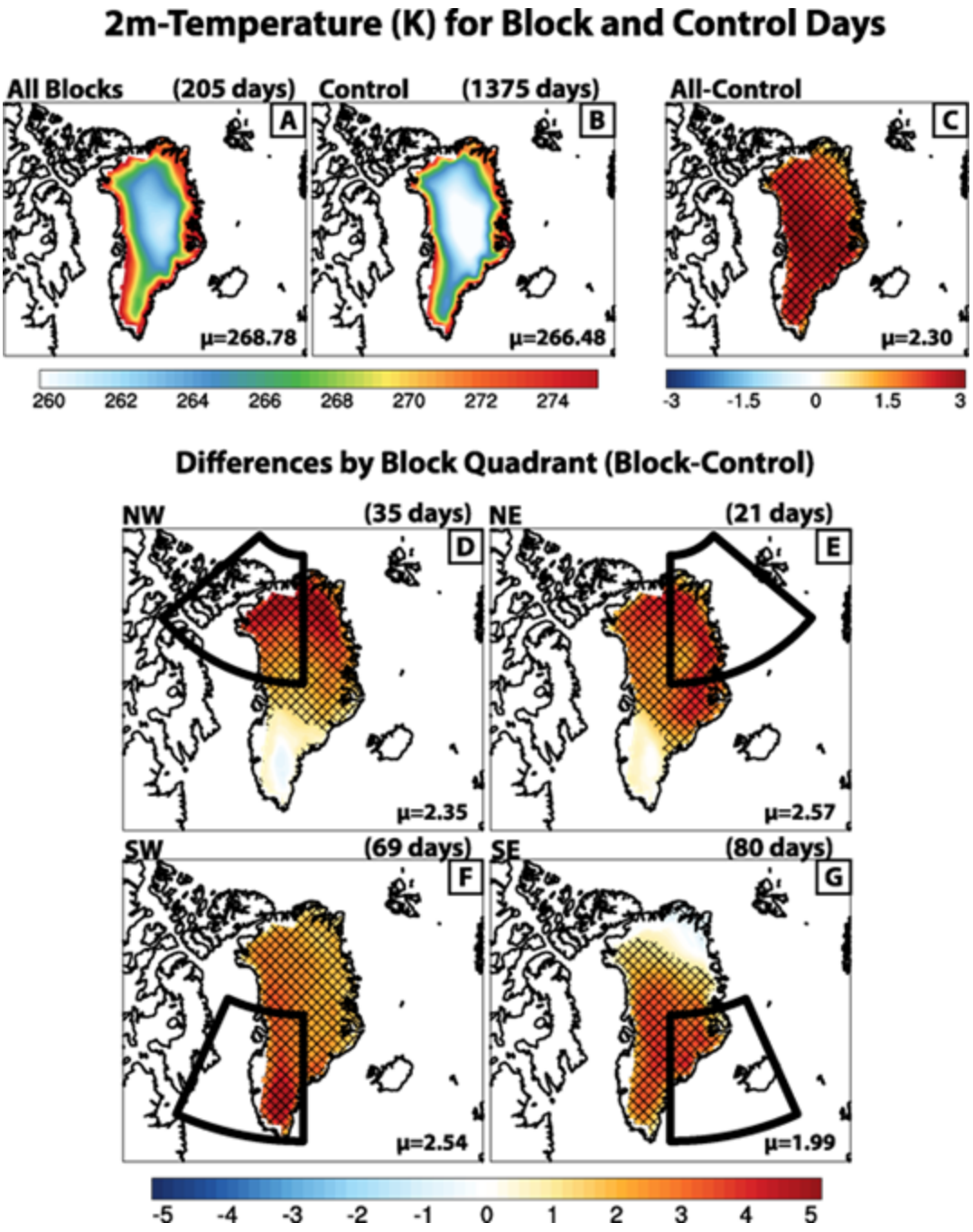

Fig. 3.9: Same as Fig. 3.4, but for MERRA-2 2m-temperature (K).

Unlike our shortwave cloud radiative forcing results, we find NW and NE blocking produces Greenland-average longwave cloud radiative forcing reductions ($-8.37\ W/m^2$ and

$-9.65\ W/m^2$) that are 2-3 times greater than those for SW and SE block days because of larger cloud fraction and cloud water path reductions.

When we compute net cloud radiative forcing anomalies for each blocking case (Fig. 3.10), we find that longwave cloud radiative forcing anomalies outweigh shortwave cloud radiative forcing anomalies and result in dominantly negative net cloud radiative forcing. These net cloud radiative forcing anomaly patterns resemble cloud fraction and cloud water path changes during all blocking scenarios. The larger impact of longwave cloud radiative forcing we find in net cloud radiative forcing anomalies aligns with previous studies on Greenland cloud radiative forcing (Miller et al., 2015; Van Tricht et al., 2016). NW and NE blocks produce the most negative net cloud radiative forcing changes ($-4.75\ W/m^2$ and $-4.94\ W/m^2$, respectively) that have magnitudes approximately 2 times larger than net cloud radiative forcing anomalies for SW and SE block days ($-2.45\ W/m^2$ and $-1.23\ W/m^2$).

NW and NE block days produce larger positive shortwave cloud radiative forcing anomalies and more negative longwave cloud radiative forcing anomalies than southern quadrant blocking because of greater cloud cover reductions. In the case of shortwave cloud radiative forcing changes, positive ice cloud fraction and negative liquid cloud fraction changes during NE and SE block days also increase net shortwave cloud radiative forcing (compared to NW and SW block days, respectively) by reducing cloud albedo. For each block location, however, longwave cloud radiative forcing changes outweigh shortwave cloud radiative forcing changes, resulting in negative cloud radiative effects over the GrIS because of reduced cloudiness. These findings demonstrate that block location is important not only for cloud changes over Greenland but also for associated cloud radiative forcing anomalies.

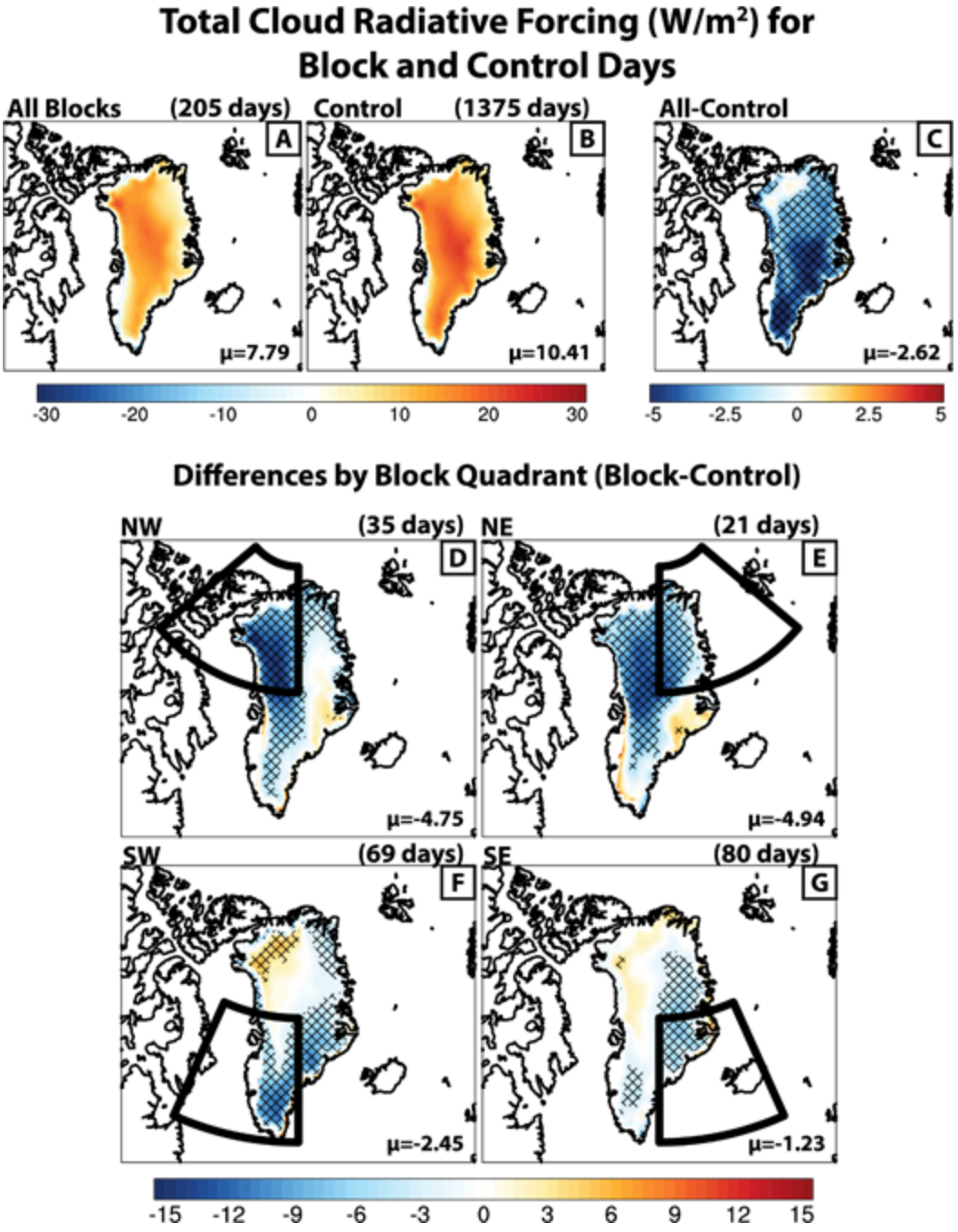

Fig. 3.10: Same as Fig. 3.4, but for MERRA-2 derived total surface cloud radiative forcing (W/m^2).

3.3.4 Surface Energy Fluxes and Block Location

Because changes in net surface energy fluxes are impacted by factors other than cloud presence (e.g., air temperature, moisture availability, and surface albedo), we calculate net surface shortwave and longwave flux anomalies for each block location. Overall, Greenland-average net radiative flux (i.e., the sum of net shortwave and net longwave fluxes) increases for all blocking cases (Figs. A2 and A.3). Unlike southern quadrant block days, negative net longwave flux anomalies produced by northern quadrant blocking partially offset positive changes in net shortwave fluxes. SW and SE block days produce positive surface shortwave and longwave flux anomalies (SW block day net longwave responses are quite small) because of smaller cloud fraction reductions and moisture transport processes (Fig. A.4). These positive net radiative flux anomalies correspond to negative Greenland-average total cloud radiative forcing, which highlights the importance of other phenomena apart from clouds for impacting surface radiative fluxes.

Sensible and latent heat fluxes are also important for total surface energy input during blocking. As we can see from Fig. 3.11, significant sensible heat flux anomalies are dominantly positive for all block locations. However, NE and SE block days produce larger Greenland-wide sensible heat anomalies ($+8.98\ W/m^2$ and $+5.49\ W/m^2$, respectively) than NW and SW block days. Since warm air advection and adiabatic warming of descending airflow have both been shown to contribute to greater downward-directed sensible heat flux (e.g., Box et al., 2012; Fausto et al., 2016; Välisuo et al., 2018), we examine 2m-temperature anomalies and wind patterns for these cases. All block locations exhibit significantly positive 2m-temperature anomalies (Fig. 3.9), but block circulation patterns for NE and SE block days suggest large regions of descending adiabatic warming and onshore southerly airflow over western Greenland,

respectively (Fig. 3.5). NW and SW block days, on the other hand, produce large areas of adiabatic cooling as air ascends to higher GrIS elevations and results in smaller sensible heat anomalies.

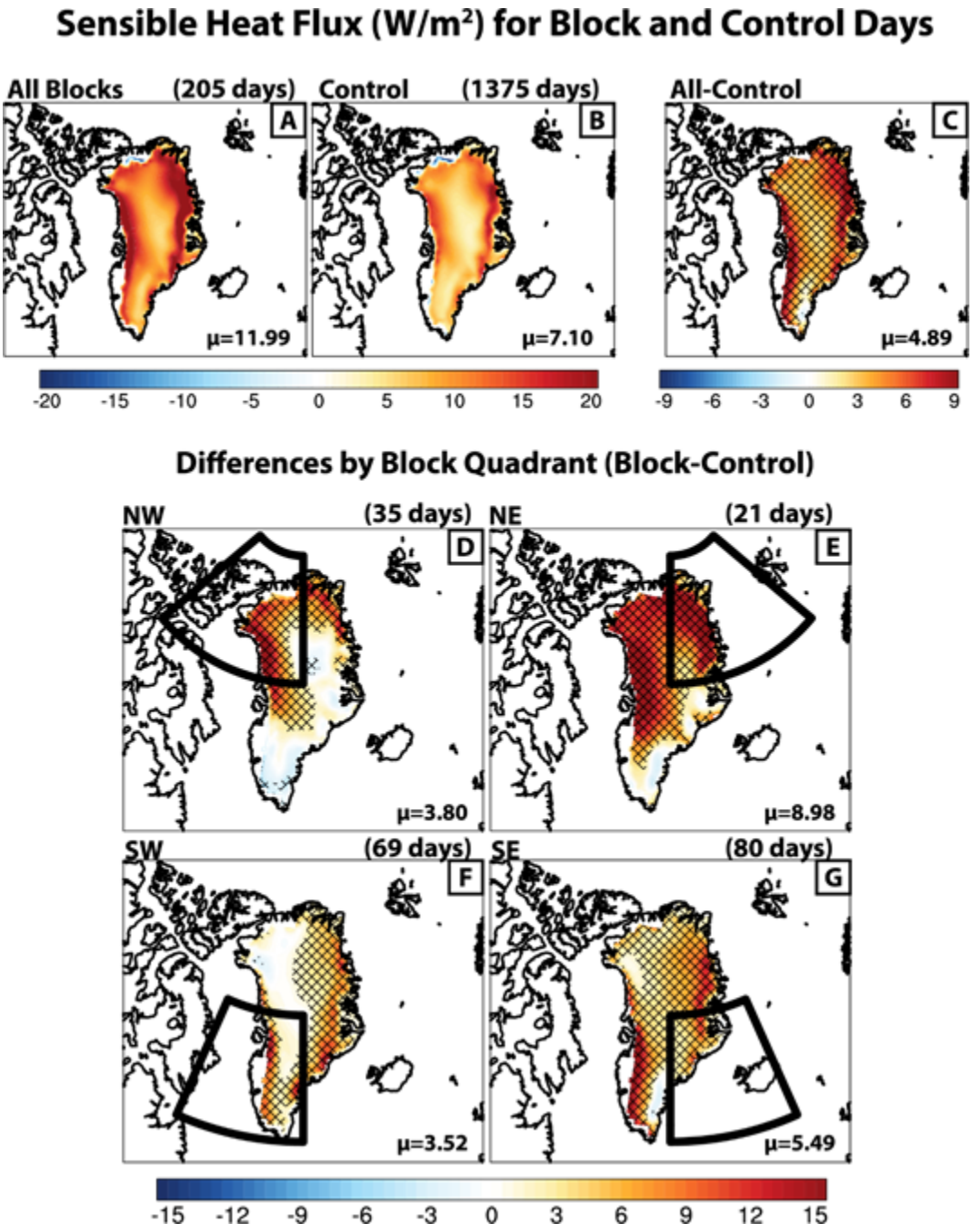

Fig. 3.11: Same as Fig. 3.4, but for MERRA-2 sensible heat flux (W/m^2). Positive quantities are directed into the surface.

Although latent heat flux anomalies are non-negligible, they are small in comparison with radiative and sensible heat fluxes, so we do not include these findings here (see supplementary information Fig. A.6).

Now that we have examined cloud radiative forcing, radiative fluxes, and turbulent heat fluxes associated with different Greenland block locations, we will look at the impact of block location on total surface energy flux (E_{total}), defined as the sum of net shortwave, net longwave, sensible, and latent heat fluxes, respectively:

$$E_{total} = SW_{net} + LW_{net} + SH + LH \quad (3.4).$$

All blocking locations produce large positive surface energy flux changes (Fig. 3.12) along the lower albedo GrIS margins (e.g., Tedesco et al., 2011). With the exception of NW block days, we also calculate significant positive changes over sub-areas of the GrIS interior. These net energy flux changes in the accumulation zone are statistically significant relative to "Control" because the high albedo snow surface reduces energy absorption and have important snowmelt implications (e.g., van den Broeke et al., 2009). In contrast, NW block days produce significantly negative net surface energy flux anomalies over most of the central GrIS because of the combined influence of cloud changes and northerly cold air advection. Reduced cloud cover produces negative net fluxes that outweigh positive sensible heat flux changes that are limited by the colder, drier overlying air. Negative net energy flux anomalies over central Greenland during NW block days counteract positive changes along the GrIS margins and produce the lowest Greenland-average net surface flux change ($+7.12\ W/m^2$) of all block locations. Positive average net shortwave energy ($+10.75\ W/m^2$) is the largest contributor to enhanced net surface energy and more than offsets negative net longwave energy ($-6.14\ W/m^2$) change. Out of the remaining blocking locations, NE block days produce the largest Greenland-wide net surface

energy change ($+12.36\ W/m^2$) because of the combined influence of spatially-averaged net shortwave ($+7.10\ W/m^2$) and sensible heat flux ($+8.98\ W/m^2$) anomalies.

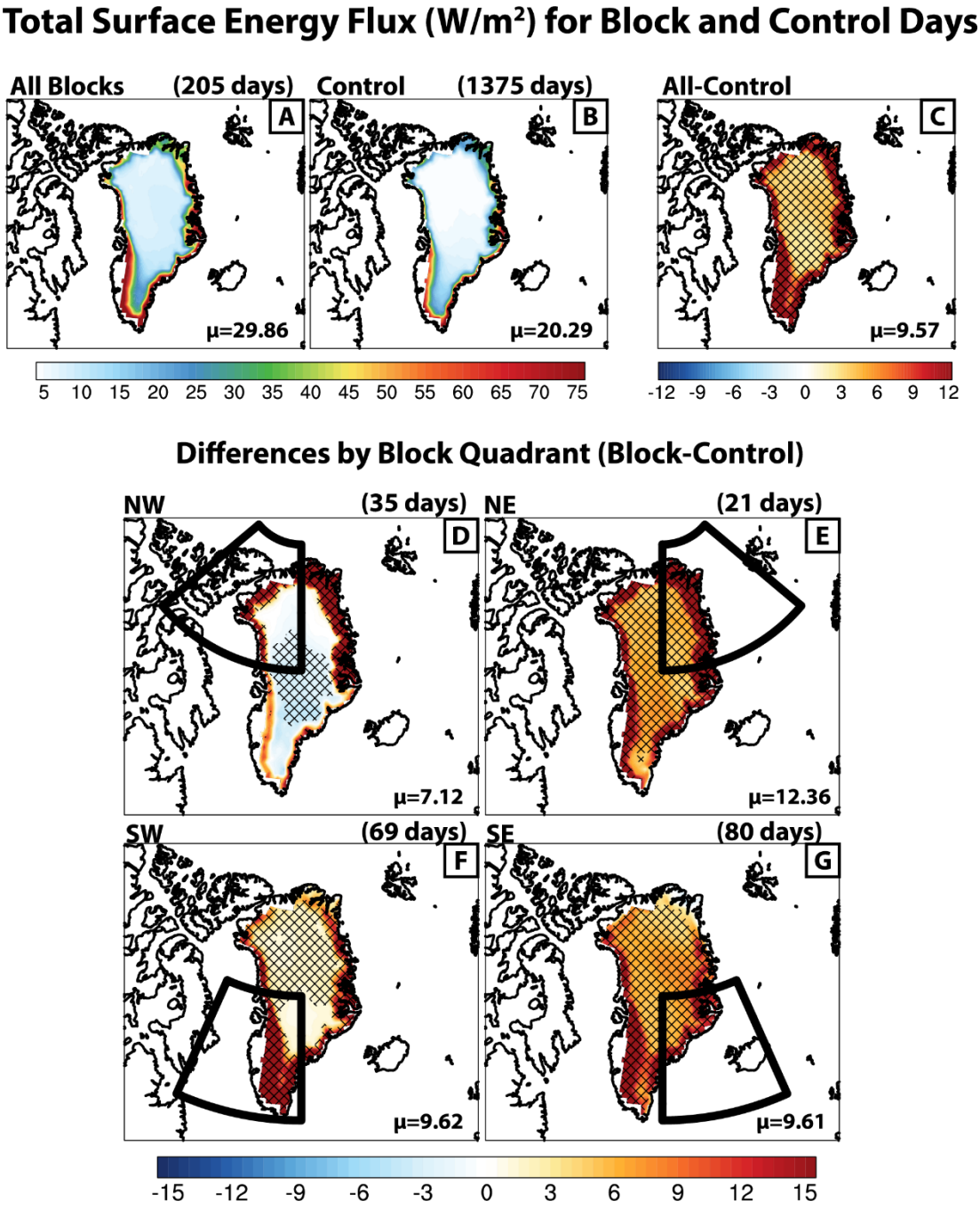

Fig. 3.12: Same as Fig. 3, but for MERRA-2 derived total surface energy flux (W/m^2).

Although “All Blocks”, SW, and SE block days produce similar spatial patterns and Greenland-wide average net surface energy flux anomalies ($+9.57\ W/m^2$, $+9.61\ W/m^2$, and $+9.62\ W/m^2$, respectively), the relative contribution of component fluxes to total energy change varies by block location. Net shortwave ($+5.08\ W/m^2$) and sensible heat flux ($+4.89\ W/m^2$) anomalies are almost equally responsible for positive Greenland-wide surface energy changes during “All Blocks”. In contrast, spatially-averaged net shortwave energy change ($+6.50\ W/m^2$) is responsible for over 60% of the corresponding net surface energy change during SW block days and average sensible heat change ($+5.49\ W/m^2$) produces almost 60% of total surface energy flux change during SE block days. As with NE block days, sensible heating is a large contributor to positive surface energy flux change during SE block days because from warm air advection from lower latitudes onto the GrIS that results from the composite block location.

Greenland block location affects spatial and Greenland-average surface energy fluxes through the production of different cloud patterns, moisture transport and source region, and adiabatic heating resulting from orographic airflow. NW block days are unique from other blocking in other locations because they produce negative net surface energy flux anomalies over the central GrIS and result in the lowest Greenland-average net surface energy flux change. Although we find similar total surface energy flux anomaly patterns between the remaining blocking cases, moisture and airflow changes over the GrIS dictate the relative contribution of turbulent and radiative heat flux anomalies. Sensible heat fluxes contribute more to net surface energy flux changes for NE and SE block days because of enhanced warm air advection and subsidence over southern and western Greenland. Net solar energy anomalies are the largest contributing energy source to net surface energy changes for NW and SW block days.

3.4 Conclusion

In this study, we use a combination of MERRA-2 meteorological reanalysis data and MODIS collection 6, level 2 cloud data to assess the impacts of Greenland block location on regional clouds and Greenland Ice Sheet (GrIS) surface energy fluxes in the summer months of 2002-2018. We find block days using a modified setup of the D-S block detection algorithm (Dunn-Sigouin et al., 2013) and separate individual block days using uniquely defined equal-area block quadrants over Greenland. We use moisture transport, winds, and temperature data to explain how block location affects clouds and surface energy fluxes and compare these results on a quadrant-by-quadrant basis.

From 2002 through 2018, we find 30 Greenland block events in June, July, and August (JJA), totaling 205 block days. Of these years, the summers of 2003, 2006-2008, 2012, and 2015-2016 had higher-than-average block day counts, while no blocking activity occurs in 2002, 2013, or 2017. Although we verify block activity for each day in our record, we emphasize that block days found by the D-S algorithm (and others) are sensitive to changes in algorithm threshold values. Although most (73%) of these block days are located in the SW and SE block quadrants, understanding cloud and energy flux changes during NW and NE block days (27% of all block days) is also important to fully understanding Greenland blocking.

All Greenland block locations produce negative Greenland-average cloud fraction and cloud water path changes, as demonstrated previously (e.g., Lim et al. 2016; Mioduszewski et al., 2016; Hofer et al., 2017; Tedesco and Fettweis, 2019). However, the extent to which cloud coverage and water path decrease, as well as the cloud change patterns over Greenland, vary by block location. Negative cloud fraction and cloud water path anomalies are at least four times greater for NW and NE block days than SW and SE block days because SW and SE quadrant

block days import warmer, moister air over the GrIS to damp the extent of cloud reduction caused by block dynamics.

Cloud radiative forcing anomalies vary in magnitude and spatial distribution for different block locations. Greenland-average shortwave cloud radiative forcing values are greater for NW and NE block days and correspond to large cloud fraction and cloud water path reductions. However, cloud water path changes in eastern Greenland blocks produce greater shortwave cloud radiative forcing anomalies than western Greenland blocks at the same latitude. Longwave cloud radiative forcing and total cloud radiative forcing anomalies are negative for all block locations, with NW and NE block days producing anomalies at least 2 times as great as SW and SE block day anomalies. Larger longwave cloud radiative forcing anomaly magnitudes indicate that Greenland blocking cloud changes negatively impact the amount of radiative energy absorbed by the surface.

During all except NW block days, total surface energy flux is positive over most of the GrIS, with the largest flux anomalies located along the ice sheet margins and minimal yet statistically significant increases over the central GrIS. Although NW block days also produce large positive net surface energy anomalies over the GrIS margins, net energy anomalies are negative over central Greenland. Large cloud reductions and northerly cold air advection over the central GrIS greatly reduce net longwave surface flux to more than offset the positive surface energy contribution of net shortwave and sensible heat anomalies. Because of these negative total energy flux changes, NW block days produce the least positive Greenland-average net surface net energy change ($+7.12\ W/m^2$). NE block days produce the greatest Greenland-average net energy flux change ($+12.36\ W/m^2$) because of the combined influence of large positive net shortwave and sensible heat flux anomalies. Although net surface energy flux

anomalies are similar for “All Blocks”, SW, and SE block days, the component flux anomalies that contribute to these changes are different because of changes in dominant air and moisture source regions.

These results all highlight the importance of block location for cloud and surface energy flux patterns over the GrIS. However, some of our chosen methods could affect these findings. One of the most significant constraints in this study is block detection itself. Because there is no concrete definition for blocking, we can justify changes we make to the D-S algorithm thresholds. However, changing these thresholds or using a different detection method to find Greenland blocks from meteorological data could affect the block days identified.

This study demonstrates that blocks in northern Greenland more effectively reduce cloud cover and decrease total cloud radiative forcing at the surface. Along with clouds, air temperature and moisture also contribute to surface energy changes during blocking, especially for blocking over southern Greenland that draws warm, moist North Atlantic air over the GrIS. Our findings can be used to further understand the impact of block location on GrIS snowmelt processes through the examination of clouds and surface energy fluxes.

Chapter 4. Future Greenland Ice Sheet Surface Flux Anomalies Produced by Atmospheric Blocking in the CMIP6 Models

(Ward et al., 2020b, in prep)

4.1 Introduction

Summertime blocking activity (i.e., persistent, quasi-stationary anticyclonic circulation (Rex, 1950)) has increased over Greenland since the start of the 21st century (Fettweis et al., 2013; Rajewicz and Marshall, 2014; McLeod and Mote, 2015; Hanna et al., 2018a) and was accompanied by increased Greenland Ice Sheet (GrIS) surface energy and snowmelt (Fettweis et al., 2011, 2013; Box et al., 2012; Belleflamme et al., 2013; Hanna et al., 2014; Neff et al., 2014; Lim et al., 2016; Mioduszewski et al., 2016; Delhasse et al., 2018; Hanna et al., 2018a). Blocking induces melt by decreasing cloud cover in the high pressure region (e.g., Hofer et al., 2017), advecting warm, moist air over the GrIS (van den Broeke et al., 2011; Franco et al., 2013; Häkkinen et al., 2014; Fausto et al., 2016; Tedesco et al., 2016b; Välisuo et al., 2018), and promote cloud growth via orographic airflow processes (Bonne et al., 2015). As we demonstrate in Chapter 3 (Ward et al., 2020; submitted), energy and cloud response magnitudes to historical blocking depend on block location. Although atmospheric temperature, moisture, and energy flux responses to blocking can individually affect GrIS surface mass balance, the modeled response of melt to blocking with increased temperatures is two times greater than the response for temperature increase alone (Delhasse et al., 2018; Hofer et al., 2019). The summers of 2012,

2015, and 2019 exhibited extensive GrIS snowmelt (Nghiem et al., 2012; Tedesco et al., 2016b; Tedesco and Fettweis, 2020) that was coincident with frequent blocking activity. During one specific 2012 melt episode (10-12 July) (Nghiem et al., 2012), clouds, moisture transport, and blocking all contributed to snowmelt over >98% of the GrIS surface (Bennartz et al., 2013; Neff et al., 2014; Mattingly et al., 2018). Relative contributions of these phenomena to observed surface melt varied over the GrIS.

Greenland blocking produces radiative and non-radiative energy flux responses over the GrIS. A large contributor to total surface energy during blocking is increased net shortwave flux response to subsidence-produced cloud reduction (Lim et al., 2016; Hofer et al., 2017; Tedesco and Fettweis, 2020). Although the GrIS surface is highly reflective, pre-conditioned snow that has undergone previous melt will absorb more sunlight during blocking. Over western Greenland, block-based warm air advection increases sensible heat input into the GrIS, especially along the GrIS margins and lower ablation zones (Fausto et al., 2016; Lim et al., 2016; Cullather and Nowicki, 2018). The impact of net longwave fluxes during blocking is more uncertain. Southerly warm air advection increases lower atmosphere air temperatures and enhances downwelling longwave fluxes, while the absence of clouds negates this effect (Hofer et al. 2017; Cullather and Nowicki, 2018). Variability associated with block-produced cloud spatial patterns, preexisting GrIS albedo conditions, and solar energy seasonality leads to uncertainty in the relative impacts of shortwave and longwave energy responses to blocking. Cullather and Nowicki (2018) found positive net longwave flux anomalies that correspond to positive 500mb geopotential height anomalies indicative of blocking for each GrIS basin melt location. On the other hand, Hofer et al. (2017) calculate negative net longwave flux anomalies over the GrIS because of greater upwelling longwave flux changes that result from surface warming.

There is more uncertainty in future Greenland blocking frequencies, structure (i.e., circulation, geopotential height, and temperature), and associated GrIS surface energy fluxes. Blocking frequencies in the larger North Atlantic region are projected to remain the same (Delhasse et al., 2018) or decrease slightly (Dunn-Sigouin and Son, 2013; Hanna et al., 2018b) in RCP 8.5 warming scenario Coupled Model Intercomparison Project, phase 5 (CMIP5) model output. Downwelling shortwave energy will likely decrease as longwave downwelling increases because of a warmer future regional mean state combined with greater atmospheric moisture availability for cloud production over Greenland (Delhasse et al., 2018). Despite these findings, the validity of CMIP5 data to forecast blocking trends and the resulting surface energy fluxes is questionable. Hanna et al. (2018b) report that CMIP5 models are not only unable to reproduce summer Greenland blocking frequencies from 2000 onward, but they also do not capture the hypothesized enhancement in geopotential heights that should result from atmospheric warming. The CMIP6 (i.e., CMIP, phase 6) data archive is the newest global climate model output repository containing simulations from the newest model versions (e.g., Eyring et al., 2016). These new data could be an excellent tool for reexamining Greenland blocking trends.

Future Greenland blocking trends and surface energy flux responses over the GrIS have not yet been explored with CMIP6 output. We will use this newly-released data to analyze how Greenland blocking total surface energy flux anomalies (and the relative contributions of component fluxes) change in the middle of the twenty-first century (2040-2059) and the end of the twenty-first century (2080-2099) for the highest projected warming scenario. To complete this project, we first describe the data we use, our methods for block detection, and statistical analysis techniques in the methods section (4.2). We analyze these results and their implications

for Greenland's future climate in the Results (4.3) section before summarizing our findings and their implications for future research in the Conclusion (4.4).

4.2 Methods

We use historical and future global climate model simulations from the Coupled Model Intercomparison Project, phase 6 (CMIP6) data archive to characterize GrIS surface energy flux responses to blocking and how these change with time (Eyring et al., 2016). We define three 20 year periods in historical and future simulations to examine these responses: 1) "Historical" (1986-2005) (i.e., Meredith et al., 2019), 2) "Mid-Century" (2040-2059), and 3) "Late-Century" (2080-2099). For Mid-Century and Late-Century, we analyze shared socioeconomic pathway (SSP) 5 (i.e., O'Neill et al., 2017) simulations with a representative pathway concentration (RCP) value of 8.5 W/m^2 (RCP 8.5; van Vuuren et al., 2011). This SSP/RCP combination represents the scenario in which humanity continues the "business-as-usual" approach while increasing average global surface radiative forcing by 8.5 W/m^2. O'Neill et al. (2017) defines this SSP/RCP outcome (hereafter referred to as SSP585) by continued use of fossil fuels, infrastructure built around fossil fuels, and minimal international cooperation for energy policy change. Out of all available CMIP6 future simulations, the SSP585 scenario represents the largest warming projection (O'Neill et al., 2017) by the end of the 21st century, which has important implications for GrIS surface mass balance changes.

We detect individual blocks for all time periods and models using daily-resolved 500mb geopotential height output (more details about block detection methods are in the next paragraph). Daily-resolved fields are necessary for blocking because 1) blocking occurs on time scales of days to weeks (Rex et al., 1950), and 2) separating out individual blocks from non-

block days produces a more accurate representation of the impacts of blocking on GrIS surface processes, as opposed to seasonal averages. We assess daily net shortwave (SW_{net}), net longwave (LW_{net}), sensible heat (SH), and latent heat (LH) fluxes individually for each model and time period. Net shortwave and net longwave results are produced by subtracting the corresponding upwelling fluxes from downwelling fluxes. Individual energy fluxes are summed together to calculate daily net surface energy flux (E_{Total}):

$$E_{Total} = SW_{net} + LW_{net} + SH + LH \quad (4.1).$$

In equation 4.1, all component fluxes are positive when directed into the surface (i.e., downward).

We select the five CMIP6 models (Table 4.1) with daily-resolved geopotential height and surface energy flux output.

Table 4.1: CMIP6 Model Information. Spatial resolutions are defined with latitude by longitude dimensions. Hereafter, we refer to models by their "Model Alias".

Model	**Model Alias**	**Institution, Country**	**Simulation Variant**	**Spatial Resolution**
CanESM5	CanESM	CCCma, Canada	r1i1p1f1	T63 (2.8° × 2.8°)
CESM2	CESM	NCAR, USA	r1i1p1f1	0.9° × 1.25°
CESM2-WACCM	WACCM	NCAR, USA	r1i1p1f1	0.9° × 1.25°
CNRM-CM6-1	CNRM	CNRM, France	r1i1p1f2	TL127 (1.4° × 1.4°)
UKESM1-0-LL	UKESM	MOHC, UK	r1i1p1f2	N96 (1.875° × 1.25°)

Future CNRM upwelling shortwave fluxes are only available in a high resolution (i.e., not listed in Table 4.1) format, so we use bilinear interpolation to regrid these data to the native CNRM horizontal resolution. Finally, we calculate blocking and surface energy flux statistics for MERRA-2 reanalysis data so as to disentangle potential biases within the chosen historical CMIP6 simulations and extrapolate mid- and Late-Century biases (Gelaro et al., 2017).

Because blocks at the beginning of June (end of August) can extend into late May (early September), we search for block days in the Historical, Mid-Century, and Late-Century period data from May 16 through September 15. Block days from May or September are only included when the block event extends into June or starts in late August. To find blocks, we use a multi-step version of the Greenland Blocking Index (GBI) method (Hanna et al., 2018b). More specifically, we calculate two area-weighted average 500mb geopotential heights: "GBI1" over the Greenland region ($60-80°N$ and $20-80°W$) and the zonal mean from $60-80°N$ over all longitudes (i.e., $\overline{Z_{500}}$) (Hanna et al., 2018b). We find the final GBI index, GBI2 using the equation 4.2:

$$GBI2 = GBI1 - \overline{Z_{500}} \quad (4.2).$$

Unlike GBI1 alone, GBI2 reduces the likelihood of detecting false block days that result from atmospheric warming-based geopotential height increases (i.e., Belleflamme et al., 2013). Once we calculate GBI2 for all days in a given dataset, we standardize these values using the respective daily GBI2 climatology. If five consecutive days produce standardized GBI2 values exceeding a GBI2 value of 0.75, these days constitute a blocking event. A GBI2 threshold of 0.75 allows for variability in blocking strength and is more inclusive of ridging and weak closed blocks that can both impact GrIS surface processes (Belleflamme et al., 2015; Mioduszewski et al., 2016; Tedesco et al., 2016b; Hofer et al., 2017).

All June, July, and August (JJA) days that are not block days are classified as "non-block", or "Control" days. Because the purpose of this study is to understand how surface energy fluxes during Greenland blocking compare to "Control" surface energy fluxes, we statistically compare block and "Control" days separately for each data source and each time span (e.g., Historical, Mid-Century, and Late-Century). For this reason, we do not use historical "Control"

days as the control for future simulations produced by the same global climate model. Radiative and non-radiative surface energy flux anomalies for block days are calculated over the respective global climate model grid. Greenland-wide average surface energy flux changes are area-weighted and only computed for GrIS grids with a minimum of 50% land ice coverage. We use MERRA-2 land ice fraction data to inform the status of each grid. Since the models have different spatial resolutions (Table 4.1), we regrid the MERRA-2 land ice fraction for each of the models.

4.3 Results and Discussion

4.3.1 Blocking Statistics for CMIP6 and MERRA-2

We first examine Greenland blocking frequency, GBI2, and GBI1 trends in the Historical, Mid-Century, and Late-Century time periods for MERRA-2 and each CMIP6 model. Summer season block day counts are highly variable for all time periods and for all models (Fig. 4.1). We attribute this blocking activity variability to planetary-scale dynamics, like the North Atlantic Oscillation (NAO) (e.g., Hanna et al., 2015; Lim et al., 2016). Average summertime GBI1, a proxy for Greenland blocking activity, is anticorrelated with the North Atlantic Oscillation (NAO) Index (e.g., Hanna et al., 2016), but whether NAO triggers blocking or vice versa is still unknown. Due to interannual variability in block day counts, we do not find any statistically significant trends in block day counts with respect to time for any model.

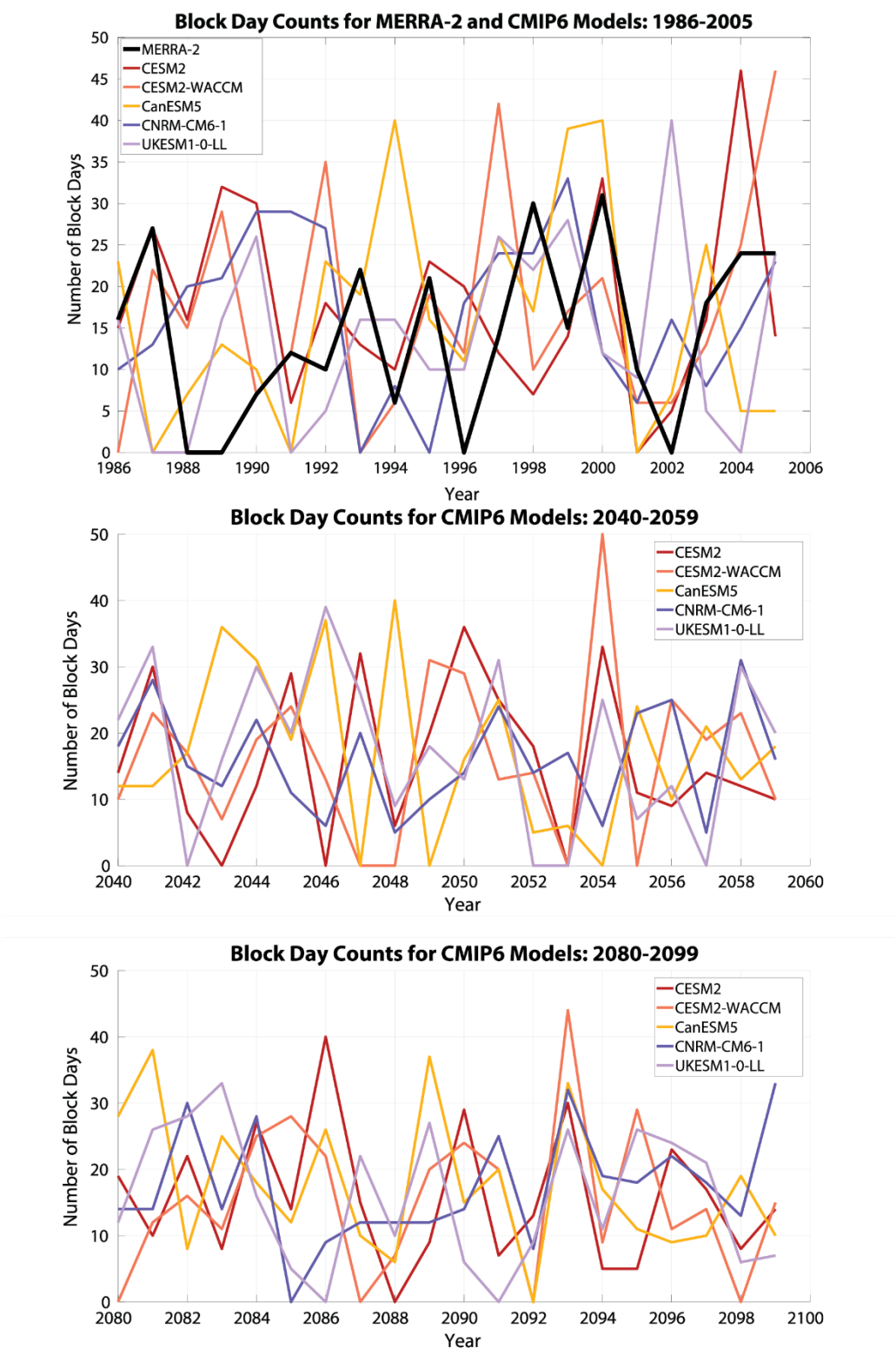

Fig. 4.1: Block day counts per summer (UKESM summer length is 120 days instead of 123 days) for MERRA-2 and CMIP6 models over each time span.

Although previous studies have cited increasing summer Greenland blocking activity from 2000 through the present (e.g., Fettweis et al., 2013; Hanna et al., 2018b), we only analyze blocks from 1986-2005 and do not include the most recent block activity enhancements from the mid-2000s onward (e.g., Tedesco et al., 2011, 2016b; Tedesco and Fettweis, 2020).

We examine average summer day count, GBI2, and GBI1 statistics to further characterize Greenland blocking activity and extrapolate atmospheric changes over time (Table 4.2).

Table 4.2: CMIP6 and MERRA-2 Summer-Average Block Statistics (123 total possible days)*

Model/Reanalysis	**Variable**	**1986-2005**	**2040-2059**	**2080-2099**
CESM	Day Count	17.85	15.95	15.75
	GBI2	33.13	29.42	37.99
	GBI1	5538.14	5651.60	5727.49
WACCM	Day Count	17.15	16.35	15.35
	GBI2	39.02	48.92	29.22
	GBI1	5545.39	5632.99	5709.54
CanESM	Day Count	16.30	17.10	17.60
	GBI2	50.96	48.36	27.21
	GBI1	5603.26	5672.96	5724.86
CNRM	Day Count	16.80	16.10	17.35
	GBI2	71.58	51.99	42.40
	GBI1	5623.43	5641.64	5710.88
*UKESM**	Day Count	14.05	17.55	15.75
	GBI2	43.55	35.23	17.55
	GBI1	5596.74	5658.70	5731.41
MERRA-2	Day Count	14.35	--	--
	GBI2	36.85	--	--
	GBI1	5576.82	--	--

*UKESM summer season is 120 days long.

CESM and WACCM produce block day count reductions in the future. In contrast, CanESM block days increase and CNRM and UKESM average day count changes are non-monotonic with time. Like CMIP5 models (e.g., Dunn-Sigouin and Son, 2013), CMIP6 models do not produce robust Greenland blocking frequency changes in future simulations. All models produce greater GBI1 values with time, which we attribute to continuing atmospheric warming through the end of the 21st century in the SSP585 case (van Vuuren et al., 2011). However, average GBI2

changes are in disagreement between the models. In CanESM, CNRM, and UKESM, GBI2 averages decrease over time, while CESM and WACCM GBI2 average trends are non-monotonic (Table 4.2). We believe these GBI2 inconsistencies highlight differences in dynamical processes between each of these models. GBI2, which is the difference between Greenland- and northern high latitude-average 500mb geopotential height (equation 4.2, Section 4.2), is useful for determining the relative strength of Greenland blocks relative to the average high latitude geopotential height conditions. Lower GBI2 values indicate smaller differences in Greenland-regional geopotential heights and imply less intense blocking conditions. We hypothesize that increasing (decreasing) average block day counts (GBI2) in CNRM, CanESM, and UKESM could result in more frequent, yet weaker, blocking activity over Greenland at the end of the 21st century.

Spatial distributions of 500mb geopotential height for each case are shown in Fig. 4.2. With the exception of CNRM (Fig. 4.2J-L), MERRA-2 and CMIP6 model average Greenland block 500mb geopotential heights form anticyclonic ridges, regardless of time period. We see ridging because of varying strengths in blocks found using the GBI2 detection technique (Section 4.2). Some block days are likely weak ridges while others are cut-off high pressure systems. Closed geopotential height isolines in CNRM correspond to the highest average GBI2 values, which suggests that the dynamical processes in CNRM favor stronger Greenland blocking than the other models.

Overall, inter-model Greenland blocking variability among the CMIP6 models in our ensemble is quite high. Furthermore, we do not find any change in Greenland blocking seasonal frequencies over any time period. Summertime blocking activity has increased over Greenland since 2000 (e.g., Fettweis et al., 2011, 2013), but we do not see this trend because of how we define Historical blocking. Although average GBI1 increases into the future for all models, we find varying trends in GBI2 that highlight different dynamical processes between the models. However, despite inter-model variability in spatially-averaged Greenland blocking statistics, composite block day geopotential height maps exhibit anticyclonic circulation.

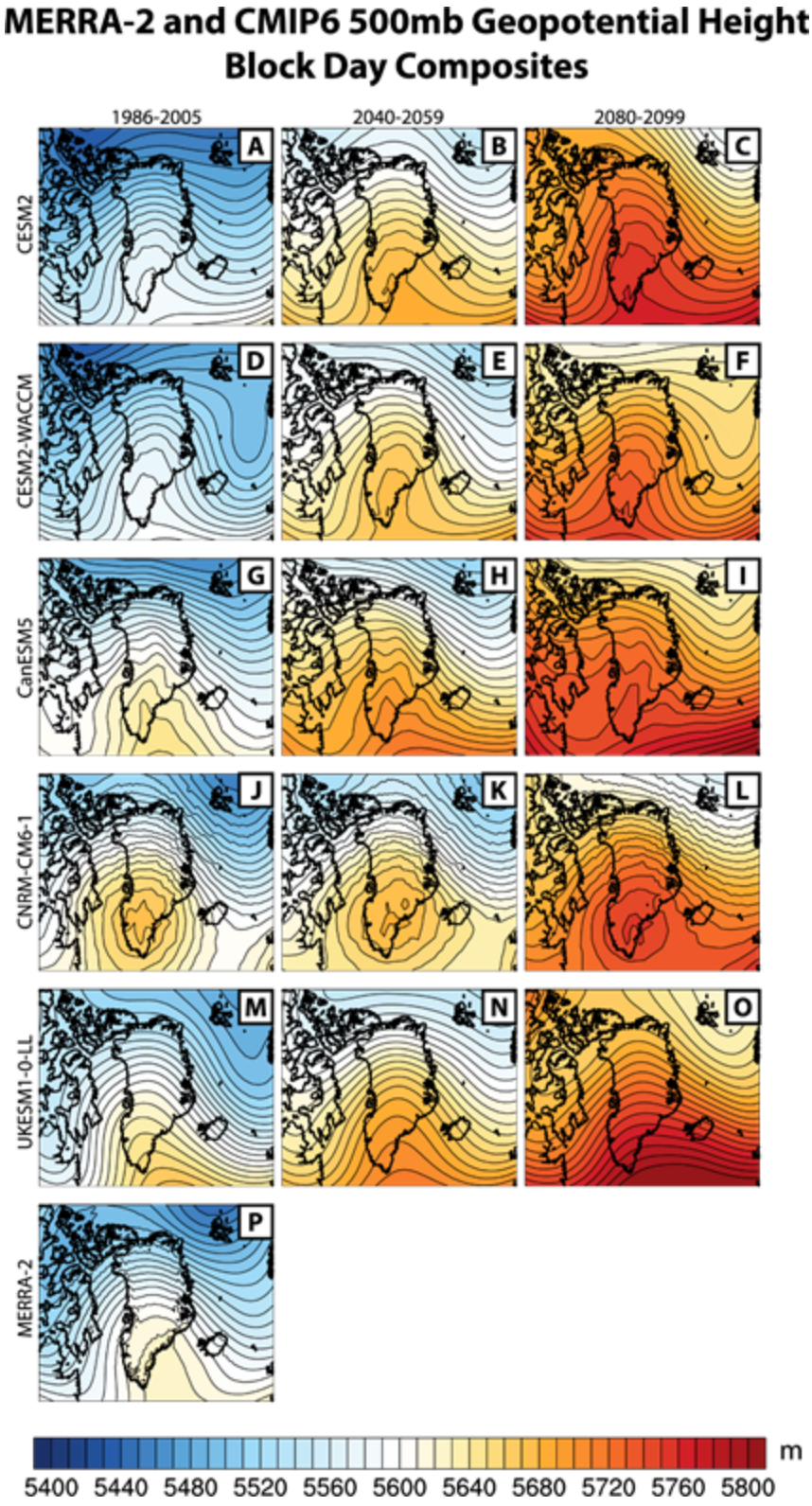

Fig. 4.2: Composite 500mb geopotential height maps for MERRA-2 and CMIP6 block days in the Historical, Mid-Century, and Late-Century time spans.

4.3.2 Surface Energy Fluxes

We examine changes in individual net surface energy flux (equation 4.1) anomaly components in order to better understand 1) how blocking affects radiative and turbulent energy fluxes, and 2) how these changes impact net surface energy flux anomalies over the Historical, Mid-Century, and Late-Century time periods. We will limit the discussion of component flux anomalies to those that are statistically significant over the GrIS.

4.3.2.1 Net Shortwave Fluxes

Net shortwave energy surface fluxes depend on the amount of downwelling shortwave radiation that transmits through the atmosphere and surface albedo. Because downwelling shortwave fluxes are highest in the summer, block days in late May or early September will exhibit smaller absolute flux magnitudes than block days in meteorological summer (i.e., June, July, and August). This trend exists between the CMIP6 models and time periods; absolute incident GrIS-average shortwave energy is significantly anticorrelated to the number of May/September days ($r = -0.60$) (Fig. 4.3).

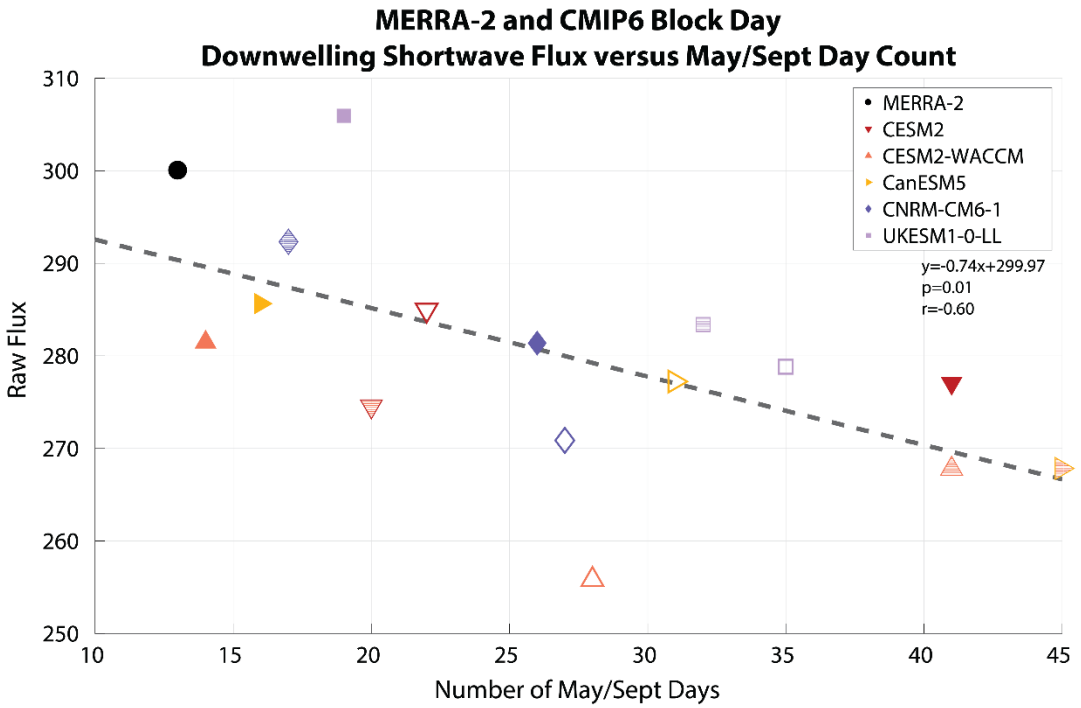

Fig. 4.3: Greenland-average downwelling shortwave flux with respect to the combined count of May and September Greenland block days for each time period. Historical average symbols are filled, Mid-Century (2040-2059) symbols are striped, and Late-Century (2080-2099) symbols are outlined.

Large May/September day counts decrease the expected net shortwave response to blocking because less downwelling shortwave energy reaches the surface. Because we do not account for downwelling shortwave flux seasonality, we recognize that our CMIP6 and MERRA-2 results are likely affected.

One of the main drivers behind surface energy change during historical Greenland blocking is the net shortwave flux response at the GrIS surface that results from cloud reduction (e.g. Mioduszewski et al., 2016; Lim et al., 2016; Hofer et al., 2017). Although MERRA-2 net shortwave anomalies are dominantly positive everywhere except northern Greenland, negative net shortwave energy changes are produced by blocking in the historical CMIP6 simulations (Fig. 4.4).

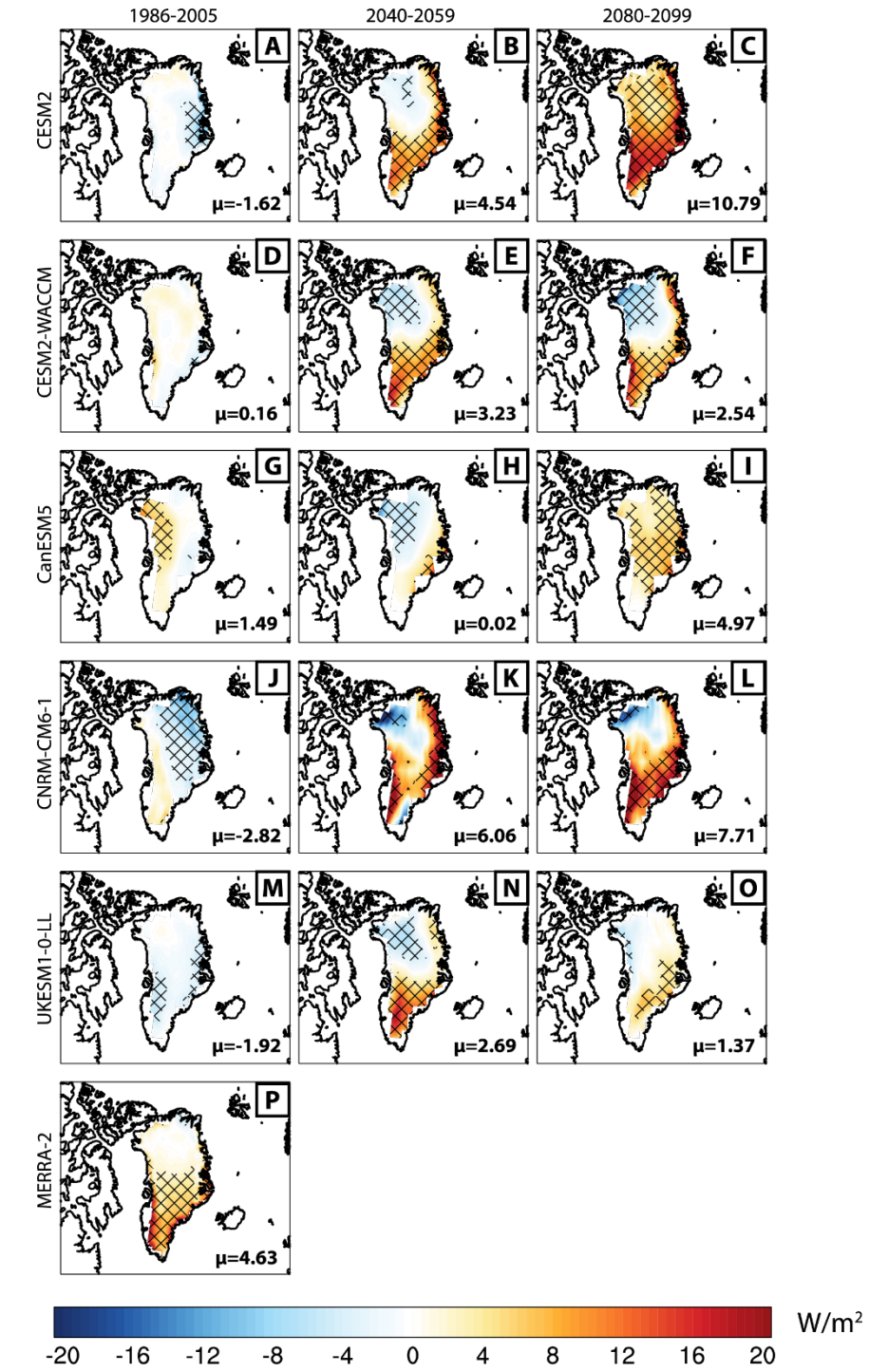

Fig. 4.4: Net shortwave energy flux blocking anomalies (relative to "Control" days) for MERRA-2 and Historical (1986-2005), Mid-Century (2040-2059), and Late-Century (2080-2099) CMIP6 model output. Cross-hatched areas are significant on a 95% confidence interval.

Net shortwave flux change patterns over Greenland also vary for each historical simulation, which suggests that the impacts of block circulation on cloud or surface albedo processes may be different between the models.

Mid-Century and Late-Century SSP585 simulations produce greater (i.e., more positive) net shortwave energy flux changes during block activity. We find more consistent net shortwave anomaly patterns in the Mid-Century simulations; increased (decreased) fluxes occur over southern (northern) Greenland (Fig. 4.4). 500mb geopotential height patterns (Fig. 4.2) indicate regional subsidence and cloud reduction is collocated with composite block centers over southern Greenland (e.g., Rajecwicz and Marshall, 2014; Hofer et al., 2017). Over northern Greenland, negative net shortwave flux anomalies likely result from onshore airflow that moves over the GrIS surface and cools adiabatically to increase cloud cover and reduce available incident shortwave energy (Mioduszewski et al., 2016; Hofer et al, 2017; Delhasse et al., 2018).

As we see with Historical blocking, Late-Century net shortwave flux anomaly patterns are markedly different between the models. Some (CESM and CanESM) solely produce positive anomalies that likely result from aggressive cloud reductions, while the others maintain the positive-to-negative changes from southern to northern Greenland that we observe in Mid-Century output. UKESM alone produces smaller GrIS-wide net shortwave flux anomalies in Late-Century when compared to Mid-Century. In this case, we hypothesize that atmospheric warming and enhanced moisture content are responsible for increased cloud production over sub-areas of the GrIS, despite subsiding airflow produced during blocking (Bennartz et al., 2013; Franco et al., 2013).

To better understand the mechanisms behind net shortwave flux anomalies, we examine the corresponding surface albedo and downwelling shortwave flux anomalies (Figs. 4.5 and 4.6).

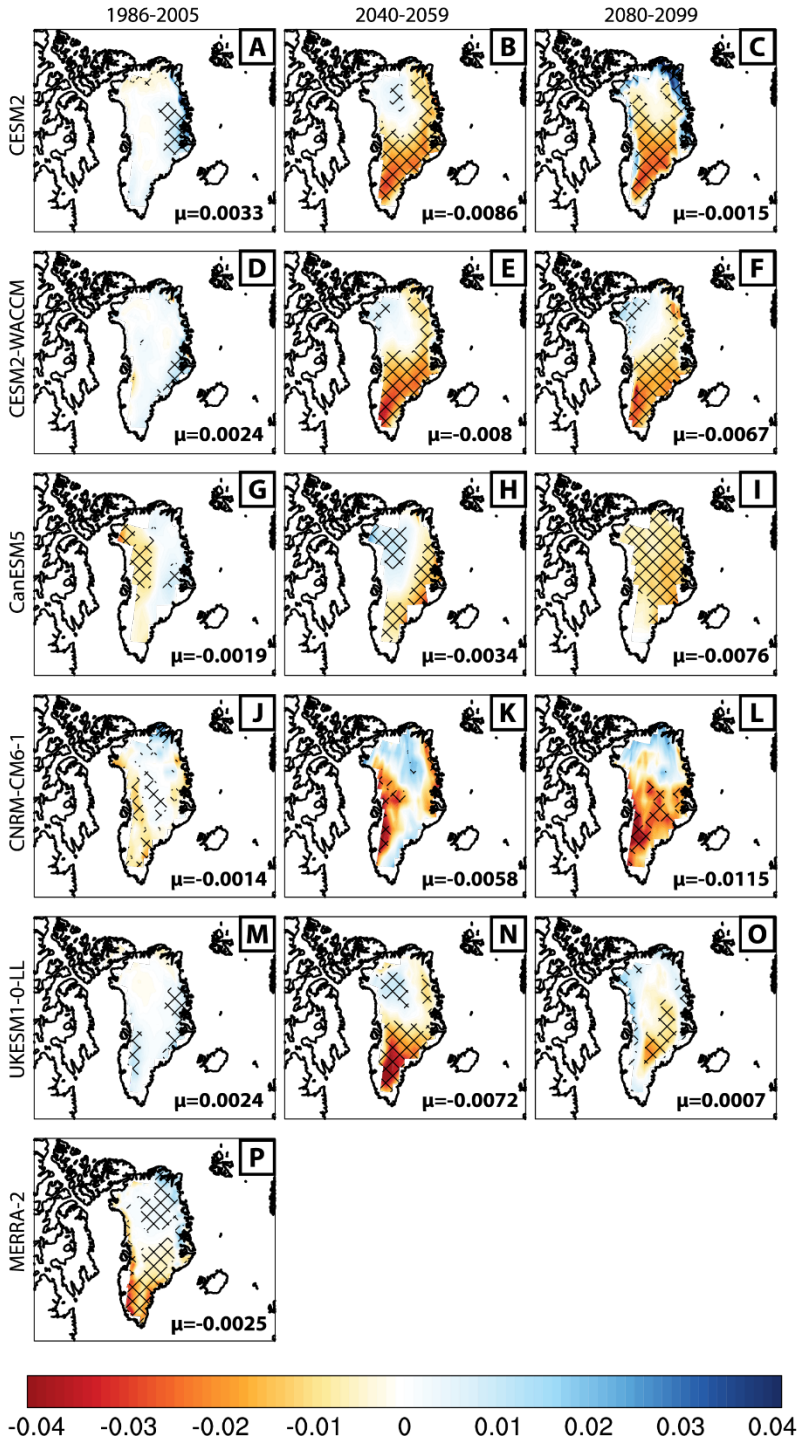

Fig. 4.5: Same as Fig. 4.4, but for surface albedo anomalies.

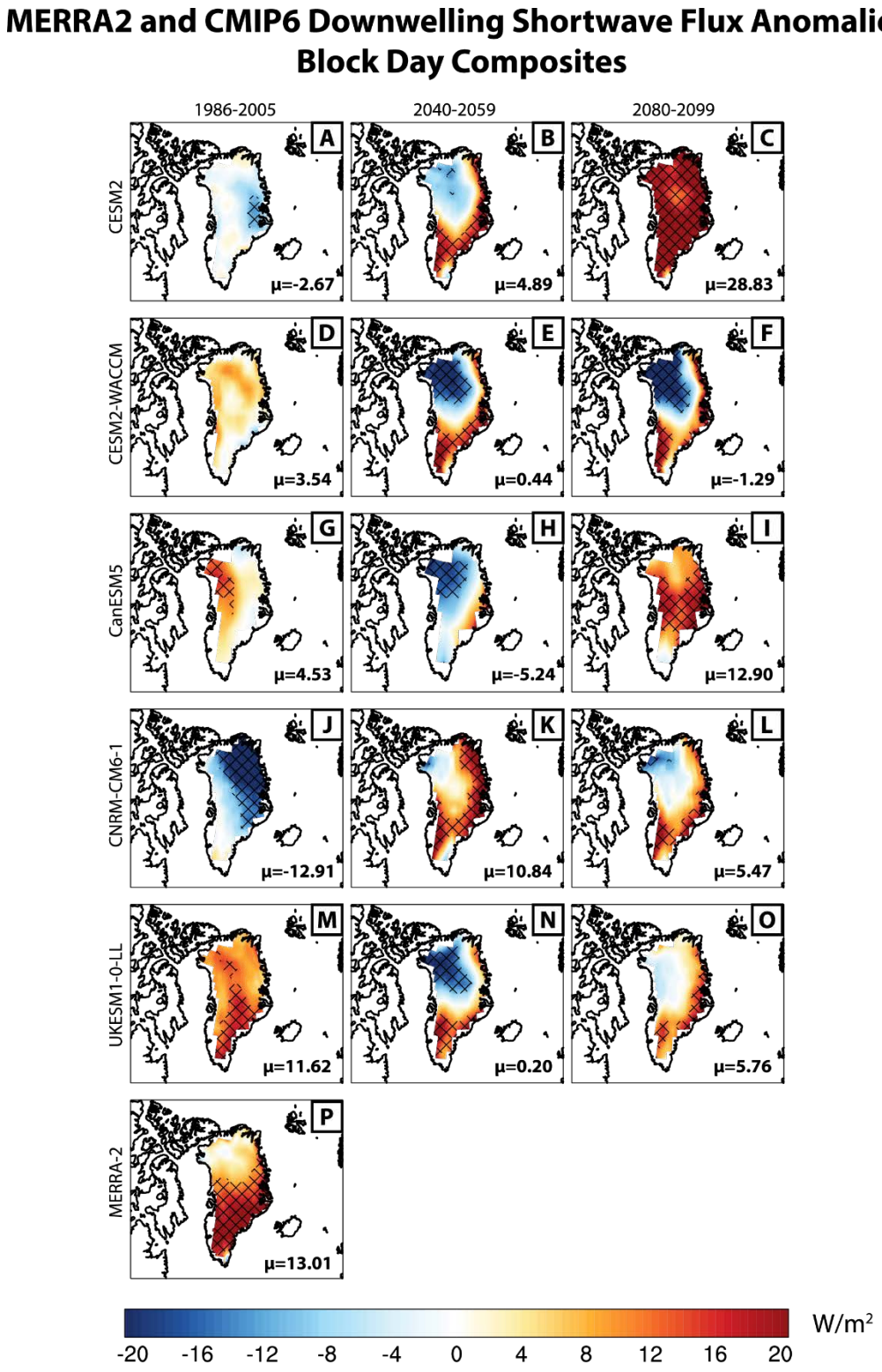

Fig. 4.6: Same as Fig. 4.4, but for downwelling shortwave flux anomalies.

Overall, larger downwelling shortwave flux changes during blocking correspond to larger net shortwave fluxes and decreased surface albedos, regardless of time period. A notable exception is Historical UKESM blocking, which produces negative net shortwave flux changes that correspond to greater surface albedo despite enhanced downwelling shortwave fluxes (Figs. 4.4M, 4.5M, and 4.6M). This suggests that UKESM model surface albedo changes are less sensitive to downwelling shortwave flux perturbations than other models. This could be especially important during late May block days since GrIS albedo is greatest in the spring months (Box et al., 2012).

We find that all historical CMIP6 models underestimate GrIS-average net shortwave changes with respect to MERRA-2 (Fig. 4.7):

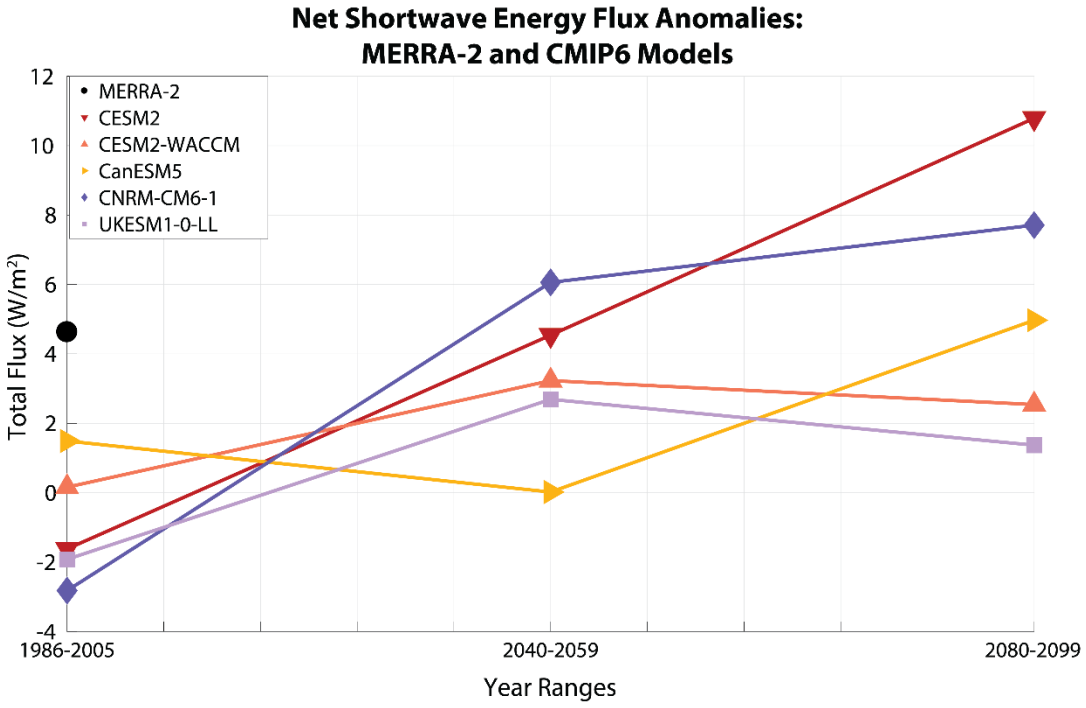

Fig. 4.7: Greenland-average net shortwave anomalies for blocking in the historical (1986-2005), Mid-Century (2040-2059), and Late-Century (2080-2099) time periods.

Because MERRA-2 produces the lowest May/September block day count (Fig. 4.3), this negative bias in net shortwave flux anomalies could partly result from downwelling shortwave seasonality biases produced by CMIP6 greater Historical May/September block day counts. However, since CMIP6 Historical May/September block day counts are lower than the corresponding day counts in Mid- and Late-Century blocking (Fig. 4.3; CESM is an exception), CMIP6 model energy flux parameterizations could struggle to correctly produce expected net shortwave flux anomalies. In this case, it is plausible that the positive Greenland-average Mid-Century and Late-Century net shortwave flux anomalies should be larger. Regardless, we observe larger Greenland-wide net shortwave flux responses to Mid-Century and Late-Century blocking. We also find that the spread in GrIS-average net shortwave flux anomalies (along the y-axis in Fig. 4.7) in each time period is quite high. Although larger and variable future net shortwave flux anomalies could be produced by changes in block dynamics in individual models, we conclude that enhanced shortwave absorption at the surface results from lower (and highly variable) GrIS absolute albedo in future simulations (not shown).

4.3.2.2 Net Longwave Fluxes

Unlike net shortwave energy responses, net longwave flux anomalies produced by blocking depend on decreased cloud coverage and warm air advection, both of which have offsetting effects (i.e., Shupe and Intrieri, 2004; Hofer et al., 2017). Across all time periods and models, we find that negative (positive) net shortwave flux anomalies correspond to positive (negative) net longwave flux anomalies (Fig. 4.8).

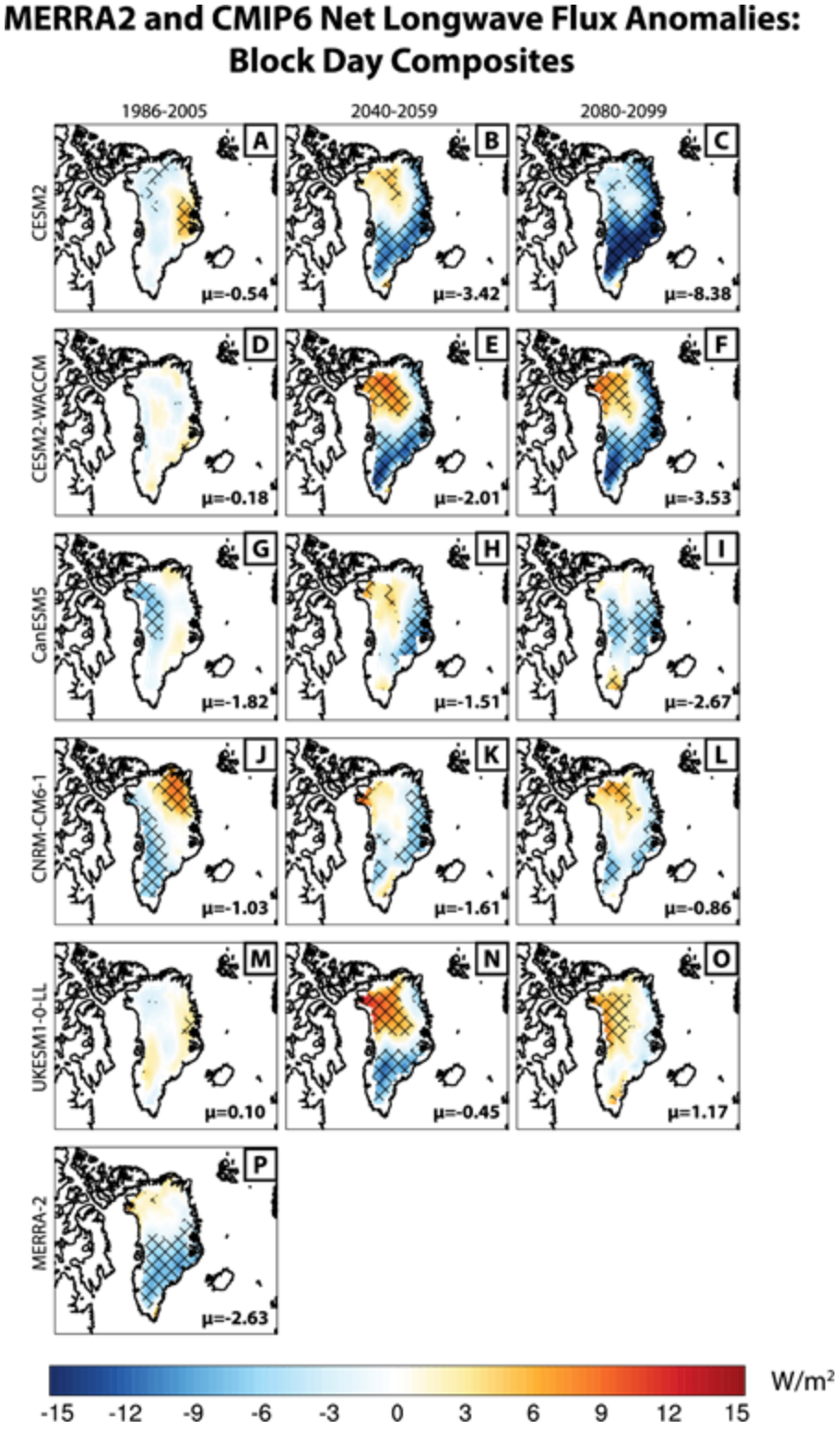

Fig. 4.8: Same as Fig. 4.4, but for net longwave flux anomalies.

We hypothesize negative correlations in net shortwave and net longwave flux anomalies result from cloud changes produced by the models. In areas where blocking reduces cloud cover, downwelling fluxes decrease because terrestrial longwave energy transmits through the atmosphere (Franco et al., 2013; Fausto et al., 2016) while minimal upwelling longwave flux changes occur because the GrIS surface temperature is restricted by melting point of water (e.g., Lenaerts et al., 2019). We will confirm this by examining corresponding CMIP6 cloud data.

Greenland-wide net longwave flux anomalies are negative in MERRA-2 and CMIP6 models except UKESM Historical and Late-Century simulations. UKESM Late-Century blocking increases net longwave flux by $+1.17\ W/m^2$ (Fig. 4.9). This provides further evidence that UKESM produces more regional atmospheric moisture than other CMIP6 Late-Century simulations.

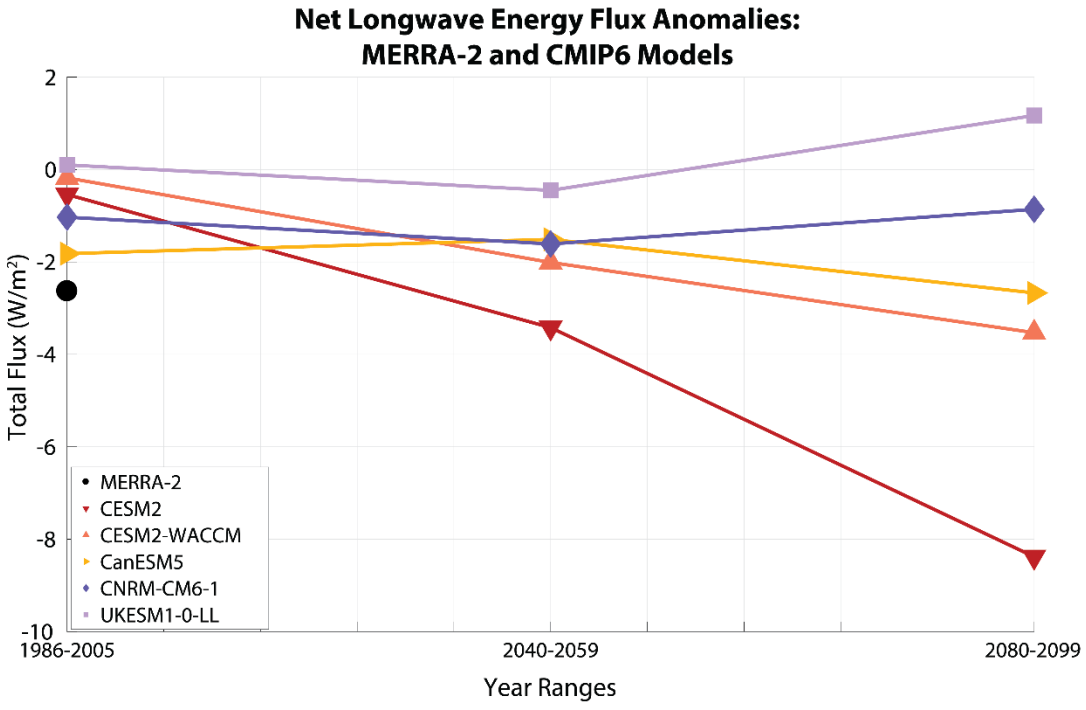

Fig. 4.9: Same as Fig. 4.7, but for Greenland-average net longwave flux anomalies.

Similar to net shortwave fluxes, the Greenland-average MERRA-2 net longwave flux change has a larger magnitude (i.e., more negative) than all Historical CMIP6 net longwave flux anomalies. CMIP6 models also struggle to agree on future net longwave flux changes to Greenland blocking in Late Century (Fig. 4.8), indicating that longwave energy responses to blocking are very uncertain in the future.

GrIS-average net longwave flux anomaly magnitudes tend to be smaller than the corresponding net shortwave flux anomalies in all models except WACCM and CanESM (Fig. 4.9). This indicates that net shortwave flux changes contribute more to GrIS surface energy processes than net longwave fluxes during Greenland blocking, which has been found in previous studies (e.g., Hofer et al., 2017; Lim et al., 2016; Mioduszewski et al., 2016).

As we see with net shortwave fluxes, net longwave flux anomalies vary greatly between models and time periods. We hypothesize that net longwave flux anomaly patterns are roughly anticorrelated with net shortwave flux anomalies because of blocking-produced cloud changes. Net longwave flux changes become more variable in the future simulations and are thus highly uncertain. Overall, net shortwave flux anomalies generally outweigh net longwave flux anomalies in most simulations.

4.3.2.3 Sensible Heat Fluxes

Our work in Chapter 3 also demonstrates that sensible heating is an important contributor to net surface energy changes during blocking, especially over western Greenland where warm, moist air from the North Atlantic is transported over the GrIS (Franco et al., 2013; Fausto et al., 2016). Regardless of time period, we find that most blocking cases produce positive changes in sensible heat flux over areas of the GrIS (Fig. 4.10).

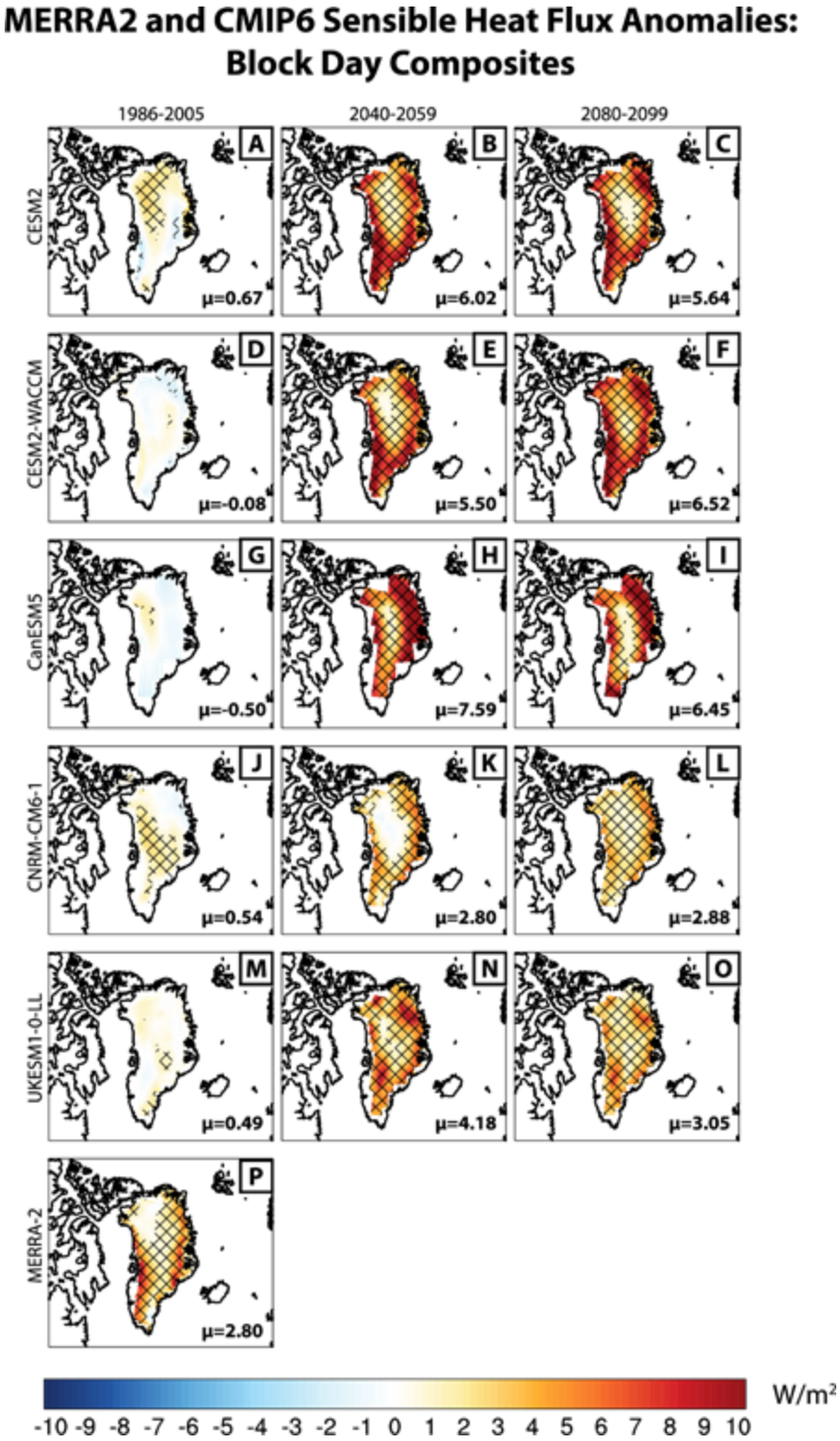

Fig. 4.10: Same as Fig. 4.4, but for sensible heat flux anomalies.

Only Historical simulations produce areas of negative sensible heat flux anomalies (i.e., directed outward from the GrIS surface). Because GrIS surface warming is limited by the melting point of frozen water (e.g., Lenaerts et al., 2019) and blocking warms the lower atmosphere (Fettweis et al., 2011, 2013; Hofer et al., 2017), negative sensible heat flux anomalies in Historical CMIP6 simulations indicate subdued warm air advection over the GrIS. This could arise for a variety of reasons, including low Greenland blocking wind speeds or imported air mass temperature characteristics. As we see with net radiative flux anomalies, MERRA-2 sensible heat flux changes are greater over the GrIS. MERRA-2 produces positive sensible heat anomalies everywhere except a small region in north-central Greenland and more accurately depict atmospheric warming produced by blocking activity. Overall, Greenland-averaged MERRA-2 sensible heat flux change is more than 2 W/m^2 greater than any of the CMIP6 output (Fig. 4.11).

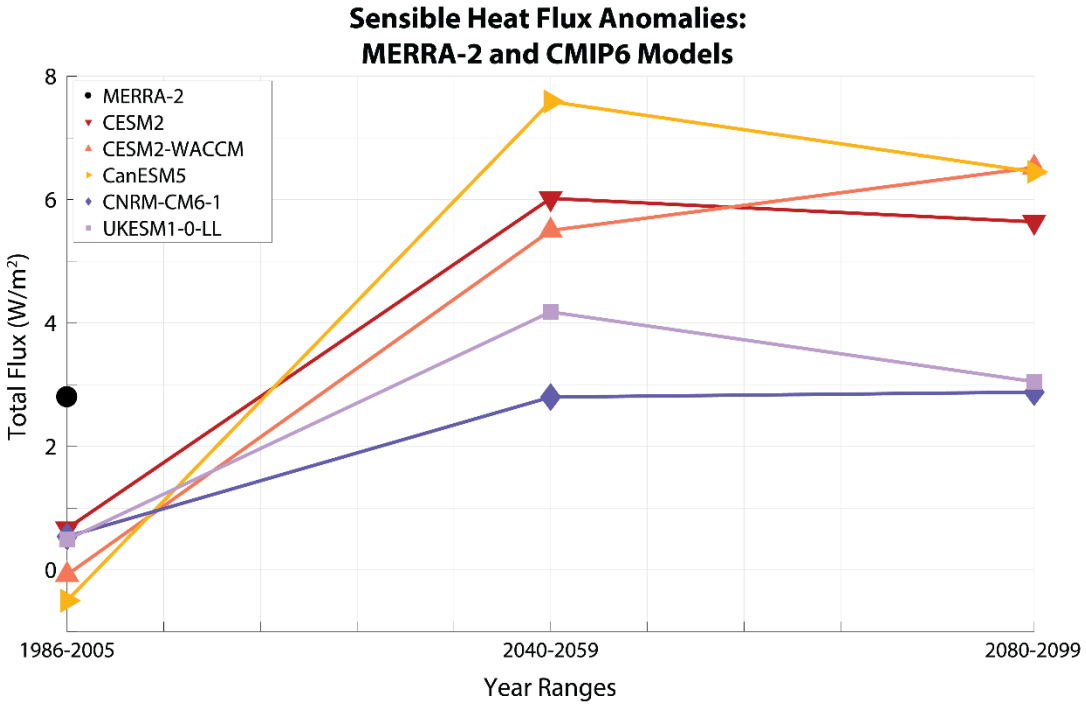

Fig. 4.11: Same as Fig. 4.7, for sensible heat flux.

Mid-Century and Late-Century sensible heat flux anomalies are similar in magnitude (Figs. 4.10, 4.11) and are larger than Historical anomalies for each CMIP6 model. Anomalies decrease at higher altitudes (i.e., the central GrIS) because airflow cools adiabatically as it moves upslope. Future sensible heat changes likely result from increased atmospheric temperature produced by warm air advection during blocking (van den Broeke et al., 2011). 500mb geopotential height patterns and pressure gradient patterns are similar between all time periods (Fig. 4.2), which suggests that sensible heat changes might not be caused by wind speed anomalies.

4.3.2.4 Latent Heat Fluxes

Latent heat flux anomalies can result from a combination of specific humidity, wind, or precipitation responses to blocking. Like the other energy flux anomalies, we find that latent heat flux anomalies are more positive for future Greenland blocking. Historical CMIP6 simulations produce positive and negative anomalies over the GrIS, with Greenland-average changes ranging from $-0.81\ W/m^2$ for CanESM to $+0.33\ W/m^2$ for CESM (Fig. 4.12 and Fig. 4.13; next page). Anomaly patterns over the GrIS also vary between the CMIP6 models. As we see with MERRA-2, only CanESM is able to replicate positive latent heat flux changes over central Greenland and negative anomalies over the GrIS margins (Fig. 4.12J). Unlike GrIS-average radiative and sensible heat flux anomalies, CMIP6 historical simulations do not appear to produce any bias in latent heat responses to blocking.

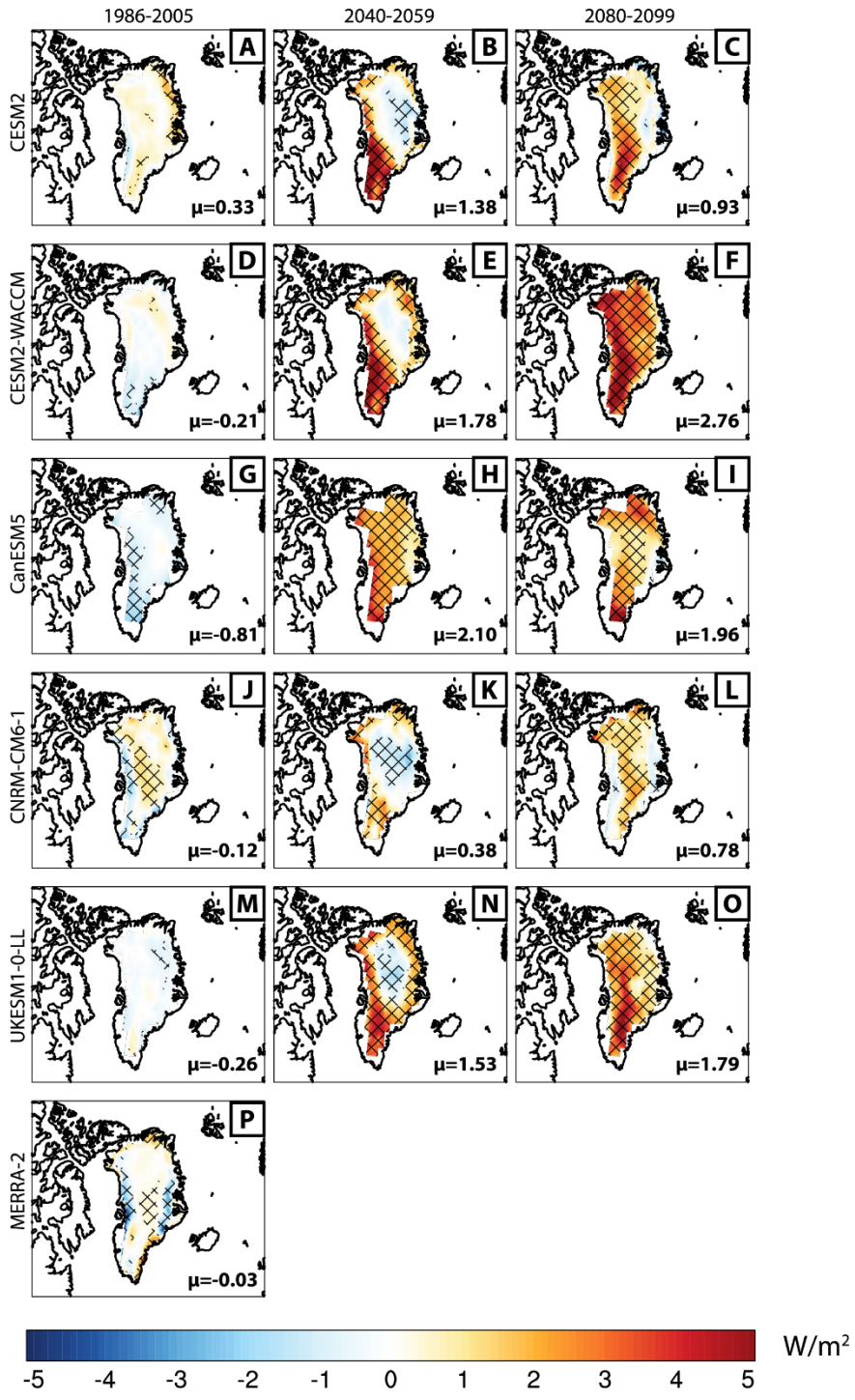

Fig. 4.12: Same as Fig. 4.4, but for latent heat flux anomalies.

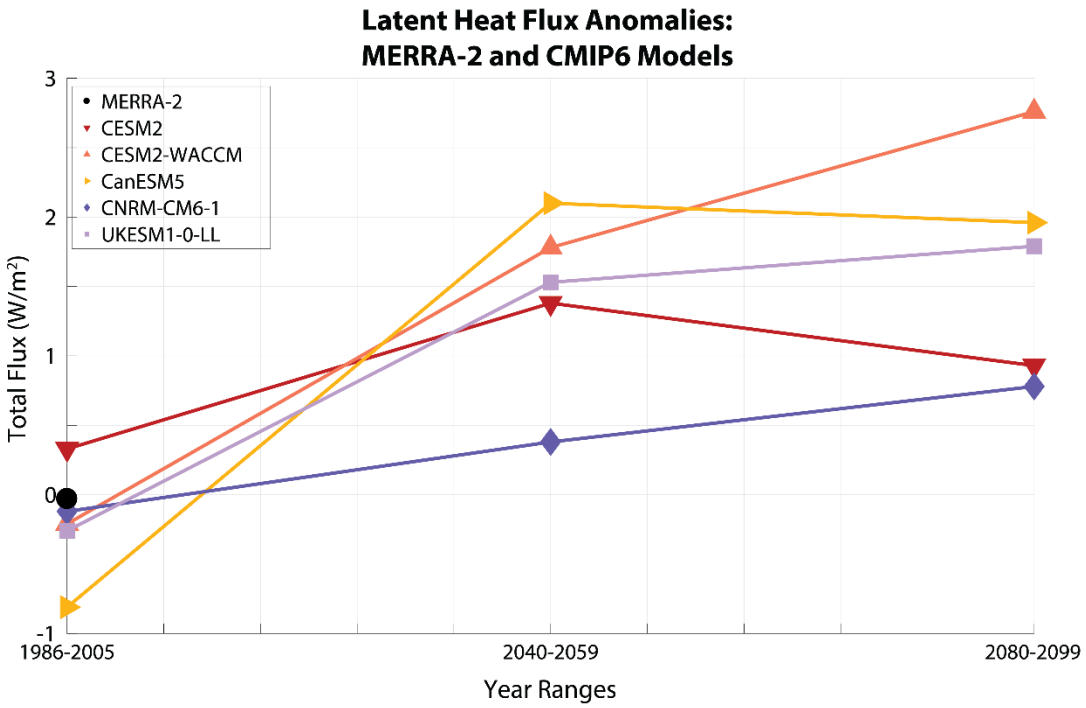

Fig. 4.13: Same as Fig. 4.7, but for spatially-averaged latent heat flux anomalies.

All Mid-Century CMIP6 models except CanESM produce positive (negative) latent heat anomalies over the GrIS margins (central GrIS). Southerly warm, moist airflow from the North Atlantic moves over the GrIS margins and condenses to transfer additional latent heat to the GrIS surface (Tedesco and Fettweis, 2012). Over central Greenland, the orographic airflow that contributed to GrIS marginal positive anomalies is less moist than the surface and produces negative latent heat anomalies. In contrast, all Late-Century simulations produce positive latent heat flux anomalies over central Greenland. This could arise from GrIS surface elevation changes (i.e., Hakuba et al., 2012) or warmer airflow compared to Mid-Century simulations. Overall, Greenland-averaged Mid-Century and Late-Century latent heat flux changes are similar.

4.3.2.5 Net Surface Energy Fluxes

Greenland blocking has been cited as one of the main contributors to observed summertime negative surface mass balance changes through increasing energy input (Mioduszewski et al., 2016; Hofer et al., 2017; Delhasse et al., 2018). Surprisingly, historical CMIP6 net surface energy flux anomalies do not exhibit positive energy contributions (Fig. 4.14). This contradicts MERRA-2 net surface energy flux anomalies, which are positive over all but the highest GrIS elevations. We find that CMIP6 spatially-averaged anomalies are too low for all CMIP6 models (Fig. 4.15), which is not surprising given the aforementioned net shortwave, net longwave, and sensible heat flux anomaly biases. Greenland-average net energy change during MERRA-2 blocking is at least 4 W/m^2 larger than all of the other CMIP6 models. Since Greenland blocking is supposed to enhance net surface energy, negative net surface energy changes could negate or even reverse expected GrIS snowmelt rates.

In Mid-Century and Late-Century, net surface energy flux anomalies are positive. Apart from CNRM, all models produce positive net energy changes over all of the GrIS during future blocking. CNRM produces small areas of negative net energy flux anomalies over northwestern Greenland because of large negative net shortwave flux changes (see Fig. 4.4). GrIS-wide net energy anomalies are similar between Mid-Century and Late-Century (Fig. 4.15), with less variability between models in Mid-Century (net energy flux anomaly range: $+7.64\ W/m^2$ to $+8.52\ W/m^2$) than Late-Century ($+7.38\ W/m^2$ to $+10.71\ W/m^2$).

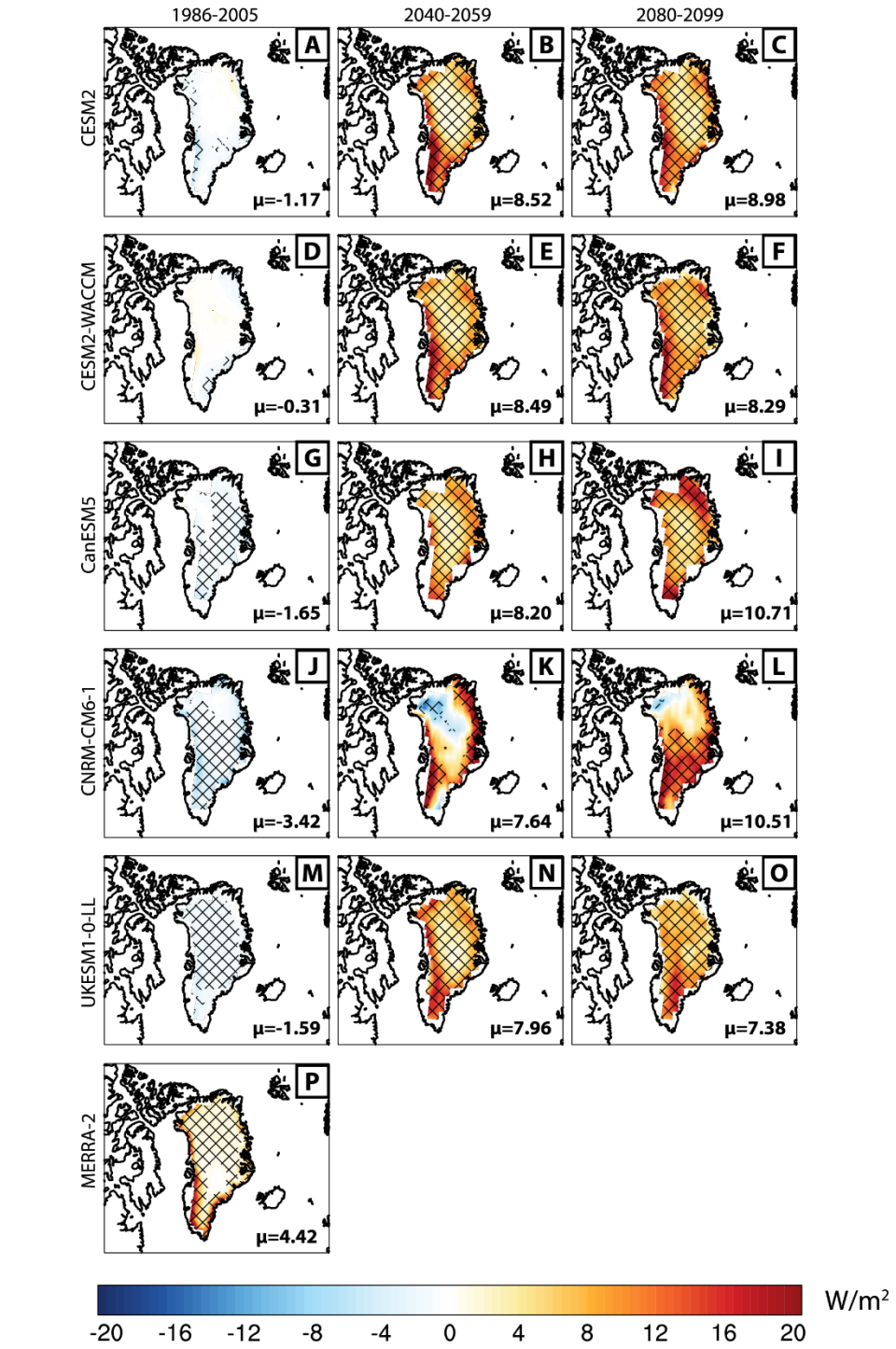

Fig. 4.14: Same as Fig. 4.4, but for net surface energy flux anomalies.

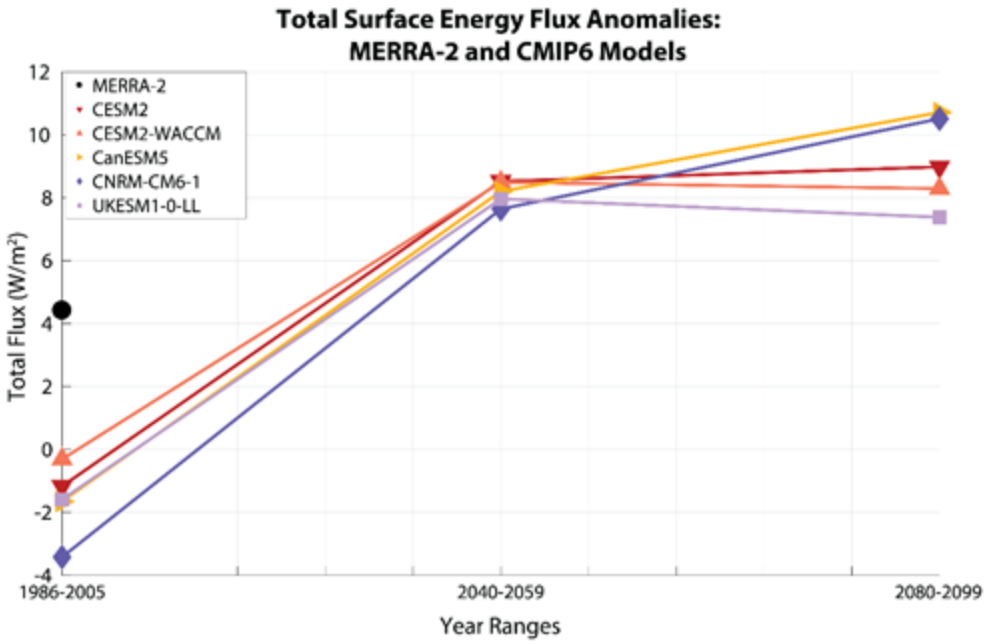

Fig. 4.15: Same as Fig. 4.7, but for Greenland-average net energy flux anomalies.

Between all three time periods, we examine the relative contributions of radiative and non-radiative flux changes to net surface energy anomalies produced by blocking (Table 4.3).

Table 4.3: Percent Contribution of Component Energy Anomalies to Net Surface Energy Anomalies. Highest percentages for each case are highlighted in yellow.

Model	Simulation	SW_{net}	LW_{net}	SH	LH
CESM	Historical	51.3	17.1	21.2	10.4
	Mid-Century	29.3	22.1	38.9	8.9
	Late-Century	41.9	32.6	21.9	3.6
WACCM	Historical	25.4	28.6	12.7	33.3
	Mid-Century	25.8	16.1	43.9	14.2
	Late-Century	16.5	23.0	42.3	18.0
CanESM	Historical	32.3	39.4	10.8	17.5
	Mid-Century	0.2	13.5	67.6	18.7
	Late-Century	31.0	16.6	40.2	12.2
CNRM	Historical	62.5	22.8	12.0	2.7
	Mid-Century	55.9	14.8	25.8	3.5
	Late-Century	63.0	7.0	23.5	6.4
UKESM	Historical	69.3	3.6	17.7	9.4
	Mid-Century	30.4	5.1	47.2	17.3
	Late-Century	18.6	15.9	41.3	24.3
MERRA-2	Historical	45.9	26.1	27.8	0.3

In agreement with previous studies (e.g., Fausto et al., 2016; Hofer et al., 2017), we find that net shortwave and sensible heat flux anomalies are the largest contributors over all models and time periods (~41% of all cases for both flux varieties). Net longwave and latent heat anomalies are the largest contributors to net surface energy change during Historical CanESM and Historical WACCM blocking, respectively.

When we separate Historical, Mid-Century, and Late-Century simulations, we find that important contributing flux changes vary over time. 3 out of 5 Historical CMIP6 simulations produce the largest energy contributions from net shortwave anomalies. Sensible heating anomalies become more important contributors in Mid-Century (4 of the simulations) and Late-Century (3 of the simulations). Per these simulations, future surface energy changes that result from blocking will be more sensitive to sensible heating via warm air advection than net shortwave flux changes caused by subsidence, surface albedo change, or downwelling shortwave flux changes.

Averaging CMIP6 Greenland-wide energy flux anomalies provides an ensemble view of how blocking will impact surface energy processes in the future (Table 4.4).

Table 4.4: CMIP6-Average Flux Anomalies for each Time Period (W/m^2)

Simulation	SW_{net}	LW_{net}	SH	LH	E_{Total}
Historical	-0.94	-0.69	0.22	-0.21	-1.63
Mid-Century	3.31	-1.80	5.22	1.43	8.17
Late-Century	5.48	-2.85	4.91	1.64	9.17

Historical blocking produces negative contributions to total surface energy for all except sensible heat fluxes, most likely caused by warm air advection. Both Mid- and Late-Century averages produce positive flux anomalies for all except net longwave energy, which serves as a surface energy sink (e.g., van den Broeke et al., 2011). Although Mid-Century sensible heat changes outweigh net shortwave flux changes, Late-Century net shortwave flux anomalies are slightly

higher than sensible heat anomalies. This can be partly attributed to notably high CESM net shortwave responses to blocking activity in Late Century. It is worth noting that all Late-Century Greenland-wide component energy anomalies are more variable than their Mid-Century counterparts, so this transition back to dominant net shortwave flux changes is uncertain.

Greenland blocking-induced net surface energy changes increase between the Historical and future CMIP6 simulations. Historical blocking produces negative net surface energy changes that contradict the positive anomalies we calculate for MERRA-2 because of biases in CMIP6 net shortwave, net longwave, and sensible heat flux anomalies. This potential negative bias in Historical simulations indicates that the Mid-Century and Late-Century surface energy flux anomalies might be larger than those produced by the SSP585 simulations. Although net shortwave and sensible heat flux anomalies are the largest overall contributors to surface energy flux changes, we find that sensible heat flux anomalies become more influential during future blocking activity. This suggests that warm air transport over the GrIS could become more important than cloud reduction during future Greenland blocking episodes for Greenland-wide snowmelt acceleration.

4.4 Conclusion

In this study, we use CMIP6 model data and MERRA-2 reanalysis data to understand GrIS surface energy flux responses to summer Greenland blocking activity over historical (1986-2005) and future (2040-2059; 2080-2099) time periods in the SSP585 climate change scenario. We use the GBI2 technique (Hanna et al., 2018b) to detect Greenland block days for each dataset. June, July, and August non-block days serve as the control, which we subtract from

block days to find anomaly fields. MERRA-2 block and flux anomalies are used to validate CMIP6 historical data and to explain biases in future CMIP6 simulations.

Greenland blocking frequencies do not show any trends within each time period. In addition, average seasonal block day counts are similar between all time periods. Despite increased summertime Greenland blocking frequency over the past 20 years (Fettweis et al., 2011, 2013; Hanna et al., 2014), we do not find any significant trends in MERRA-2 or CMIP6 block frequencies because we use an earlier time period (1986-2005). Although we do not find any significant changes in GBI2 between the historical and future time spans, GBI1 (i.e., spatially-averaged 500mb geopotential height over Greenland) increases with time. Average 500mb geopotential height patterns depict atmospheric ridging, regardless of time period.

Individual CMIP6 net energy flux anomalies are highly variable between each model. Anomaly patterns over the GrIS are also different for each model, which suggests inconsistencies in CMIP6 blocking representation. CMIP6 historical net shortwave, net longwave, and sensible heat flux anomalies disagree with the corresponding MERRA-2 anomalies. Block-caused net shortwave and sensible heat flux changes in CMIP6 are at least 2 W/m^2 lower than the corresponding MERRA-2 anomalies, while all CMIP6 net longwave flux anomalies are up to 2 W/m^2 larger than MERRA-2. These biases produce MERRA-2 total surface energy flux anomaly differences that are over 4 W/m^2 greater than CMIP6, which suggests that CMIP6 historical models struggle to reproduce surface energy change conditions during Greenland blocking. Assuming model processes are consistent between historical and future simulations, the resulting energy flux anomalies we find in the SSP585 simulations could be too low.

Mid-Century and Late-Century Greenland blocking produce different energy anomalies than Historical models. Net shortwave, sensible heat, and latent heat anomalies all increase in the

SSP585 simulations, while net longwave fluxes marginally decrease. We also find more consistent energy anomalies between models during Mid-Century blocking. Net shortwave flux changes are positive over southern Greenland because of subsidence and reduced cloud cover, while net shortwave energy decreases over northern Greenland because of upslope airflow produced by block circulation. The opposite is the case for net longwave fluxes because of the impact of clouds on downwelling longwave energy. Sensible and latent heat fluxes increase over most of the GrIS as a result of enhanced transport of warm, moist air by blocks over the GrIS in future simulations. As a result, net surface energy increases uniformly over the GrIS during blocking for almost all models. Although these patterns and magnitude changes are similar in Late-Century, there is less agreement between models and more uncertainty in the results that introduces uncertainty in our interpretations.

In 13 out of 15 CMIP6 simulations, net shortwave or sensible heat flux anomalies are the largest contributors to net surface energy changes (positive or negative), with Historical simulations comprising the two exceptions. Sensible heat flux anomalies increase net surface energy during blocking to a greater extent in Mid-Century and Late-Century simulations, which suggests that airflow processes and turbulent heat exchange with the surface during blocking will be more influential on surface energy than changes in radiative energy. Latent heat flux contributes more to surface energy during Mid-Century and Late-Century blocking because of enhanced air temperature and moisture content, but these anomalies are smaller than sensible heat flux changes.

This study provides unique insight into the mechanisms through which Greenland blocking affects surface energy, and how these mechanisms will change in the future. We use 5 CMIP6 models to study these changes over daily time scales, but ensemble studies ideally

include more model data. As the CMIP6 database continues to populate, we will add more models that produce daily 500mb geopotential height and surface energy flux fields to gain a better idea of average simulated Greenland blocking conditions. We also limit our analysis to surface energy fluxes without analyzing meteorological conditions like cloud fraction, air temperature, winds, and moisture availability. Adding these fields to the analysis will provide a clearer understanding of how the surface energy fluxes are changing.

Atmosphere-surface interactions will evolve in the future. Greenland blocking is projected to increase energy input into the GrIS. CMIP6 models forecast sensible heat anomalies as the main component of GrIS net energy change while net shortwave flux changes become less influential on surface processes. Based on these results, Greenland blocking will still be an important contributor to net surface energy increase and greater GrIS snowmelt.

Chapter 5: Conclusions and Future Work

5.1 Summary of Findings

Greenland Ice Sheet (GrIS) surface melt has become increasingly important to total GrIS mass loss. Because the GrIS is the largest reservoir of frozen water in the northern hemisphere, it is important that we understand the causes behind its surface melt to better predict how global sea level will rise. Complete GrIS melt would increase global sea level by over 7 meters (i.e., Gregory et al., 2004; Church et al., 2013), which would have major consequences for society, especially those who live close to Earth's oceans.

There are many surface melt triggers that vary in duration and spatial coverage over the GrIS. The spatial variability in melt pattern responses to these triggers arises from surface albedo, temperature, and circulation responses to GrIS topography. GrIS surface albedo increases with elevation because of atmospheric adiabatic cooling and lower melt frequency. In contrast, the GrIS margins are characterized by aged snow and exposed ice and are thus less reflective. Airflow that moves onto the ice sheet is forced aloft by the GrIS margins and often induces orographic precipitation and cloud formation processes.

Although there are many short-term (i.e., days to weeks in duration) processes responsible for GrIS snowmelt and surface energy changes, we focus on the impacts of atmospheric and in-snow light-absorbing aerosols (Chapter 2), how changing block location impacts clouds and surface energy fluxes (Chapter 3), and how future blocking will contribute to GrIS surface energy flux changes in the shared socioeconomic pathway (SSP) 5 and representation concentration pathway (RCP) 8.5 scenarios (Chapter 4).

In Chapter 2, we explored the following science question: *How do biomass burning-produced light-absorbing aerosols in the atmosphere and in the GrIS snow impact snowmelt and surface energy processes?* We modified the Community Earth System Model (CESM) to assign consistent, specific light-absorbing aerosol burdens in the atmosphere, in the GrIS, and in both locations simultaneously. For each case, we ran five separate global climate model simulations with different aerosol amounts to test the Greenland response to these changing burdens, some of which were unrealistically high. We also tested how changing atmospheric aerosol single-scatter albedo affected surface processes. GrIS snowmelt anomalies cases with atmospheric light-absorbing aerosols were insignificant because of the offsetting impacts of shortwave flux dimming and tropospheric warming. Although the same is true for single-scatter albedo modification, we did find that lower single-scatter albedos produced larger areas of positive melt change. Regardless of atmospheric aerosol presence, in-snow BC and dust combined mass mixing ratios exceeding 58.8 ng/g produced significant melt over the GrIS. Snowmelt and net surface energy flux responses to increasing aerosol burdens were similar for each aerosol placement scenario. However, atmospheric and in-snow aerosols influenced radiative and non-radiative fluxes differently. In-snow aerosols impacted net shortwave fluxes through surface albedo reduction and also corresponded to the largest net energy changes. Although atmospheric

aerosols were responsible for the largest sensible and latent heat flux changes because of lower tropospheric warming, these anomalies were smaller than in-snow net shortwave energy changes. From this study, we concluded that knowledge of simultaneous atmospheric and in-snow aerosol presence is necessary to best understand how light-absorbing BC and dust impact Greenland's climate.

The focus of Chapter 3 and the data we used were markedly different from Chapter 2. We used a combination of MODIS cloud data and MERRA-2 meteorological and surface energy data to answer: *How does Greenland block location affect cloud and surface energy flux patterns?* We found that blocks over northern Greenland reduce average cloud cover roughly 4 times more than blocks over southern Greenland. These differences in cloud changes also impact net cloud radiative forcing at the GrIS; shortwave (longwave) cloud radiative forcing is more positive (negative) during northern Greenland blocking than southern Greenland blocking. Out of all block locations, northwest (NW) block days produce the lowest average change in net surface energy over the entire GrIS. Although NW blocking reduces cloud coverage and increases net shortwave energy, longwave energy escapes and turbulent heat flux changes are negligible. NW block days alone produce significantly negative net surface energy changes over the accumulation zone snow. We also determined that eastern Greenland block days exhibited higher net surface energy changes than their corresponding western Greenland block days because of enhanced sensible heating produced by warm air advection onto the southern GrIS. Overall, we concluded that Greenland block location impacts the spatial distribution of cloud and energy changes and can lead to different Greenland-average responses.

We continued to examine the role of blocking on GrIS surface energy fluxes in Chapter 4. The questions we asked were the following: *How will future Greenland blocking affect*

radiative, non-radiative, and total surface energy fluxes in the greatest warming scenario (SSP585)? How do these changes compare to historical trends? To answer these questions, we used daily CMIP6 500mb geopotential height and surface energy flux fields from five models. We used MERRA-2 data over the same time to benchmark CMIP6 surface energy flux anomalies. With the exception of latent heat flux anomalies, historical CMIP6 fluxes were biased relative to MERRA-2 and produced negative net surface energy changes during blocking. However, Greenland blocking in the future time periods produced positive net surface energy changes over most of the GrIS in all models. These corresponded to dominantly positive sensible heat flux anomalies and mostly increased net shortwave fluxes. For all models and time periods, net shortwave and sensible heat flux anomalies are the largest contributors to net surface energy changes. However, we found that sensible heat flux changes are likely to become more important because of enhanced atmospheric warming. These results suggest that summertime Greenland blocking will continue to be important for positive surface energy changes in the future.

5.2 Future Work

Greenland blocking has already been established as an important contributor to GrIS snowmelt and surface processes, especially since the onset of increased GrIS surface melt at the end of the 20th century. We explore surface energy responses to block location and future blocking activity without directly examining snowmelt.

The impacts of summer block location in Chapter 3 are examined through the use of observations. In a follow-on study to Ward et al. (2020, submitted), we plan to use the Modèle Atmosphérique Régional (MAR) regional climate model to examine how melt trends vary by block location. In the MAR setup, we will use MERRA-2 data for boundary conditions so we

can use the same block days for each block quadrant. Although observational snowmelt data would be ideal, daily MODIS and Making Earth System Data Records for Use in Research Environments (MEaSUREs) snowmelt data only extend through December 2017 and December 2012, respectively. Global climate models are also able to simulate overall GrIS melt trends reasonably well (i.e., Vizcaino et al., 2013), but they produce large biases over the steep GrIS margins. If MAR is incompatible with MERRA-2 data, we will use the latest version of CESM. We will use an offline land model simulation (i.e., no active atmosphere) that assigns MERRA-2 meteorological data to drive surface responses would be an ideal continuation of the study presented in Chapter 3. Although a fully-coupled (i.e., active atmosphere and surface processes) model setup in MAR or CESM could demonstrate snowmelt responses to block location change, but a new set of block days would have to be detected from the atmospheric model output.

Because Chapter 4 has not yet been submitted, most future work will be dedicated to rounding out this study. One way we could add substance to these findings is to incorporate blocking impacts on GrIS snowmelt. Unfortunately, no available CMIP6 models produce daily snowmelt, so monthly snowmelt would have to be compared to daily blocking activity. Although this would involve comparing data with different time resolutions, the number of block days per each month of snowmelt could be used as a weighting factor to better understand model-based output over both future time periods.

Apart from snowmelt, we will add other CMIP6 simulations and data fields to our analysis to better understand future Greenland blocking surface energy flux impacts. At the time of data acquisition, only 5 CMIP6 models provided daily 500mb geopotential height fields. However, since the CMIP6 database is still being populated, it is likely that more models with historical and future daily geopotential height and surface energy fluxes will be added. The

inclusion of more models will be useful for better understanding average CMIP6 Greenland blocking and surface response conditions. Furthermore, only the warmest of the future climate change scenarios (i.e., SSP585) is included in this analysis. If the human population chooses more sustainable energy sources in the future, the results presented in Chapter 4 may not be representative of how surface energy changes with future Greenland blocking activity. We can represent the range of Greenland blocking surface response possibilities by including a lower SSP scenario. Finally, analyzing simulated meteorological variables (e.g., atmospheric temperature, winds, and specific humidity) for each model and time period would be useful for understanding *why* the discussed surface energy flux changes occur.

The seasonality of downwelling shortwave fluxes at the surface is not accounted for in Chapter 4. This results in skewed net shortwave flux anomalies that are likely underestimated when more May and September block days are included. We can account for days outside of June, July, and August by scaling shortwave flux results with scale factors computed for top-of-atmosphere downwelling shortwave fluxes (i.e., scaling method used in Chapter 3) for each CMIP6 model and time period. Alternatively, another option to correct for lower downwelling shortwave fluxes in May and September block days would be to remove block days outside of June, July, and August. If there are at least 5 remaining consecutive block days inside JJA, the block will remain in the dataset. Otherwise, the remaining days will be removed from the blocking dataset. With these research ideas in mind, we are hoping to submit Chapter 4 and additional findings for publication by the end of 2020.

Apart from the research discussed in previous chapters, we could pursue additional science questions related to Greenland surface energy exchange and melt processes in future studies. Although Greenland melt is most prevalent in the summer, atmosphere-surface

interactions in other seasons could precondition the GrIS surface albedo to enhance summertime melt (e.g., Tedesco et al., 2013). One question we would be interested in pursuing is: *How does GrIS total surface energy change during autumn, winter, and spring blocking events?* As in Chapters 3 and 4, we can answer this question with observational data or climate modeling techniques. The annual cycle of solar energy input indicates that the importance of turbulent and longwave energy flux changes during blocking would increase in non-summer seasons. We could also use climate modeling to better understand *the extent to which spring blocking activity preconditions the GrIS to enhance summer melt*. The simplest way to achieve this understanding is to run a fully-coupled global climate model for numerous years. We could then compare GrIS surface albedo characteristics of high and low blocking frequency spring seasons and explain how any changes in albedo result from the corresponding surface energy fluxes. As we see when we compare the effects of summertime blocking on surface energy fluxes in global climate model output in Chapter 4, the responses vary markedly between different models. Finally, as Liu et al. (2016) suggest, declining sea ice coverage in the Arctic increases GrIS melt extent through blocking activity. We think it would be interesting to explore *how the extent of sea ice retreat and the start date of sea ice coverage decline correlates with total GrIS summertime melt*. Depending on the results regarding springtime blocking activity over Greenland, the potential triggering of greater blocking activity as a result of earlier sea ice decline could have implications for GrIS surface processes.

Appendix: Supplementary Cloud and Surface Energy Flux Figures for Chapter 3

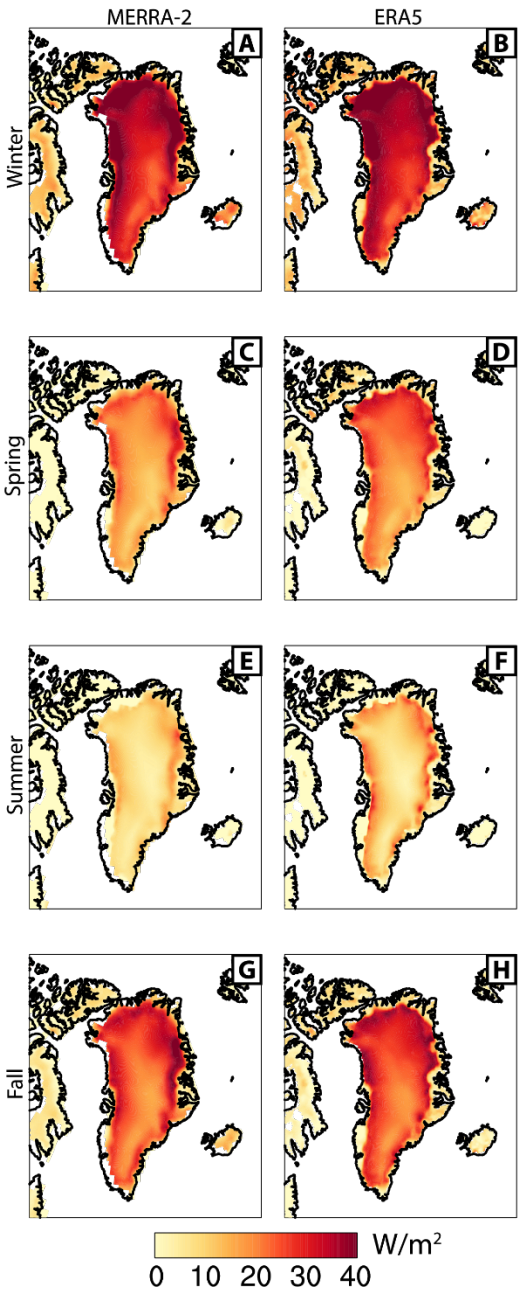

Fig. A.1: Seasonal average sensible heat flux (positive quantities are directed into the surface) for MERRA-2 (left column) and ERA5 (right column) reanalysis data products.

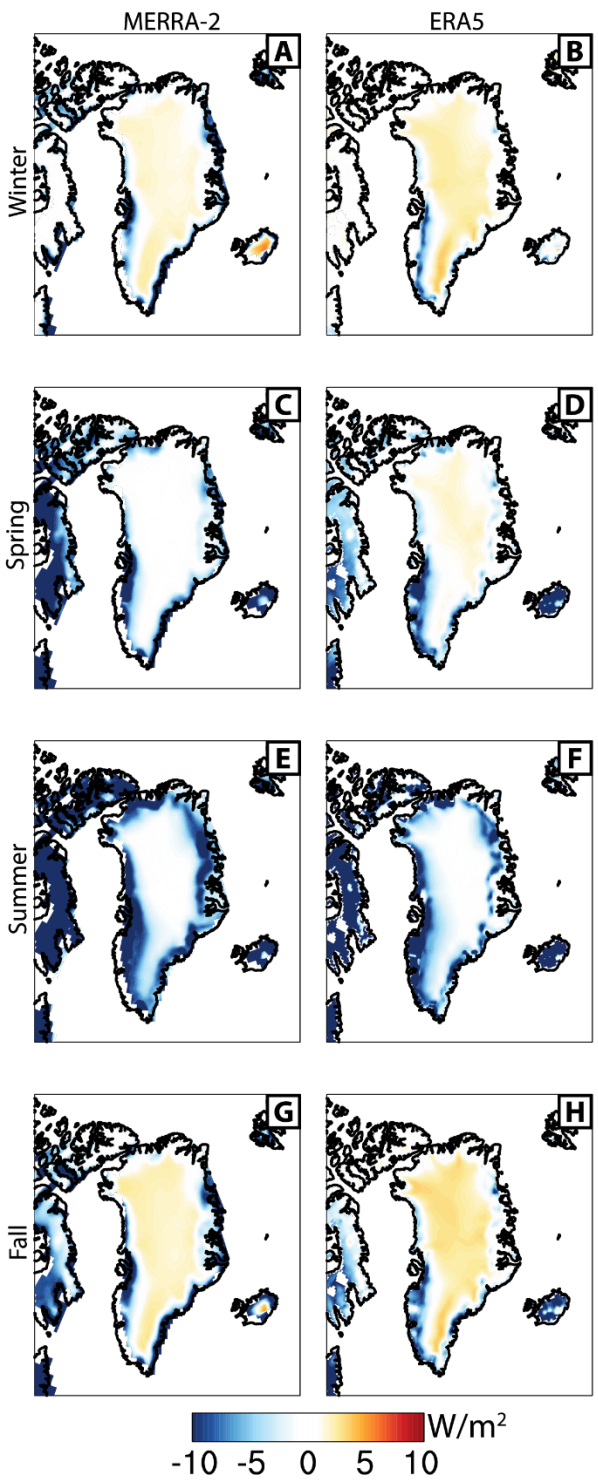

Fig. A.2: Same as Fig. A.1, but for latent heat flux.

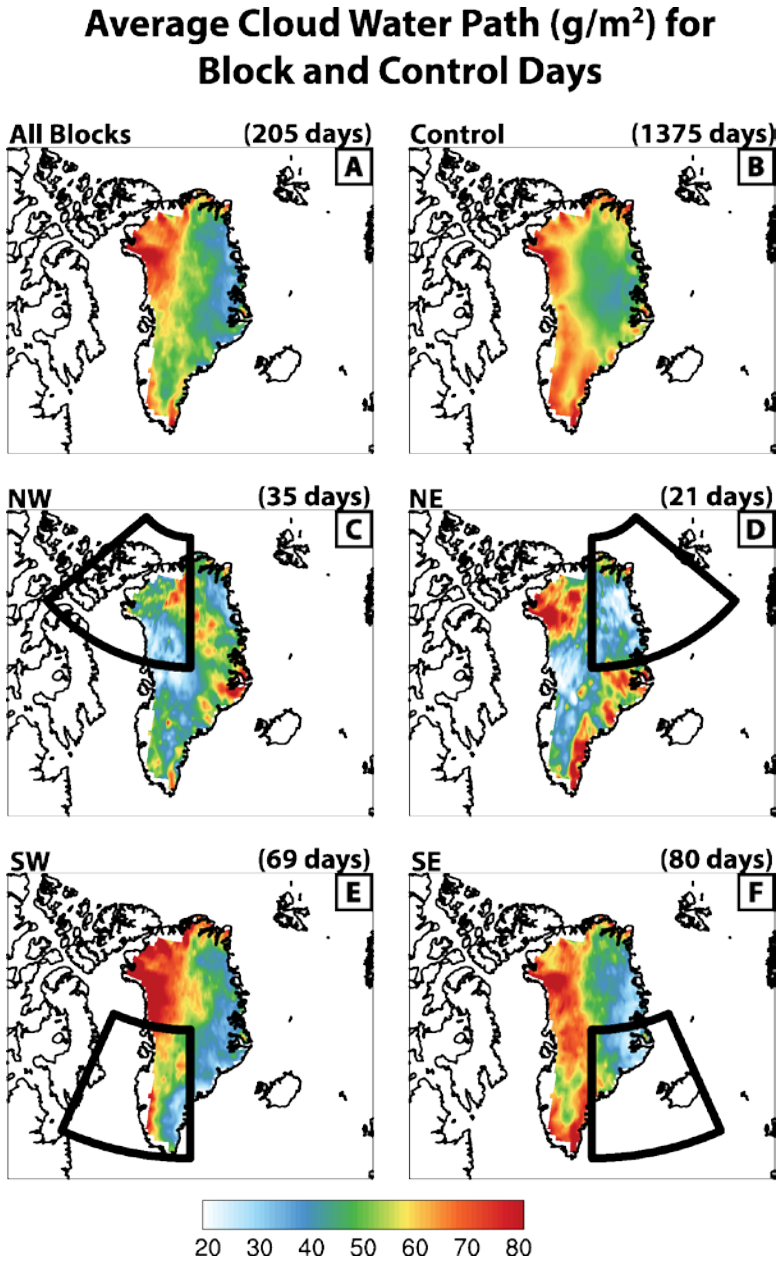

Fig. A.3: Composite absolute MOD06 cloud water path over Greenland (JJA, 2002-2018).

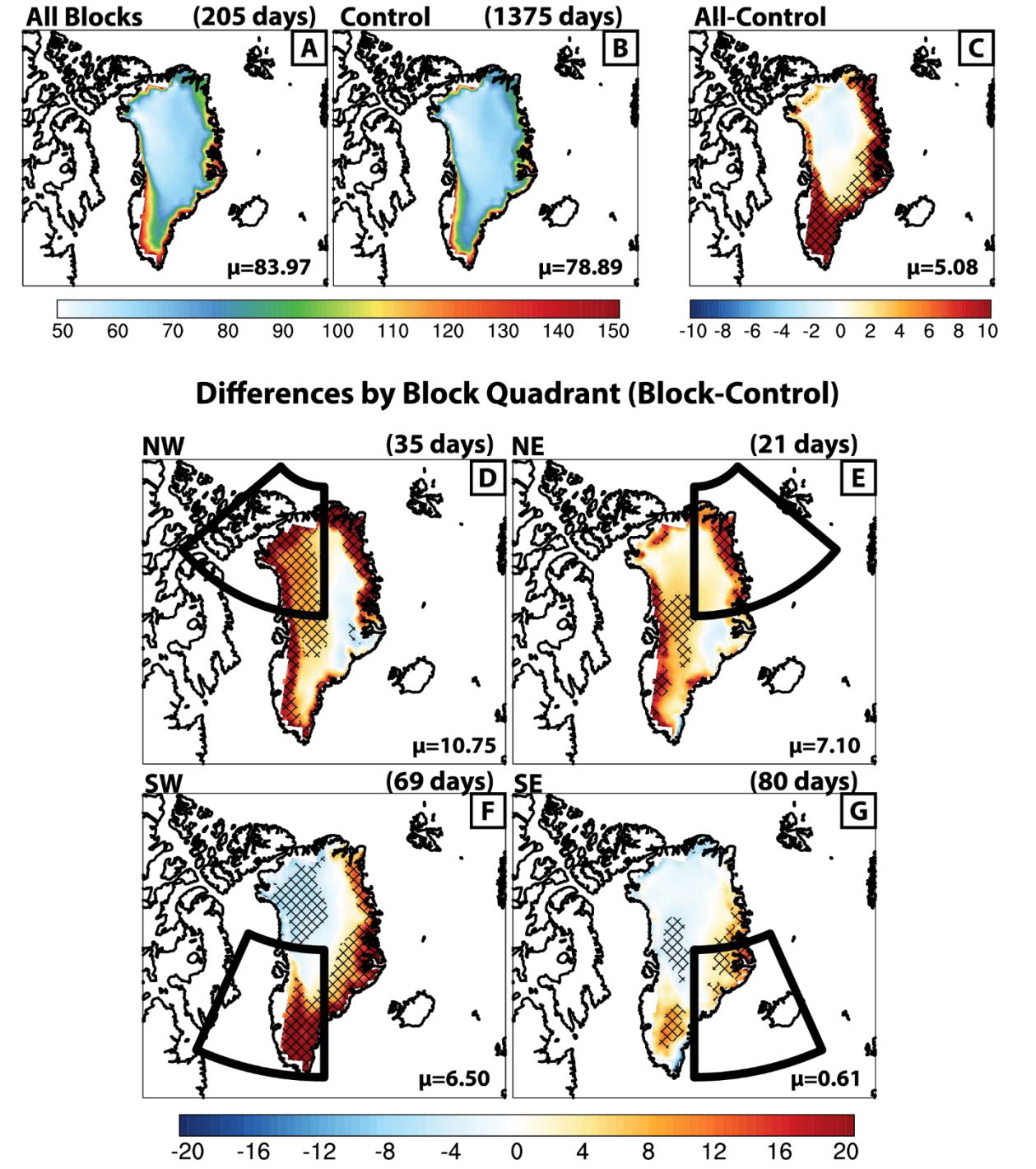

Fig. A.4: Panels A and B show MERRA-2 absolute net shortwave flux for "All Blocks" and "Control", respectively, and their difference is in panel C. Block quadrant-based net shortwave flux changes with respect to "Control" are in panels D through G. The black boxes are the corresponding block quadrant boundaries. Cross-hatching in panels C through G represents statistically significant differences (95% confidence level).

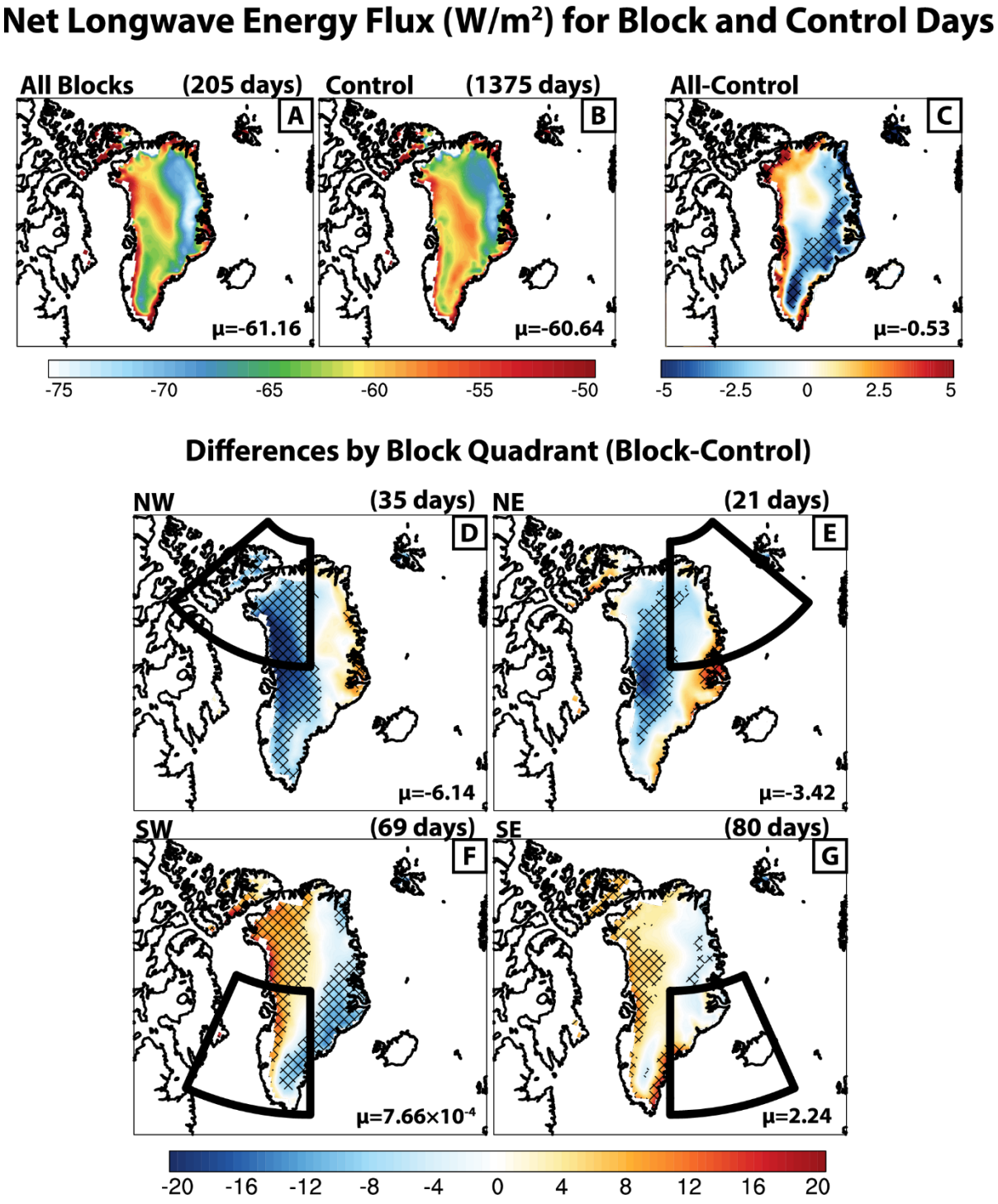

Fig. A.5: Same as Fig. A.4, but for MERRA-2 net longwave flux.

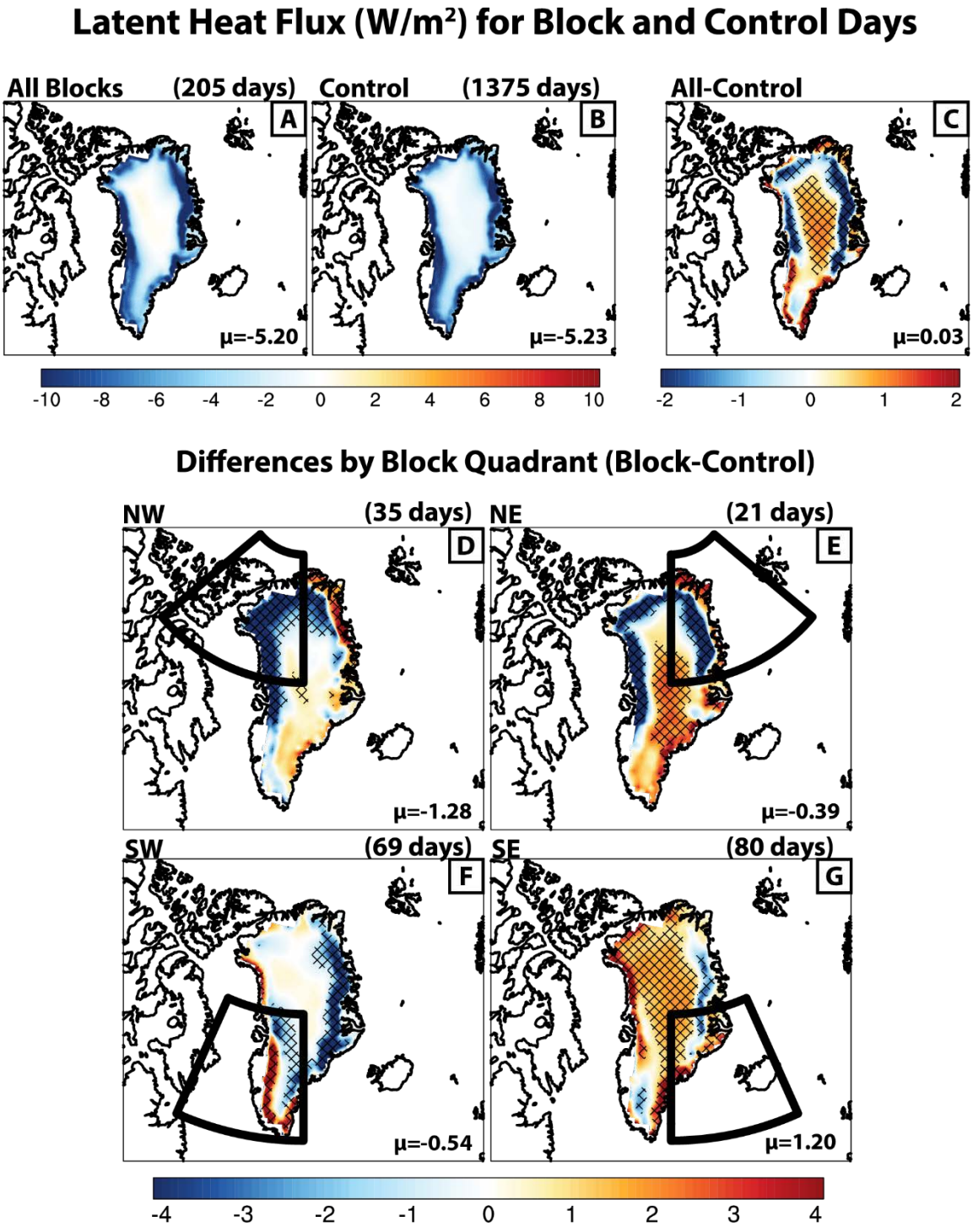

Fig. A.6: Same as Fig. A.2, but for MERRA-2 latent heat flux.

References

Ackerman, S.A., Strabala, K.I., Menzel, W.P., Frey, R.A., Moeller, C.C., & Gumley, L.E. (1998, December 27). Discriminating clear sky from clouds with MODIS. *Journal of Geophysical Research, 103*(D24), 32,141-32,157.

Allen, R.J., & Landuyt, W. (2014). The vertical distribution of black carbon in CMIP5 models: Comparison to observations and the importance of convective transport. *Journal of Geophysical Research: Atmospheres, 119*, 4808-4835, doi:10.1002/2014JD021595.

Ban-Weiss, G.A., Cao, L., Bala, G., & Caldeira, K. (2011). Dependence of climate forcing and response on the altitude of black carbon aerosols. *Climate Dynamics, 38*(5), 897-911, doi:10.1007/s00382-011-1052-y.

Barriopedro, D., García-Herrera, R., Lupo, A.R., & Hernández, E. (2006, March 15). A Climatology of Northern Hemisphere Blocking. *Journal of Climate, 19*, 1042-1063.

Belleflamme, A., Fettweis, X., & Erpicum, M. (2015). Recent summer Arctic atmospheric circulation anomalies in a historical perspective. *The Cryosphere, 9*, 53-64, doi:10.5194/tc-9-53-2015.

Belleflamme, A., Fettweis, X., Lang, C., & Erpicum, M. (2013) .Current and future atmospheric circulation at 500hPa over Greenland simulated by the CMIP3 and CMIP5 global models. *Climate Dynamics, 41*, 2061-2080, doi:10.1007/s00382-012-1538-2.

Bennartz, R., Shupe, M.D., Turner, D.D., Walden, V.P., Steffen, K., Cox, C.J., et al. (2013, April 4). July 2012 Greenland melt extent enhanced by low-level liquid clouds. *Nature, 496*, 83-86, doi:10.1038/nature12002.

Bond, T.C., Doherty, S.J., Fahey, D.W., Forster, P.M., Berntsen, T., DeAngelo, B.J., …Zender, C.S. (2013). Bounding the role of black carbon in the climate system: A scientific assessment. *Journal of Geophysical Research: Atmospheres, 118*, 5380-5552, doi: 10.1002/jgrd.50171.

Bond, T.C., Bhardwaj, E., Dong, R., Jogani, R., Jung, S., Roden, C., …, Trautmann, N.M. (2007). Historical emissions of black and organic carbon aerosol from energy-related combustion, 1850-2000. *Global Biogeochemical Cycles, 21*(GB2018), doi:10.1029/2006GB002840.

Bond, T.C., Charlson, R.J., & Heintzenburg, J. (1998, February). Quantifying the emission of light-absorbing particles: Measurements tailored to climate studies. *Geophysical Research Letters, 25*(3), 337-340.

Bonne, J-L., Steen-Larsen, H.C., Risi, C., Werner, M., Sodemann, H., Lacour, J-L., Fettweis, X., …Masson-Delmotte, V. (2015). The summer 2012 Greenland heat wave: In situ and remote sensing observations of water vapor isotropic composition during an atmospheric river event. *Journal of Geophysical Research: Atmospheres, 120*, 2970-2989, doi:10.1002/2014JD022602.

Bory, A.J.-M., Biscaye, P.E., Piotrowski, A.M., & Steffensen, J.P. (2003). Regional variability of ice core dust composition and provenance in Greenland. *Geochemistry, Geophysics, Geosystems, 4*(12), doi:10.1029/2003GC000627.

Box, J.E., Fettweis, X., Stroeve, J.C., Tedesco, M., Hall, D.K., & Steffen, K. (2012). Greenland ice sheet albedo feedback: thermodynamics and atmospheric drivers. *The Cryosphere, 6*, 821-839, doi:10.5194/tc-6-821-2012.

Cassano, J.J., Uotila, P., & Lynch, A. (2006). Changes in synoptic weather patterns in the polar regions in the twentieth and twenty-first centuries, part 1: Arctic. *International Journal of Climatology, 26*, 1027-1049.

Cawkwell, F.G.L., & Bamber, J.L. (2002). The impact of cloud cover on the net radiation budget for the Greenland ice sheet. *Annals of Glaciology, 34*, 141-149.

Chen, X. & Luo, D. (2017). Arctic sea ice decline and continental cold anomalies: Upstream and downstream effects of Greenland blocking, *Geophysical Research Letters, 44*, 3411-3419, doi:10.1002/2016GL072387.

Chung, S.H., & Seinfeld, J.H. (2002). Global distribution and climate forcing of carbonaceous aerosols. *Journal of Geophysical Research, 107*(D19,4407), doi:10.1029/2001JD001397.

Church, J.A., Clark, P.U., Cazenave, A., Gregory, J.M., Jevrejeva, S., Levermann, A., …, Unnikrishnan, A.S. (2013). Sea level change. In: Climate *Change 2013: The Physical Science Basis. Contribution of Working Group I to the Fifth Assessment Report of the Intergovernmental Panel on Climate Change*. [Stocker, T.F., Qin, D., Plattner, G.-K., Tignor, M., Allen, S.K., Boschung, J., …, Midgley, P.M. (eds.)]. Cambridge University Press, Cambridge, United Kingdom and New York, NY, USA.

Chýlek, P., Ramaswamy, V., & Cheng, R.J. (1984). Effect of Graphitic Carbon on the Albedo of Clouds. *Journal of the Atmospheric Sciences, 41*(21), 3076-3084.

Clark, S.K., Ward, D.S., & Mahowald, N.M. (2015). The sensitivity of global climate to the episodicity of fire aerosol emissions. *Journal of Geophysical Research: Atmospheres, 120*, 11589-11607, doi:10.1002/2015JD024068.

Copernicus Climate Change Service (CS3). (2017). ERA5: Fifth generation of ECMWF atmospheric reanalyses of the global climate. Copernicus Climate Change Service Climate Data Store (CDS), accessed on June 24, 2020. https://cds.climate.copernicus.eu/cdsapp#!/home

Croci-Maspoli, M., Schwierz, C., & Davies, H.C. (2007, February 15). A Multifaceted Climatology of Atmospheric Blocking and Its Recent Linear Trend. *Journal of Climate, 20*, 633-649, doi:10.1175/JCLI4029.1.

Curry, J.A., Rossow, W.B., Randall, D., & Schramm, J.L. (1996, August). Overview of Arctic Cloud and Radiation Characteristics. *Journal of Climate, 9*, 1731-1764.

Cullather, R.I., & Nowicki, S.M.J. (2018, March 1). Greenland Ice Sheet Surface Melt and Its Relation to Daily Atmospheric Conditions. *Journal of Climate, 31,* 1897-1919, doi:10.1175/JCLI-D-17-0447.1.

Davini, P, Cagnazzo, C., Neale, R., & Tribbia, J. (2012). Coupling between Greenland blocking and the North Atlantic Oscillation pattern. *Geophysical Research Letters, 39*(L14701), doi:10.1029/2012GL052315.

de Boer, G., Chapman, W., Kay, J.E., Medeiros, B., Shupe, M.D., Vavrus, S., & Walsh, J. (2012). A Characterization of the Present-Day Arctic Atmosphere in CCSM4. *Journal of Climate, 25*, 2676-2695.

Delhasse, A., Kittel, C., Amory, C., Hofer, S., van As, D., Fausto, R.S., & Fettweis, X. (2020, March). Brief Communication: Evaluation of the near-surface climate in ERA5 over the Greenland Ice Sheet. *The Cryosphere, 14*, 957-965. https://doi.org/10.5194/tc-14-957-2020.

Delhasse, A., Fettweis, X., Kittel, C., Amory, C., & Agosta, C. (2018). Brief communication: Impact of the recent atmospheric circulation change in summer on the future surface mass balance of the Greenland Ice Sheet. *The Cryosphere, 12*, 3409-3418. https://doi.org/10.5194/tc-12-3409-2018.

Doherty, S.J., Warren, S.G., Grenfell, T.C., Clarke, A.D., & Brandt, R.E. (2010). Light-absorbing impurities in Arctic Snow. *Atmospheric Chemistry and Physics, 10*, 11647-11680, doi:10.5194/acp-10-11647-2010.

Doyle, S.H., Hubbard, A., van de Wal, R.S.W., Box, J.E. van As, D., Scharrer, K., …, Hubbard, B. (2015, August). Amplified melt and flow of the Greenland ice sheet driven by late-summer cyclonic rainfall. *Nature Geoscience, 8*, 647-656, doi:10.1038/NGEO2482.

Dunn-Sigouin, E., Son, S-W., & Lin, H. (2013, February). Evaluation of Northern Hemisphere Blocking Climatology in the Global Environment Multiscale Model. *Monthly Weather Review, 141*, 707-727, doi:10.1175/MWR-D-12-00134.1.

Dunn-Sigouin, E., & Son, S-W. (2013). Northern Hemisphere blocking frequency and duration in the CMIP5 models. *Journal of Geophysical Research: Atmospheres, 118*, 1179-1188, doi:10.1002/jgrd.50143.

Edwards-Opperman, J., Cavallo, S., & Turner, D. (2018, April). The Occurrence and Properties of Long-Lived Liquid-Bearing Clouds over the Greenland Ice Sheet and Their Relationship to

the North Atlantic Oscillation. *Journal of Applied Meteorology and Climatology, 57*, 921-935, doi:10.1175/JAMC-D-17-0230.1.

Ettema, J., van den Broeke, M.R., van Meijgaard, E., & van de Berg, W.J. (2010). Climate of the Greenland ice sheet using a high-resolution climate model-Part 2: Near-surface climate and energy balance. *The Cryosphere, 4*, 529-544, doi:10.5194/tc-4-529-2010.

Eyring, V., Bony, S., Meehl, G.A., Senior, C.A., Stevens, B., Stouffer, R.J., & Taylor, K.E. (2016). Overview of the Coupled Model Intercomparison Project Phase 6 (CMIP6) experimental design and organization. *Geoscientific Model Development, 9*, 1937-1958, doi:10.5194/gmd-9-1937-2016.

Fausto, R.S., van As, D., Box, J.E., Colgan, W., Langen, P.L., & Mottram, R.H. (2016). The implication of nonradiative energy fluxes dominating Greenland ice sheet exceptional ablation area surface melt in 2012. *Geophysical Research Letters, 43*, 2649-2658, doi:10.1002/2016GL067720.

Fettweis, X., Box, J.E., Agosta, C., Amory, C., Kittel, C., Lang, C., …, Gallée, H. (2017). Reconstructions of the 1900-2015 Greenland ice sheet surface mass balance using the regional climate MAR model. *The Cryosphere, 11*, 1015-1033. doi.10.5194/tc-11-1015-2017.

Fettweis, X., Hanna, E., Lang, C., Belleflamme, A., Erpicum, M., & Gallée, H. (2013). Brief Communication: Important role of the mid-tropospheric atmospheric circulation in the recent surface melt increase over the Greenland ice sheet. *The Cyrosphere, 7*, 241-248, doi:10.5194/tc-7-241-2013.

Fettweis, X., Mabille, G., Erpicum, M., Nicolay, S., & Van den Broeke, M. (2011). The 1958-2009 Greenland ice sheet surface melt and the mid-tropospheric atmospheric circulation. *Climate Dynamics*, 36, 139-159, doi:10.1007/s00382-010-0772-8.

Flanner, M.G. (2013). Arctic climate sensitivity to local black carbon. *Journal of Geophysical Research: Atmospheres, 118*, 1840-1851, doi:10.1002/jgrd.50176.

Flanner, M.G., Zender, C.S., Randerson, J.T., & Rasch, P.J. (2007). Present-day climate forcing and response from black carbon in snow. *Journal of Geophysical Research, 112*(D11202), doi:10.1029/2006JD008003.

Flanner, M.G., & Zender, C.S. (2006). Linking snowpack microphysics and albedo evolution. *Journal of Geophysical Research, 111*(D12208), doi:10.1029/2005JD006834

Flanner, M.G., & Zender, C.S. (2005). Snowpack radiative heating: Influence on Tibetan Plateau climate. *Geophysical Research Letters, 32*(L06501), doi:10.1029/2004GL022076.

Flannigan, M. D., Krawchuk, M. A., de Groot, W. J., Wotton, B. M. & Gowman, L. M. (2009). Implications of changing climate for global wildland fire. *International Journal of Wildland Fire, 18,* 483-507, doi: 10.1071/WF08187.

Flannigan, M., S.Cantin, A., deGroot, W. J., Wotton, M., Newbery, A. & Gowman, L. M. (2013). Global wildland fire season severity in the 21st century. *Forest Ecology and Management, 294,* 54-61, doi: 10.1016/j.foreco.2012.10.022.

Forsythe, N., Hardy, A.J., Fowler, H.J., Blenkinsop, S., Kilsby, C.G., Archer, D.R., & Hashmi, M.Z. (2015, May 1). A Detailed Cloud Fraction Climatology of the Upper Indus Basin and Its Implications for Near-Surface Air Temperature. *Journal of Climate, 28*, 3537-3556, doi:10.1175/JCLI-D-14-00505.1.

Franco, B., Fettweis, X., & Erpicum, M. (2013). Future projections of the Greenland ice sheet energy balance driving the surface melt. *The Cryosphere, 7*, 1-18, doi:10.5194/tc-7-1-2013.

Gelaro, R., McCarty, W., Suárez, M.J., Todling, R., Molod, A., Takacs, L., et al. (2017, July 15). The Modern-Era Retrospective Analysis for Research and Applications, Version 2 (MERRA-2). *Journal of Climate, 30*, 5419-5454, doi:10.1175/JCLI-D-16-0758.1.

Graham, R.M., Hudson, S.R., & Maturilli, M. (2019, May). Improved Performance of ERA5 in Arctic Gateway Relative to Four Global Atmospheric Reanlayses. *Geophysical Research Letters, 46*(11), 6138-6147. https://doi.org/10.1029/2019GL082781.

Gregory, J.M., Huybrechts, P., & Raper, S.C.B. (2004). Climatology: Threatened loss of the Greenland ice-sheet. *Nature, 428*, 616.

Häkkinen, S., Hall, D.K., Shuman, C.A., Worthen, D.L., & DiGirolamo, N.E. (2014). Greenland ice sheet melt from MODIS and associated atmospheric variability. *Geophysical Research Letters, 41*, 1600-1607, doi:10.1002/2013GL059185.

Hanna, E., Hall, R.J., Cropper, T.E., Ballinger, T.J., Wake, L., Mote, T., & Cappelen, J. (2018a). Greenland blocking index daily series 1851-2015: Analysis of changes in extremes and links with North Atlantic and UK climate variability and change. *International Journal of Climatology, 38*, 3546-3564, DOI: 10.1002/joc.5516.

Hanna, E., Fettweis, X., & Hall, R.J. (2018b). Brief Communication: Recent changes in summer Greenland blocking captured by none of the CMIP5 models. *The Cryosphere, 12*, 3287-3292. https://doi.org/10.5194/tc-12-3287-2018.

Hanna, E., Cropper, T.E., Hall, R.J., & Cappelen, J. (2016). Greenland Blocking Index 1851-2015: a regional climate change signal. *International Journal of Climatology, 36*, 4847-4861, doi:10.1002/joc.4673.

Hanna, E., Cropper, T.E., Jones, P.D., Scaife, A.A., & Allan, R. (2015). Recent seasonal asymmetric changes in the NAO (a marked summer decline and increased winter variability) and associated changes in the AO and Greenland Blocking Index. *International Journal of Climatology, 35*, 2540-2554, doi:10.1002/joc.4157.

Hanna, E., Fettweis, X., Mernild, S.H., Cappelen, J., Ribergaard, M.H., Shuman, C.A., et al. (2014). Atmospheric and oceanic climate forcing of the exceptional Greenland ice sheet surface melt in summer 2012. *International Journal of Climatology, 34*, 1022-1037, doi:10.1002/joc.3743.

Hanna, E., Huybrechts, P., Steffen, K., Cappelen, J., Huff, R., Shuman, C., … Griffiths, M. (2008, January). Increased Runoff from Melt from the Greenland Ice Sheet: A Response to Global Warming. *Journal of Climate, 21*, 331-341.

Hansen, J., & Nazarenko, L. (2004, January). Soot climate forcing via snow and ice albedos. *Proceedings of the National Academy of Sciences, 101*(2), 423-428, doi:10.1073/pnas.2237157100.

Hassanzadeh, P., & Kuang, Z. (2015). Blocking variability: Arctic Amplification versus Arctic Oscillation. *Geophysical Research Letters, 42*, 8586-8595, doi:10.1002/2015GL065923.

Haywood, J.M., & Ramaswamy, V. (1998, March). Global sensitivity studies of the direct radiative forcing due to anthropogenic sulfate and black carbon aerosols. *Journal of Geophysical Research, 103*(D6), 6043-6058.

Hakuba, M.Z., Folini, D., Wild, M., & Schär, C. (2012). Impact of Greenland's topographic height on precipitation and snow accumulation in idealized simulations. *Journal of Geophysical Research, 117*(D09107), doi:10.1029/2011JD017052.

Hofer, S., Tedstone, A.J., Fettweis, X., & Bamber, J.L. (2017, June 28). Decreasing cloud cover drives the recent mass loss on the Greenland Ice Sheet. *Science Advances, 3*(6), doi:10.1126/sciadv.1700584.

Hofer, S., Tedstone, A.J., Fettweis, X., & Bamber, J.L. (2019, July). Cloud microphysics and circulation anomalies control differences in future Greenland melt. *Nature Climate Change, 9*, 523-528, https://doi.org/10.1038/s41558-019-0507-8.

Humboldt State University. (2019). *Electromagnetic Spectrum: Introduction.* Accessed on 15 May 2020. http://gsp.humboldt.edu/OLM/Courses/GSP_216_Online/lesson1-2/spectrum.html.

Jacobson, M.Z. (2001). Global direct radiative forcing due to multicomponent anthropogenic and natural aerosols. *Journal of Geophysical Research, 106*(D2), 1551-1568.

Jacobson, M.Z. (2004). Climate response of fossil fuel and biofuel soot, accounting for soot's feedback to snow and sea ice albedo and emissivity. *Journal of Geophysical Research, 109*(D21201), doi:10.1029/2004JD004945.

Jiao, C., Flanner, M.G., Balkanski, Y., Bauer, S.E., Bellouin, N., Berntsen, T.K., … Zhang, K. (2014). An AeroCom assessment of black carbon in Arctic snow and sea ice. *Atmospheric Chemistry and Physics, 14*, 2399-2417, doi:10.5194/acp- 14-2399-2014.

Jiao, C., & Flanner, M.G. (2016). Changing black carbon transport to the Arctic from present day to the end of the 21st century. *Journal of Geophysical Research: Atmospheres, 121*, 4734-4750, doi:10.1002/2015JD023964.

Johansson, E., Devasthale, A., Tjernström, M., Ekman, A.M.L., & L'Ecuyer, T. (2017). Response of the lower troposphere to moisture intrusions into the Arctic. *Geophysical Research Letters, 44*, 2527-2536, doi:10.1002/2017GL072687.

Jolly, W.M., Cochrane, M.A., Freeborn, P.H., Holden, Z.A., Brown, T.J., Williamson, G.J., & Bowman, D.M.J.S. (2015). Climate-induced variations in global wildfire danger from 1979 to 2013. *Nature Communications, 6*(7537), doi:10.1038/ncomms8537.

Kay, J.E., & Gettelman, A. (2009). Cloud influence on and response to seasonal Arctic sea ice loss. *Journal of Geophysical Research, 114*(D18204), doi:10.1029/2009JD011773.

Kay, J.E., Hillman, B.R., Klein, S.A., Zhang, Y., Medeiros, B., Pincus, R., … Ackerman, T.P. (2012). Exposing Global Cloud Biases in the Community Atmosphere Model (CAM) Using Satellite Observations and Their Corresponding Instrument Simulators. *Journal of Climate, 25*, 5190-5207, doi:10.1175/JCLI-D-11-00469.1.

Keegan, K.M., Albert, M.R., McConnell, J.R., & Baker, I. (2014). Climate change and forest fires synergistically drive widespread melt events of the Greenland Ice Sheet. *Proceedings of the National Academy of Sciences, 111*(22), 7964-7967, doi:10.1073/pnas.1405397111.

Kelly, R., Chipman, M.L., Higuera, P.E., Stefanova, I., Brubaker, L.B., & Hu, F.S. (2013, August). Recent burning of boreal forests exceeds fire regime limits of the past 10,000 years. *Proceedings of the National Academy of Sciences, 110*(32), 13055-13060, doi:10.1037/pnas.1305069110.

Kennedy, D., Parker, T., Woollings, T., Harvey, B., & Shaffrey, L. (2016). The response of high-impact blocking weather systems to climate change, *Geophysical Research Letters, 43*, 7250-7258, doi:10.1002/2016GL069725.

Khan, S.A., Aschwanden, A., Bjørk, A.A., Wahr, J., Kjeldsen, K.K., & Kjær, K.H. (2015). Greenland ice sheet mass balance: a review. *Reports on Progress in Physics, 78*(046801), doi:10.1088/0034-4885/78/4/046801.

Koch, D., Schulz, M., Kinne, S., McNaughton, C., Spackman, J.R., Balkanski, Y., … van Aardenne, J.A. (2009). Evaluation of black carbon estimations in global aerosol models. *Atmospheric Chemistry and Physics, 9*, 9001-9026.

Kusunoki, S., Mizuta, R., & Hosaka, M. (2015, September). Future changes in precipitation intensity over the Arctic projected by a global atmospheric model with a 60-km grid size. *Polar Science, 9*(3), 277-292. https://doi.org/10.1016/j.polar.2015.08.001.

Lacour, A., Chepfer, H., Shupe, M.D., Miller, N.B., Noel, V., Kay, J., …, Guzman, R. (2017, August 1). Greenland Clouds Observed in CALIPSO-GOCCP: Comparison with Ground-Based Summit Observations. *Journal of Climate, 30,* 6065-6083, doi:10.1175/JCLI-D-16-0552.1.

Lamarque, J.-F., Bond, T.C., Eyring, V., Granier, C., Heil, A., Klmont, Z., …van Vuuren, D.P.. (2010). Historical (1850-2000) gridded anthropogenic and biomass burning emissions of reactive gases and aerosols: methodology and application. *Atmospheric Chemistry and Physics, 10,* 7017-7039, doi:10.5194/acp-10-7017-2010.

Lenaerts, J.T.M., Medley, B., van den Broeke, M., & Wouters, B. (2019). Observing and Modeling Ice Sheet Surface Mass Balance. *Reviews of Geophysics, 57,* 376-420, doi:10.1029/2018RG000622.

Lenaerts, J.T.M., Van Tricht, K., Lhermitte, S., & L'Ecuyer, T.S. (2017). Polar clouds and radiation in satellite observations, reanalyses, and climate models. *Geophysical Research Letters, 44*, 3355-3364, doi:10.1002/2016GL072242.

Lim, Y-K., Schubert, S.D., Nowicki, S.M.J., Lee, J.N., Molod, A.M., Cullather, R.I., et al. (2016). Atmospheric summer teleconnections and Greenland Ice Sheet surface mass variations: insights from MERRA-2. *Environmental Research Letters, 11,* doi:10.188/1748-9326/11/2/024002.

Liu, J., Chen, Z., Francis, J., Song, M., Mote, T., & Hu, Y. (2016, May 1). Has Arctic Sea Ice Loss Contributed to Increased Surface Melting of the Greenland Ice Sheet? *Journal of Climate, 29*, 3373-3386, doi:10.1175/JCLI-D-15-0391.1.

Liu, X., Easter, R.C., Ghan, S.J., Zaveri, R., Rasch, P., Shi, X., … Mitchell, D. (2012). Toward a minimal representation of aerosols in climate models: description and evaluation in the Community Atmosphere Model CAM5. *Geoscientific Model Development, 5*, 709-739, doi: 10.5194/gmd-5-709-2012.

Liu, Y., Ackerman, S.A., Maddux, B.C., Key, J.R., & Frey, R.A. (2010, April). Errors in Cloud Detection over the Arctic Using a Satellite Imager and Implications for Observing Feedback Mechanisms. *Journal of Climate, 23*, 1894-1907, doi:10.1175/2009JCLI3386.1.

Lupo, A.R., & Smith, P.J. (1994). Climatological features of blocking anticyclones in the Northern Hemisphere. *Tellus, 47A*, 439-456.

Marlon, J.R., Bartlein, P.J., Daniau, A-L., Harrison, S.P., Maezumi, S.Y., Power, M.J., … Vanniére, B. (2013). Global biomass burning: a synthesis and review of Holocene paleofire records and their controls. *Quaternary Science Reviews, 65*, 5-25.

Masato, G., Hoskins, B.J., & Woollings, T. (2013, September 15). Winter and Summer Northern Hemisphere Blocking in CMIP5 Models, *Journal of Climate, 26,* 7044-7059, doi:10.1175/JCLI-D-12-00466.1.

Matsueda, M, & Endo, H. (2017). The robustness of future changes in Northern Hemisphere blocking: A large ensemble projection with multiple sea surface temperature patterns. *Geophysical Research Letters, 44*, doi:10.1002/2017GL073336.

Mattingly, K.S., Mote, T.L., & Fettweis, X. (2018). Atmospheric River Impacts on Greenland Ice Sheet Surface Mass Balance. *Journal of Geophysical Research: Atmospheres, 123,* 8538-8560, doi:10.1029/2018JD028714.

Mattingly, K.S., Ramseyer, C.A., Rosen, J.J., Mote, T.L., & Muthyala, R. (2016). Increasing water vapor transport to the Greenland Ice Sheet revealed using self-organizing maps. *Geophysical Research Letters, 43,* 9250-9258, doi:10.1002/2016GL070424.

McConnell, J.R., Edwards, R., Kok, G.L., Flanner, M.G., Zender, C.S., Saltzman, E.S., … Kahl, J.D.W. (2007, September). 20th-Century Industrial Black Carbon Emissions Altered Arctic Climate Forcing. *Science, 317*, 1381-1384, doi:10.1126/science.1144856

McIlhattan, E.A., L'Ecuyer, T.S., & Miller, N.B. (2017, June). Observational Evidence Linking Arctic Supercooled Liquid Cloud Biases in CESM to Snowfall Processes. *Journal of Climate, 30*, 4477-4495, doi:10.1175/JCLI-D-16.0666.1.

McLeod, J.T., & Mote, T.L. (2016). Linking interannual variability in extreme Greenland blocking episodes to the recent increase in summer melting across the Greenland ice sheet. *International Journal of Climatology, 36*, 1484-1499, doi:10.1002/joc.4440.

McLeod, J.T., & Mote, T.L. (2015). Assessing the role of precursor cyclones on the formation of extreme Greenland blocking episodes and their impact on summer melting across the Greenland ice sheet. *Journal of Geophysical Research: Atmospheres, 120,* doi:10.1002/2015JD023945.

Menon, S., Hansen, J., Nazarenko, L., & Luo, Y. (2002). Climate Effects of Black Carbon Aerosols in China and India. *Science, 297*, 2250-2253, doi:10.1126/science.1075159.

Meridith, M., Sommerkorn, M., Cassotta, S., Derksen, C., Ekaykin, A., Hollowed, A., …, Schuur, E.A.G. (2019). Polar Regions. In: *IPCC Special Report on the Ocean and Cryosphere in a Changing Climate*. [Pörtner, H.-O., Roberts, D.C., Masson-Delmotte, V., Zhai, P., Tignor, M., Poloczanska, E., …, Weyer, N.M. (eds.)]. In press.

Miller, N.B., Shupe, M.D., Cox, C.J., Walden, V.P., Turner, D.D., & Steffen, K. (2015, August 1). Cloud Radiative Forcing at Summit, Greenland. *Journal of Climate, 28*, 6267-6280, doi:10.1175/JCLI-D-15-0076.1.

Mioduszewski, J.R., Vavrus, S., Wang, M., Holland, M., & Landrum, L. (2019). Past and future interannual variability in Arctic sea ice in coupled climate models. *The Cryosphere, 13*, 113-124. https://doi.org/10.5194/tc-13-113-2019.

Mioduszewski, J.R., Rennermalm, A.K., Hammann, A., Tedesco, M., Noble, E.U., Stroeve, J.C., et al. (2016). Atmospheric drivers of Greenland surface melt revealed by self-organizing maps. *Journal of Geophysical Research: Atmospheres, 121,* doi:10.1002/2015JD024550.

Morrison, H., de Boer, G., Feingold, G., Harrington, J., Shupe, M.D., & Sulia, K. (2012, January). Resilience of persistent Arctic mixed-phase clouds. *Nature Geoscience, 5,* 11-17, doi:10.1038/NGEO1332.

Mouginot, J., Rignot, E., Bjørk, A.A., van den Broeke, M., Millan, R., Morlighem, M., …, Wood, M. (2019, May 7). Forty-six years of Greenland Ice Sheet mass balance from 1972 to 2018. *Proceedings of the National Academy of Science, 116*(19), 9239-9244. www.pnas.org/cgi/doi/10.1073/pnas.1904242116.

Neff, W., Compo, G.P., Ralph, F.M., & Shupe, M.D. (2014). Continental heat anomalies and the extreme melting of the Greenland ice surface in 2012 and 1889. *Journal of Geophysical Research: Atmospheres, 119,* 6520-6536, doi:10.1002/2014JD021470.

Nghiem, S.V., Hall, D.K., Mote, T.L., Tedesco, M., Albert, M.R., Keegan, K., …Neumann, G. (2012). The extreme melt across the Greenland ice sheet in 2012. *Geophysical Research Letters, 39*(L20502), doi:10.1029/2012GL053611.

Nusbaumer, J., Alexander, P.M., LeGrande, A.N., & Tedesco, M. (2019). Spatial shift of Greenland moisture sources related to enhanced Arctic warming. *Geophysical Research Letters, 46,* 14,723-14,731. https://doi.org/10.1029/2019GL084633.

Ocko, I.B., Ramaswamy, V., Ginoux, P., Ming, Y., & Horowitz, L.W. (2012). Sensitivity of scattering and absorbing aerosol direct radiative forcing to physical climate factors. *Journal of Geophysical Research, 117*(D20203), doi:10.1029/2012JD018019.

O'Neill, B.C., Kriegler, E., Ebi, K.L., Kemp-Benedict, E., Riahi, K., Rothman, D.S., …, Solecki, W. (2017). The roads ahead: Narratives for shared socioeconomic pathways describing world futures in the 21st century. *Global Environmental Change, 42,* 169-180. http://dx.doi.org/10.1016/j.gloenvcha.2015.01.004.

Overland, J.E., Francis, J.A., Hanna, E., & Wang, M. (2012). The recent shift in early summer Arctic atmospheric circulation. *Geophysical Research Letters, 39*(L19804), doi:10.1029/2012GL053268.

Painter, T.H., Barrett, A.P., Landry, C.C., Neff, J.C., Cassidy, M.P., Lawrence, C.R., … Farmer, G.L. (2007). Impact of disturbed desert soils on duration of mountain snow cover. *Geophysical Research Letters, 34*(L12502), doi:10.1029/2007GL030284.

Pfahl, S., Schwierz, C., Croci-Maspoli, M., Grams, C.M., & Wernli, H. (2015, July 20). Importance of latent heat release in ascending air streams for atmospheric blocking. *Nature Geoscience, 8,* 610-615, doi:10.1038/NGEO2487.

Pithan, F., & Mauritsen, T. (2014, March). Arctic amplification dominated by temperature feedbacks in contemporary climate models. *Nature Geoscience, 7*, 181-184, doi:10.1038/NGEO2071.

Platnick, S., Meyer, K.G., King, M.D., Wind, G., Amarasinghe, N., Marchant, B., et al. (2017, January 1). The MODIS Cloud Optical and Microphysical Products: Collection 6 Updates and Examples from Terra and Aqua. *IEEE Transactions on Geoscience and Remote Sensing, 55*(1), 502-525.

Platnick, S., Li, J.Y., King, M.D., Gerber, H., & Hobbs, P.V. (2001, July 27). A solar reflectance method for retrieving the optical thickness and droplet size of liquid water clouds over snow and ice surfaces. *Journal of Geophysical Research, 106*(D14), 15,185-15,199.

Polashenski, C.M., Dibb., J.E., Flanner, M.G., Chen, J.Y., Courville, Z.R., Lai, A.M., … Bergin, M. (2015). Neither dust nor black carbon causing apparent albedo decline in Greenland's dry snow zone: Implications for MODIS C5 surface reflectance. *Geophysical Research Letters, 42*, 9319-9327, doi:10.1002/2015GL065912.

Rajewicz, J. & Marshall, S.J. (2014). Variability and trends in anticyclonic circulation over the Greenland ice sheet, 1948-2013. *Geophysical Research Letters, 41*, 2842-2850, doi:10.1002/2014GL059225.

Ramanathan, V., & Carmichael, G. (2008, April). Global and regional climate changes due to black carbon. *Nature Geoscience, 1*, 221-227.

Rex, D.P. (1950). Blocking action in the middle troposphere and its effect upon regional climate (I): An aerological study of blocking. *Tellus, 2*, 196-211.

Rignot, E., Box, J.E., Burgess, E., & Hanna, E. (2008). Mass balance of the Greenland ice sheet from 1958 to 2007. *Geophysical Research Letters, 35*(L20502), doi:10.1029/2008GL035417.

Sand, M., Berntsen, T.K., Kay, J.E., Lamarque, J.-F., Seland, Ø., & Kirkevåg, A. (2013). The Arctic response to remote and local forcing of black carbon. *Atmospheric Chemistry and Physics, 13*, 211-224, doi:10.5194/acp -13-211-2013.

Screen, J.A., Deser, C., & Simmonds, I. (2012). Local and remote controls on observed Arctic warming. *Geophysical Research Letters, 39*(L10709), doi:10.1029/2012GL051598.

Serreze, M., & Barry, R.G. (2011). Processes and impacts of Arctic amplification. A research synthesis. *Global and Planetary Change, 77*, 85-96, doi:10.1016/j.gloplacha.2011.03.004.

Shepherd, A., Ivins, E.R., Geruo, A., Barletta, V.R., Bentley, M.J., Bettadpur, S.,…Zwally, H.J. (2012, November). A Reconciled Estimate of Ice-Sheet Mass Balance, *Science, 338*(6111), 1183-1189, doi:10.1126/science.1228102.

Shupe, M.D., Turner, D.D., Walden, V.P., Bennartz, R., Cadeddu, M.P., Castellani, B.B., et al. (2013, February). High and Dry: New Observations of Tropospheric and Cloud Properties above the Greenland Ice Sheet. *Bulletin of the American Meteorological Society, 94*, 169-186, doi:10.1175/BAMS-D-11-00249.1.

Shupe, M.D., & Intrieri, J.M. (2004, February). Cloud Radiative Forcing of the Arctic Surface: The Influence of Cloud Properties, Surface Albedo, and Solar Zenith Angle. *Journal of Climate, 17*, 616-628.

Soja, A.J., Tchebakova, N.M. , French, N.H.F., Flannigan, M.D., Shugart, H.H., Stocks, B.J., … Stackhouse Jr., P.W. (2007). Climate-induced boreal forest change: Predictions versus current observations. *Global and Planetary Change, Special NEESPI Issue, 56*(3-4), 274–296, doi:10.1016/j.gloplacha.2006.07.028, 2007.

Solomon, A., Shupe, M.D., & Miller, N.B. (2017, May 1). Cloud-Atmospheric Boundary Layer-Surface Interactions on the Greenland Ice Sheet during the July 2012 Extreme Melt Event. *Journal of Climate, 30*, 3237-3252, doi:10.1175/JCLI-D-16-0071.1.

Spracklen, D.V., Mickley, L.J., Logan, J.A., Hudman, R.C., Yevich, R., Flannigan, M.D., & Westerling, A.L. (2009). Impacts of climate change from 2000 to 2050 on wildfire activity and carbonaceous aerosol concentrations in the western United States. *Journal of Geophysical Research, 114*(D20301), doi:10.1029/2008JD010966.

Stocks, B. J., Fosberg, M. A., Lynham, T. J., Mearns, L., Wotton, B. M., Yang, Q., … McKenney, D. W. (1998). Climate change and forest fire potential in Russian and Canadian boreal forests. *Climate Change, 38*, 1-13.

Stohl, A., Andrews, E., Burkhart, J.F., Forster, C., Herber, A., Hoch, S.W., … Yttri, K.E. (2006). Pan-Arctic enhancements of light absorbing aerosol concentrations due to North American boreal forest fires during summer 2004. *Journal of Geophysical Research, 111*(D22214), doi:10.1029/2006JD007216.

Strellis, B.M., Bergin, M.H., Dibb, J.E., Sokolik, I., Sheridan, P., Orgen, J.A., … Domine, F. (2013). Aerosol Radiative Forcing over Central Greenland: Estimates based on Field Measurements (Master's Thesis). Retrieved from https://smartech.gatech.edu/bitstream/handle/1853/49063/STRELLIS-THESIS-2013.pdf

Tedesco, M., & Fettweis, X. (2020). Unprecedented atmospheric conditions (1948-2019) drive the 2019 exceptional melting season over the Greenland ice sheet. *The Cryosphere, 14*, 1209-1223. https://doi:10.5194/tc-14-1209-2020.

Tedesco, M., Box, J.E., Cappelen, J., Fettweis, X., Hansen, K., Mote, T., …Wahr, J. (2016a). Greenland Ice Sheet in 2015 [in "State of the Climate in 2015"]. *Bulletin of the American Meteorological Society, 97*(8), S140-S142.

Tedesco, M., Mote, T., Fettweis, X., Hanna, E., Jeyaratnam, J., Booth, J.F., et al. (2016b). Arctic cut-off high drives the poleward shift of a new Greenland melting record. *Nature Communications, 7*(11723), doi:10.1038/ncomms11723.

Tedesco, M., Fettweis, X., Mote, T., Wahr, J., Alexander, P, Box, J.E., & Wouters, B. (2013). Evidence and analysis of 2012 Greenland records from spaceborne observations, a regional climate model and reanalysis data. *The Cryosphere, 7*, 615-630, doi:10.5194/tc-7-615-2013.

Tedesco, M., & Fettweis, X. (2012). 21st century projections of surface mass balance changes for major drainage systems of the Greenland ice sheet. *Environmental Research Letters, 7*(045405), doi:10.1088/1748-9326/7/4/045405.

Tedesco, M., Fettweis, X., van den Broeke, M.R., van de Wal, R.S.W., Smeets, C.J.P.P., van de Berg, W.J., Serreze, M.C., & Box, J.E. (2011). The role of albedo and accumulation in the 2010 melting record in Greenland. *Environmental Research Letters, 6,* doi:10.1088/1748-9326/6/1/014005.

Tedesco, M., Serreze, M., & Fettweis, X. (2008). Diagnosing the extreme surface melt over southwestern Greenland in 2007. *The Cryosphere, 2*, 159-166.

Thomas, J.L., Polashenski, C.M., Soja, A.J., Marelle, L., Casey, K., Choi, H.D., …Dibb, J.E. (2017). Quantifying black carbon deposition over the Greenland ice sheet from forest fires in Canada. *Geophysical Research Letters,* doi: 10.1002/2017GL073701

Välisuo, I., Vihma, T., Pirazzini, R., & Schäfer, M. (2018). Interannual Variability of Atmospheric Conditions and Surface Melt in Greenland in 2000-2014. *Journal of Geophysical Research: Atmospheres, 123*, 10,443-10,463, https://doi.org/10.1029/2018JD028445.

van As, D., Hubbard, A.L., Hasholt, B., Mikkelsen, A.B., van den Broeke, M.R., & Fausto, R.S. (2012). Large surface meltwater discharge from Kangerlussuaq sector of the Greenland ice sheet during the record-warm year 2010 explained by detailed energy balance observations. *The Cryosphere, 6*, 199-209, doi:10.5194/tc-6-199-2012.

van den Broeke, M., Box, J., Fettweis, X., Hanna, E., Noël, B., Tedesco, M., …van Kampenhout, L. (2017). Greenland Ice Sheet Surface Mass Loss: Recent Developments in Observation and Modeling. *Current Climate Change Report, 3*, 345-356, doi:10.1007/s40641-017-0084-8.

van den Broeke, M., Smeets, C.J.P.P., & van de Wal, R.S.W. (2011). The seasonal cycle and interannual variability of surface energy balance and melt in the ablation zone of the west Greenland ice sheet. *The Cryosphere, 5*, 377-390, doi:10.5194/tc-5-377-2011.

van den Broeke, M., Smeets, P., & Ettema, J. (2009). Surface layer climate and turbulent exchange in the ablation zone of the west Greenland ice sheet. *International Journal of Climatology, 29*, 2309-2323, doi:10.1002/joc.1815.

van der Werf, G.R., Randerson, J.T., Giglio, L., van Leeuwen, T.T., Chen, Y., Rogers, B.M., …, Kasibhatla, P.S. (2017). Global fire emissions estimates during 1997-2016. *Earth System Science Data, 9*, 697-720. https://doi.org/10.5194/essd-9-697-2017.

Van Tricht, K., Lhermitte, S., Lenaerts, J.T.M., Gorodetskaya, I.V., L'Ecuyer, T.S., Noël, B., et al. (2016). Clouds enhance Greenland ice sheet meltwater runoff. *Nature Communications, 7*(10266), doi:10.1038/ncomms10266.

van Vuuren, D.P., Edmonds, J., Kainuma, M., Riahi, K., Thomson, A., Hibbard, K., …, Rose, S.K. (2011). The representative concentration pathways: an overview. *Climate Change, 109*, 5-31, doi:10.1007/s10584-011-0148-z.

Velicogna, I., Sutterley, T.C., & van den Broeke, M.R. (2014). Regional acceleration in ice mass loss from Greenland and Antarctica using GRACE time-variable gravity data. *Geophysical Research Letters, 41,* 8130-8137, doi:10.1002/2014GL061052.

Ward, J.L., Flanner, M.G., & Dunn-Sigouin, E. (2020, submitted). Impacts of Greenland Block Location on Clouds and Surface Energy Fluxes over the Greenland Ice Sheet. *Journal of Geophysical Research: Atmospheres*.

Ward, J.L., Flanner, M.G., Bergin, M., Dibb, J.E., Polashenski, C.M., Soja, A.J., & Thomas, J.L. (2018). Modeled response of Greenland snowmelt to the presence of biomass burning-based absorbing aerosols in the atmosphere and snow. *Journal of Geophysical Research: Atmospheres, 123*. https://doi.org/10.1029/2017JD027878.

Wang, C. (2004). A modeling study on the climate impacts of black carbon aerosols. *Journal of Geophysical Research, 109*(D03106), doi:10.1029/2003JD004084.

Wang, Q., Jacob, D.J., Fisher, J.A., Mao, J., Leibensperger, E.M., Carouge, C.C., … Doherty, S.J. (2011). Sources of carbonaceous aerosols and deposited black carbon in the Arctic in winter-spring: implications for radiative forcing. *Atmospheric Chemistry and Physics, 11,* 12453-12473, doi:10.5194/acp-11-12453-2011.

Wang, W., Zender, C.S., & van As, D. (2018). Temporal Characteristics of Cloud Radiative Effects on the Greenland Ice Sheet: Discoveries from Mulltiyear Automatic Weather Station Measurements. *Journal of Geophysical Research: Atmospheres, 123*, 11348-11361. https://doi.org/10.1029/2018JD028540.

Warren, S.G., & Wiscombe, W.J. (1980, December). A Model for the Spectral Albedo of Snow. II: Snow Containing Atmospheric Aerosols. *Journal of the Atmospheric Sciences, 37*, 2734-2745.

Woods, C., Caballero, R., & Svensson, G. (2013). Large-scale circulation associated with moisture intrusions into the Arctic during winter. *Geophysical Research Letters, 40,* 4717-4721, doi:10.1002/grl.50912.

Woollings, T., Hoskins, B., Blackburn, M., & Berrisford, P. (2008, February). A New Rossby Wave-Breaking Interpretation of the North Atlantic Oscillation. *Journal of the Atmospheric Sciences, 65,* 609-626, doi:10.1175/2007JAS2347.1.

Yang, W., Guo, X., Yao, T., Yang, K., Zhao, L., Li, S., & Zhu, M. (2011). Summertime surface energy budget and ablation modeling in the ablation zone of a maritime Tibetan glacier. *Journal of Geophysical Research, 16*(D14116), doi:10.1029/2010JD015183.